QATAR UNIVERSITY

COLLEGE OF ENGIEERING

A NON-DESTRUCTIVE METHODOLOGY FOR LEAK DETECTION IN WATER NETWORKS USING INFRARED PHOTOGRAPHY (IR) AND GROUND PENETRATING RADAR (GPR)

BY

MOHAMMAD RAFE DAHER KHADER

A Thesis Submitted to the Faculty of

In Partial Fulfillment

of the Requirements

for the Degree of

Master of Science

January 2016

COMMITTEE PAGE

The members of the Committee approve the thesis of Mohammad Khader defended on 10-02-2016

_____

Dr. Alaa Al-Hawari
Thesis/Dissertation Supervisor

_____

Dr. Arslan Ayari
Committee Member

_____

Dr. Osman A Elnawawy
Committee Member

_____

Dr. Mohsin Khalid Siddiqui
Committee Member

_____

Prof. Abdalla Shanableh
Committee Member

Approved:

_____

Dr. Rashid Alammari, Dean, College of Engineering

Abstract

Two noninvasive and nondestructive methodologies for detecting leaks in water pipes were proposed and tested. The first method combines the use of Ground Penetrating Radar (GPR) for accurate determination of pipe location, followed by infrared (IR) thermographic imaging for determining the leak location. In IR thermography, four operating conditions (varying camera height and speed) were tested. Results were statistically analyzed using analysis of variance (ANOVA) and pairwise comparison methods. Several factors were found to affect the accuracy of the proposed methodology in predicting the leak location, namely, the characteristics of the studied surface (i.e. emissivity), the characteristics of the surrounding environment (i.e. ambient temperature and relative humidity), and the operating conditions of the IR camera (i.e. speed and height of the camera). In the case of low emissive surfaces, a slower camera speed would be required for the camera to be able to capture the thermal contrast at the real leak location. The results obtained in this study have also shown that under high ambient temperatures and high relative humidity conditions, a higher speed of the IR camera would reduce the impact of noise on the collected thermal contrast and therefore, would give better leak location prediction results. The field of view (FOV) is affected by the camera's height from the surface. At lower heights, less area will be covered per frame; therefore, a more homogenous temperature distribution per frame will be obtained. Consequently, the contrast between the different frames will be higher and better leak predictions would be expected. The tested methodology proved the flexibility of the approach and the ability of accurately predicting the leak location under different conditions. In method two: the GPR alone was used to

predict the existence and location of a leak in a water pipe. GPR data processing was performed based on the refined radargram, resulting in promising outcomes in the applicability of the method.

TABLE OF CONTENTS

List of Tables

List of Figures

Acknowledgment

I would like to express my gratitude to my advisor Dr. Alaa Al-Hawari for his continuous support, understanding, expert guidance and encouragement throughout my study and research.

My appreciation also extends to Qatar General Electricity and Water Corporation (KAHRAMAA) for their valued help and support in the data collection. In addition, I would also like to acknowledge Qatar National Research Fund (QNRF) for funding this research (NPRP-5-165-2-055).

Finally, I would like to thank my family and my friends for their extended support and encouragement during the previous two years.

Chapter 1: Introduction

1.1 Water Situation Overview

Global freshwater supplies are increasingly under pressure. Current industrialization and dramatic population growth are increasing the burdens on the planet's water resources. According to the World Economic Forum, the water crises is considered to be the third main threat of global concern [1]. Water scarcity is one of the most widespread challenges that retard urbanization and affect the economic and environmental aspects of human life worldwide [2, 3]. Water scarcity encompasses all means associated with restricted water availability, where it can be defined as an insufficient water resources availability that would satisfy consumers' average requirements on the long-term [4]. Also, water scarcity is defined as the overuse of water resources when the available water is less than the water demand [5, 6].

Due to the dramatic increase in the world population that amounted to almost 1 billion per ten years, water shortage crisis became more critical [7]. More than 700 million people lack access to clean safe water [2]. Therefore, serious actions must be taken to search for fresh water alternatives and maintain the existing water resources and assets especially in areas where water resources are rare and scarce as in the GCC area.

1.2 Water Situation in Qatar

The state of Qatar is experiencing critical challenges in securing fresh water resources and maintaining the current water assets for municipal and industrial uses. Qatar has one of the lowest rainfall rate in the world with an average of 82 millimeters per year and it has high

evaporation rate [8]. Accordingly Qatar dependence on water mainly from: ground water, sea water desalination and reclaimed water (Figure 1). According to Qatar National Development Strategy (QNDS), the country is losing 2000 millimeters of water due to natural evaporation yearly that makes it into a water deficiency. In addition to the low water resources in Qatar, Qatar has been nominated as one of the highest per capita household water consumption globally with an average usage of 310 liters daily per capita, twice greater than the consumption of western European countries (Figure 2) [9].

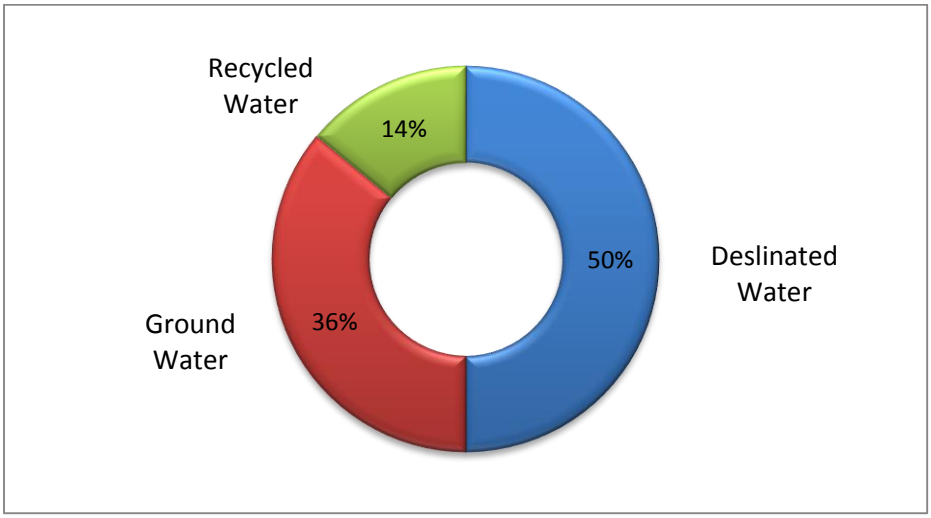

Figure 2. Water sources in Qatar

Household water consumption is expected to increase 5.4% for Qataris and 7% for expatriates yearly until the year 2020. However, production of potable water per capita has been retarded recently due to the increase in the per capita water use (Figure 3). In addition, the current water desalination technologies are desalinating limited amounts of seawater. New facilities were commissioned in 2011 in which their desalination capacity will be 48% higher than previously used desalination plants.

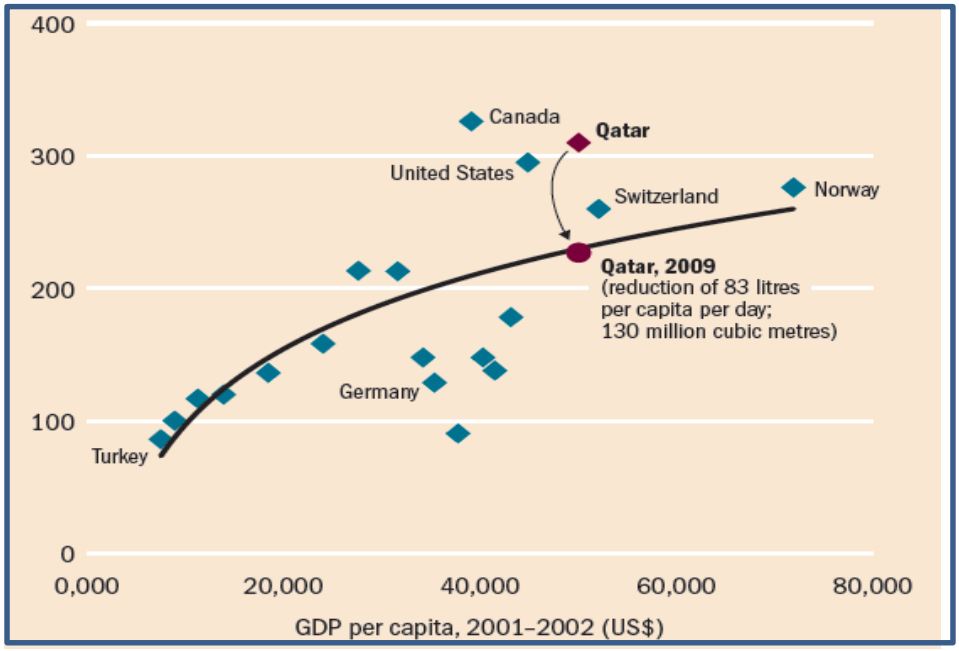

Figure 3. Per capita household consumption) [9]

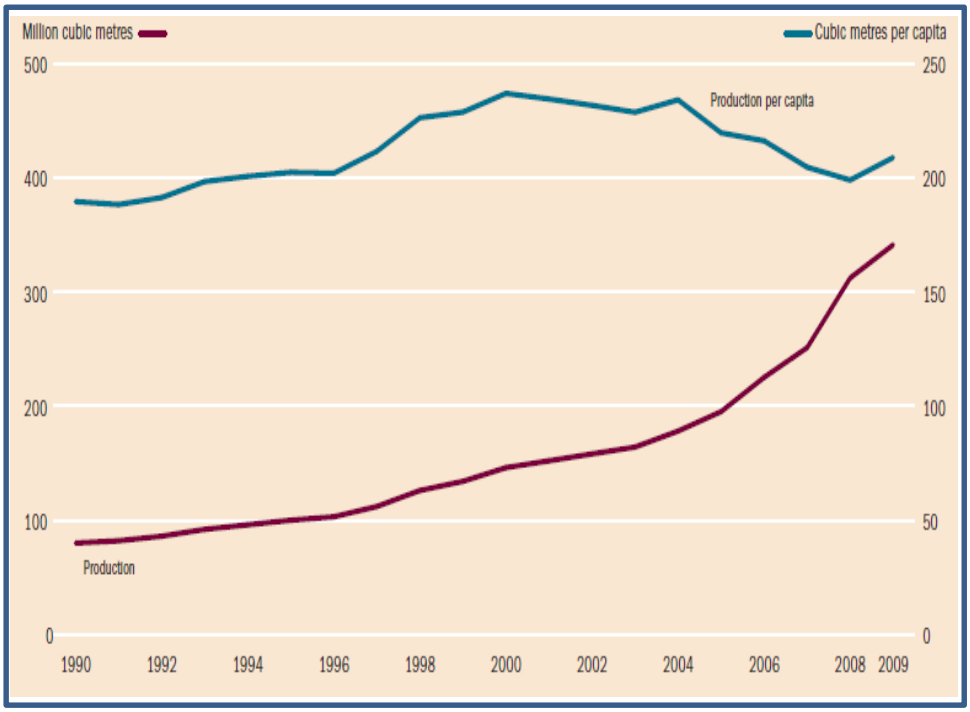

Figure 4. Desalinated water production [9]

Groundwater makes 36% of Qatar's water sources. Groundwater is extracted from natural aquifers that are entirely consumed for agricultural purposes. The amount of recharge into the aquifers is 50 million cubic meters coming from rainfall and flows from neighboring Saudi Arabia each year. However, 250 million cubic meters are being extracted yearly from groundwater that increases the risks of aquifers depletion [9].

Treated sewage water or recycled wastewater is an abundant source of water in Qatar, where it is commonly used in irrigation and play a significantly larger role in district cooling by reusing 26% of the total freshwater supplies. However, due to the lack of the required infrastructure to deliver the recycled wastewater, the consumption of such water is less than the supply that leads to dumping 40% of the treated sewage water into septic lagoons or to the sea [9].

1.3 Water Leaks

Water distribution networks (WDN) are considered to be one of the most valuable and crucial municipal infrastructure systems. They constitute the core of urban population growth, public health, welfare and safety [10]. Nevertheless, according to a 2006 World Bank report, water losses through WDN were summed up to 45 million cubic meters daily in developing countries and more than 32 billion cubic meters annually on the global level [11]. Water losses in water networks do not only mean the loss of an invaluable resource, but also the loss of money spent on treating and transporting it; moreover, the deterioration of the subterranean infrastructure [12, 13]. With the significant population growth in Qatar and subsequent increase in population density [14], the amount of stress on the network

increased and the risk of decreasing its lifetime and potential leaks have become much higher. Water leakage is a primary sign of pipe deficiency; therefore, monitoring the network and promptly detecting leaks is essential for its longevity and the reduction of water losses.

The government of Qatar has developed large networks of civil infrastructure, including the water distribution network (WDN) to support the growth of urban population and businesses and to improve public health, safety and welfare. Qatar government made a major capital investment in the development and expansion of its water distribution networks to support the growth of urban population and local economy. The water resources of Qatar are especially precious given the relatively small area of land and territory of Qatar. Over three hundred million cubic meters of potable water are pumped annually through a water distribution network (WDN) that extends over 5,400 kilometers to all parts of Qatar [15]. In Qatar, desalinated water losses are abnormally high. Based on Qatar General Electricity and Water Corporation (Kahramaa) statistics, 30%-35% of the desalinated water pumped through the water facilities is lost because of old water pipelines that are still in use Figure 4, while the average loss should not exceed 18% [9].

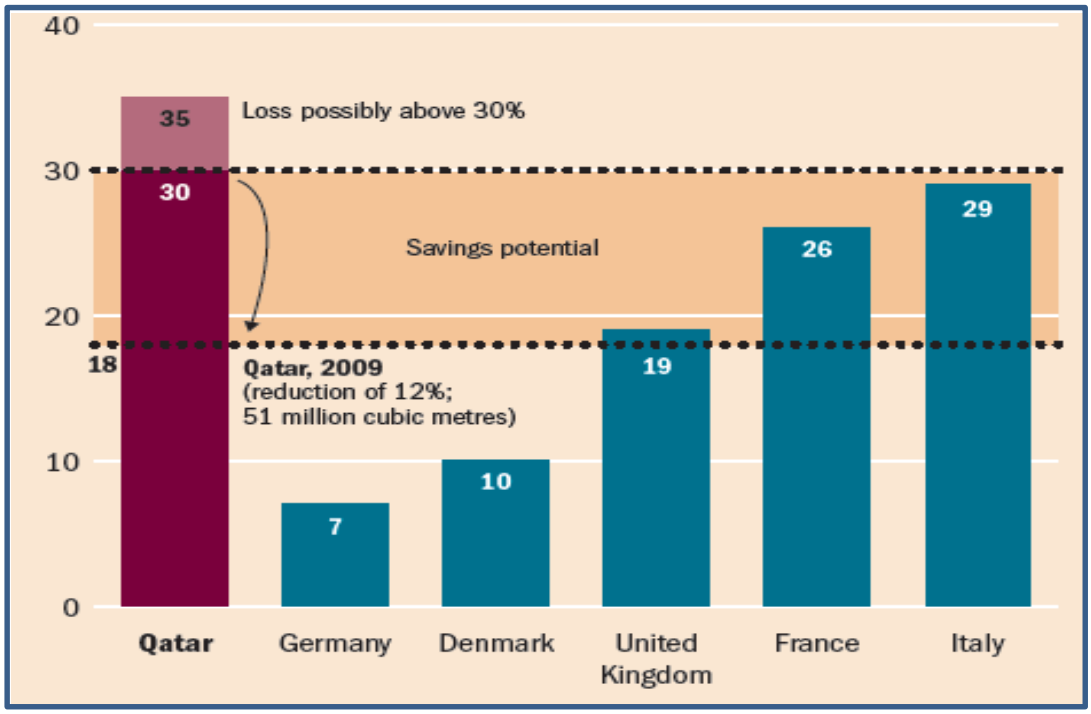

Figure 5 .Water network losses [9]

One-third of the produced desalinated water leaks into the surroundings and to the water table yearly, which is almost 100 million cubic meters per year (Figure 5). The excess inflow of Doha water table has two main sources: Kahramaa's leaking water network and Ashghal's sewage collection network. Consequently, such leaks may impose serious health hazards by septic tanks overflowing, also excessive leaks could increase costs of building projects since extra precautions must be taken to limit the effects of such leaks (dewatering, waterproofing) [9]. Apart from the physical deficiencies, the lost water constitute a financial burden on the government, where water losses cost approximately $150 million a year according to the Statistical Authority of Qatar (SAQ) [16].

Serious actions have been taken by Doha municipality and Kahramaa towards the issue of water leaks. They are aiming to reduce the Doha water table net inflow from water

networks to zero through enhancing the existing piping system and investing in leak-sealing operations to minimize network water losses by 2016 to 10%. This will be done by spreading awareness to the public about excessive water consumption and by imposing extra fees on water consumption.

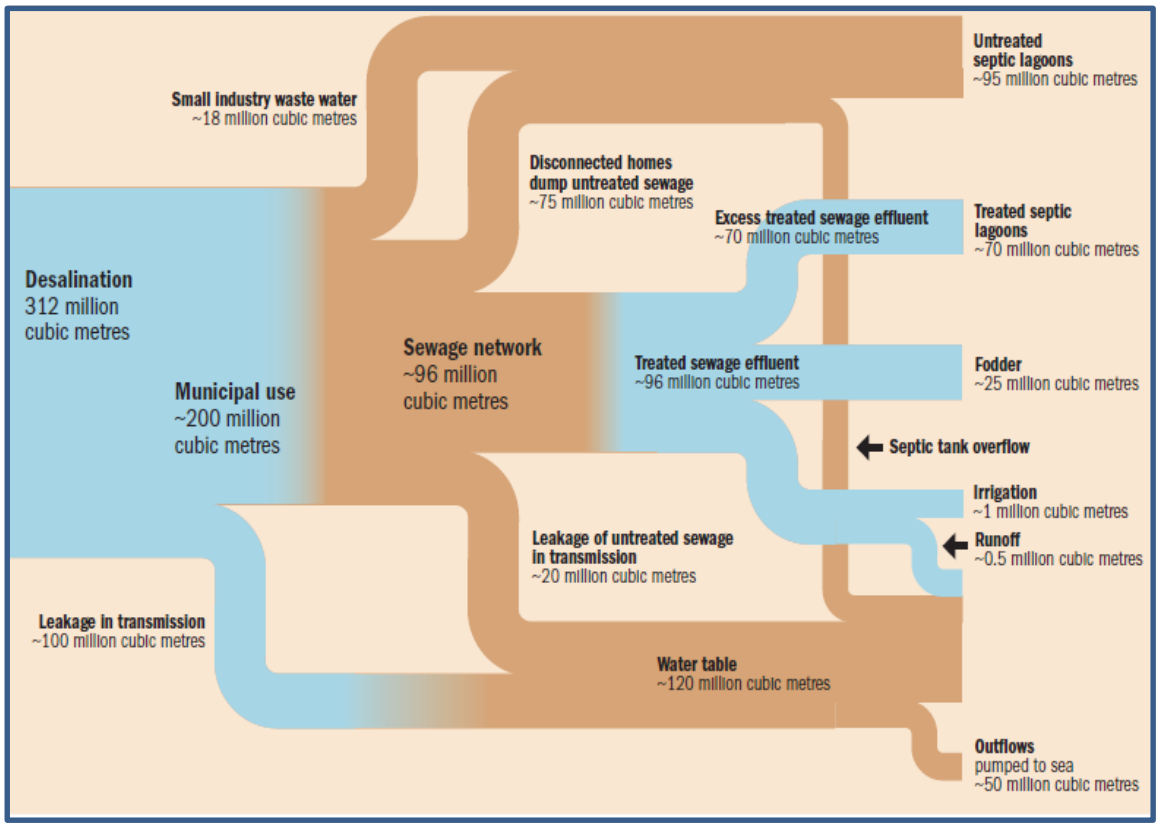

Figure 6. Desalinated water lifecycle [9]

Chapter 2: Literature Review

2.1 Introduction

One of the main components of water conservation in water utilities is early detection and repairing of leaks. Breakage of water mains might occur due to fluctuating water temperatures, vibrations, soil movement and pressure fluctuations. The impacts of water mains deterioration are: economic (higher operating and capital cost and lower income), operational (lower service level), environmental (high water and energy usage rate, consequently higher carbon and water footprints), social (traffic disturbance) and public health (contamination) [17, 18]. Several technologies have been used to early detect leaks in water networks. These technologies can be categorized into four main categories: 1- Visual techniques 2-Electromagnetic and radio frequency techniques 3- Ultrasound techniques 4- Acoustic and vibration techniques. In addition to some other techniques that do not belong to the mentioned categories [19].

2.2 Visual Techniques

Pipe internal surfaces can be monitored using such a technique through visual inspection that can be performed using closed-circuit television (CCTV), laser-based surface profiler, or videoscope [20].

2.2.1 Closed-Circuit Television (CCTV)

Since direct human-entry to the pipe is dangerous (for both pipe and human), a real-time assessment technique that is safer and cheaper has been implemented, where it consists of an illuminating device and television camera that can move through the pipes by a pulley system and winch. The system should be inserted into the pipe through an access point (manhole or fire hydrant), and then the captured data (videos and images of the interior pipe) will be sent to the processing computers. [20].

CCTV is considered as a slow and time-consuming method, depending on the number and size of the detected leaks, since the carrier should stop whenever a leak is observed to scan and inspect the area entirely. The interpretation of the transmitted data is dependent on the operator's experience to judge, detect and classify the leaks that could be a source of confusion. Beside this issue, CCTV is not a waterproof approach. Thus the pipe must be emptied [21]. To overcome the potential of contradiction in data interpretation, automatic assessment of images through processing technique can be implemented to improve interpretation and decision-making process by extracting and processing condition information from CCTV files. Other techniques were implemented to overcome manual interpretation process [22].

2.2.2 Laser Scan

The interior side profile of the pipe can be detected visually through a laser scan in which it can point corrosion loss and pipe side deflections. In this approach, the pipe interior is scanned and profiled at any point along its length through a continuous pulse of the laser

beam. However, the laser should be kept away from any source of diffraction (waterline) [23]. Therefore, this approach is applicable only in dewatered pipes and should not be used in peak hour times (used only in low-flow times) since there is no application of laser profiling underwater until today[20].

Unlike CCTV, laser scan does depend on vision inspections, therefore, it can be used in darkness. The resolution of the collected data is a function of spinning speed, velocity of the carrier, rate of sampling and some physical features of the pipe wall (color and roughness). Special softwares were coded for the integration of the scanned images which allows users to visualize the collected data in 3D profiles [24].

2.2.3 Videoscope

Videoscope approach is an optical device used in inaccessible areas for visualization purposes. It consists of eyepiece and lens connected to a rigid or flexible tube integrated by a relay visual system. Videoscope is an improved kind of borescope with a diameter less than 10 mm and length of 15.24 m. It is controlled and operated easily through articulated controls, and data can be analyzed and processed with a special software [20].

2.2.4 3D Optical Scanning

A 3D optical scanner Figure 6 operated with the help of two digital cameras (high resolution) connected to a wide-angle, distortion-free lenses where the captured data are transmitted to a control unit (vehicle) to be stored and analyzed by experts [20].

Figure 7. 3D optical manhole scanner [20]

2.2.5 Handyscan 3D

Handyscan 3D approach Figure 7 is a visual leak detection technique that consists of two cameras of laser and stereo vision combined for accelerating the process of profiling the object's surface with high-resolution images that can be analyzed using special softwares [20].

Figure 8. Handy scan 3D [20]

Advantages, limitations, purpose and performance of visual approaches are summarized in Table 1.

Table 1. Visual water leak detection techniques comparison

Techniques	CCTV	Laser scan	Videoscope	3D Optical scanning	Handyscan 3D
Purpose	Visual inspection without man-entry/ pipes inner surface inspection	Capturing pipe surface topography	Remote visual inspection for inaccessible pipes.	Boreholes, drilled shaft and manholes inspection.	Non-contact inspection applicable to industrial design and manufacturing
Area of use	Applicable for sewer pipes and limited for water mains.	Applicable for storm water and sewer pipes	Applicable for gas, oil, water and wastewater pipeline in addition to other applications (security, aircraft engines, automotive transmission, etc.)	Applicable for manholes with 400 mm diameter and more.	No information is available regarding its usage in water mains.
Advantages	-Applicable for large and small pipes. -Relatively cheap, simple. - Able to capture a full view of the experimented pipes.	-Early detection of pipe degradation by capturing primary signs of corrosion. -Helps in rehabilitation processes by providing an exact geometric dimension for the inspected pipe. -Minimum lighting is required. -applicable for several pipe sizes.	- Inaccessible and hidden areas become visible. -Provide images with high quality. -Rapid video capturing.	-Rapid inspection. -Applied for pipe-shaped structures and vertical pipes.	-Better scanning efficiency than laser alone. -Free of orientation. -Easy to operate and setup.
Limitations	-Only inner defects are detected. -Relatively slow. -pipes scrubbing are needed before inspection. -mainly depends on manual interpretation.	-pipes scrubbing are needed before inspection -pipes dewatering is substantial. -Only limited methodology is available for crack detection.	-Advanced interpretation of the qualitative results is required. -applicable only for small diameter and short-length pipes. -Experts inspectors are needed for quantitative assessment.	-Similar general limitations for the other visual inspection techniques.	-applicable only for large and short length pipes. -pipes scrubbing are needed prior to inspection
Performance	Relative to the personnel skills and experience.	Accurate, however data processing during scanning is necessary to compensate errors.	-Relative to the personnel skills and experience. - Accurate, however data processing during scanning is necessary to compensate errors.	-Relative to the personnel skills and experience. - Accurate, however, data processing during scanning is necessary to compensate errors.	No information is available. (A study was conducted using such a technique on helicopter blades, and the results were confidential).

2.3 Electromagnetic and Radio Frequency Techniques

Electromagnetic (EM) inspection techniques are considered as non-destructive non-invasive approaches that deal with magnetic fields and electric currents or both and monitor the electromagnetic response of the reflected EM waves.

2.3.1 Magnetic Flux Leakage (MFL)

MFL approach forms a saturated magnetic field surrounding the pipe wall using large magnets. A homogeneous and uniform magnetic flux distribution shows a pipe in a good condition. Consequently, deficiencies will cause the magnetic flux to change. Figure 8 shows a detector coil that records the flux leakage. MFL can be implemented outside pipes (in service pipes) or inside pipes (must be dewatered). However, the pipe size should be noticed for the equipment to fit properly inside [20]. Defects in the pipe wall are being recorded using a magnetic sensor inserted into the system and moves along the pipe and able to detect tiny leaks without causing any flow clogging [25]. An Enhanced type of MFL has been developed through pulsed excitations that help to acquire more data from a wider frequency band [26]. Data collected from MFL are raw, in which it must be interpreted through advanced software (Advanced Engineering Solutions) that implement certain algorithms to characterize and identify metal losses [20].

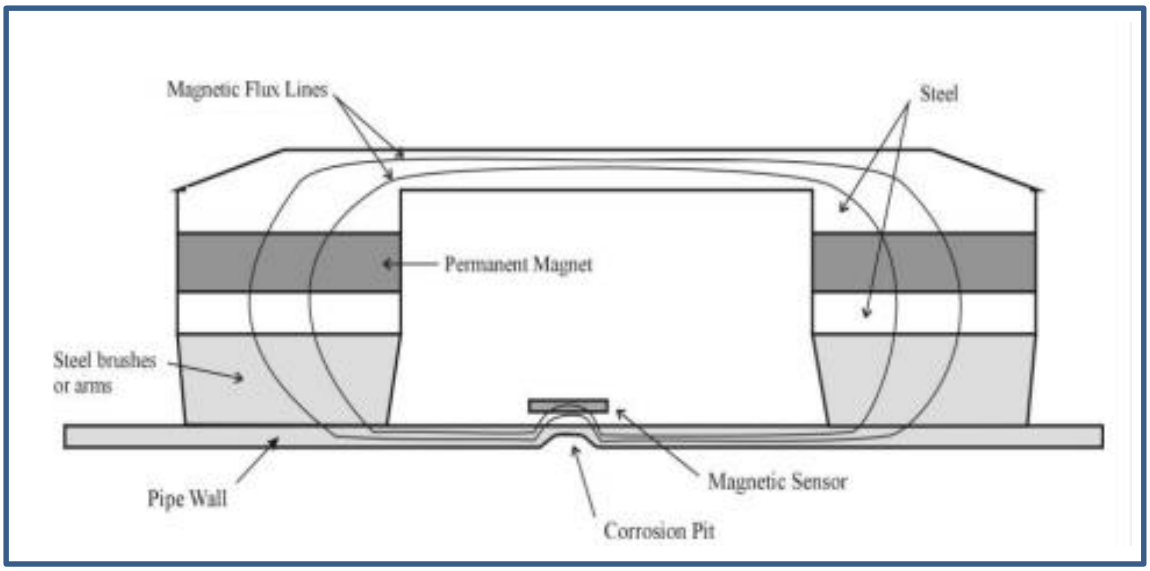

Figure 9. Principle of MFL inspection [20]

2.3.2 Eddy Current (EC)

Similar to MFL, EC technique deals with magnetic field changes occurring due to pipe defects. However, the production of the magnetic field differs from MFL. EC utilizes the idea of eddy current phenomena that takes place as a result of current changing in a magnetic coil. The induced coil moves along the pipe imposing eddy current on the pipe wall generating a magnetic field opposes the main one. Therefore, characteristics of the pipe will be a function of the recorded magnetic field impedance [25]. Although EC technique can work without direct contact with the pipe, the pipe skin depth is an issue that has been overcome through the use of Remote field eddy current (RFEC) in which its signal is greater than direct eddy current signal and able to penetrate pipe walls properly [21]. Several works have been done expressing the accuracy of RFEC. RFEC had been enhanced by adding an extra coil, and it can be operated underwater for 150 mm pipes in collaboration with certain commercial devices [27].

2.3.3 Hydroscope Technology

Hydroscope technology principle is similar in concept to the RFEC approach, where it relies on transmitting electromagnetic signals through pipe walls and receiving it back (through a cable connected to a field computer) by a detector that measures any signal variation and assesses the pipe condition accordingly. Through inserting the system to the pipe through an access point (fire hydrant for example), it moves with water flow and inspects 1000 m daily. However, small defects cannot be detected using such a technique [27]. Hydroscope approach overcome the dewatering issue of most of the visual techniques since it can be operated underwater also the pipe skin depth is not an issue unlike RFEC [21].

2.3.4 Rapid Magnetic Permeability Scans (RMPs)

In this method, two strong magnets are inserted into the pipe wall to create a magnetic field that will induce magnetic flux to be transferred through the pipe wall. Changes in the magnetic flux while passing through the pipe wall could indicate cracks or gradual pipe wall erosion as a result of corrosion [21].

2.3.5 Time Domain Ultra-Wideband

In non-ferrous pipelines, the time domain ultra-wideband approach is recommended to be applied towards pipe condition monitoring since it works in a wider range of frequency and results in high-resolution images [28]. The process works by emitting and receiving pulses in Pico or Nano-seconds that detects voids in the soil surrounding the pipe and monitor all leak characteristics such as location, orientation and size of the leak [21].

However, the prototype of the mentioned approach is still under research. Advantages, limitations, purpose and performance of electromagnetic and radio frequency approaches are summarized in Table 2.

Table 2. Electromagnetic and radio frequency water leak detection techniques comparison

Techniques	MFL	Eddy current	Hydroscope technology	RMPs	Time domain ultra-wideband
Purpose	Metal loss inspection and detection in ferrous pipes due to corrosion. (inside and outside pipes)	Metal loss inspection and detection in ferrous pipes due to corrosion.	Determination of the remaining wall thickness in Cast Iron and Ductile Iron Pipes	Leak detection in metallic pipes.	Detection of below surface corrosion, defects, and voids in non-metallic pipes
Area of use	-Oil and gas industry.	- Oil and gas industry in addition to chemical plants.	Domestic water distribution network.	Used in machinery components such as gears, engines and drive shafts.	Not determined yet
Advantages	-High accuracy in wall thickness measurement. -can be operated externally (without service interruption).	- Insulation coatings removal is not necessary. - Able to perform underwater.	-One of the most advanced approaches available. -ability to detect areas of corrosion pitting. -Ability to estimate pipes remaining useful life.	-Can be used in-pipe and outside the pipe. - Rapid technique. - Real-time assessment. -easy to operate.	-Accurate results of the pipe wall thickness. - provides high image resolution. -able to monitor pipe wall, as well as the pipeline.
Limitations	-In-line inspection requires unlined, cleaned metallic pipes. -not suitable for small pipe sizes.	-Signal interpretation and analysis require a high level of expertise. -Results may be get affected by some factors such as temperature.	-Pre-cleaning of tuberculate pipes is required. -Expensive. -Unable to detect pits smaller than 3 cm3	-Not applicable for pipes less than 100mm in diameter. -not applicable for thick coating pipes (or lining pipes).	Not determined yet
Performance	- calibration processes must be implemented to acquire accurate wall thickness measurements and small defects detection,	- Eddy current technique provides a high level of data accuracy and good repeatability.	- Hydroscope technique provides high level of wall thickness accuracy	-was extensively used for metallic pipe condition assessment.	Not determined yet

2.4 Acoustic and Vibration Techniques

2.4.1 Sonar Profiling System

Sonar profiling system is a leak detection technique that uses the acoustic approach for underwater pipe inspection and corrosion loss measurement through the use of scanner unit, process unit and skid set.

Where the system measures the travel time of the sound signal that being emitted from the transmitter to the target and back, in addition to the velocity of the sound sonar signal at the medium (approximately 0.2-0.2m/s), the distance between the transmitter and the target can be evaluated. Information about pipe cross section is carried out through each received signal. Because the speed of sound is a function of the media (air–water), the system is unable to work concurrently in both water and air, so the images should be acquired distinctly and combined at the end of the inspection [25].

For a different type of applications, different frequencies should be used in the sonar profiling system, where higher frequencies are suitable for low penetration applications (since its wavelength is low). However, the acquired images are high definition, however for applications that need a higher penetration, lower frequencies are used but with poor image quality. High-Frequency pulses are recommended While testing through clear water or inspection for small leaks, whereas low frequency is suitable for turbid water. Thus, a multi-frequency system captures the optimum data and information [24]. Moreover, a sensor that can be inserted inside the pipe to emit a wide range of frequencies is now under research.

2.4.2 LeakfinderRT

Leakfinder RT system compromises of a set of acoustics sensors such a hydrophone, wireless signal transmission, accelerometer, and computer. Accelerometers and hydrophones are utilized for detecting leak-induced sounds and vibrations in water column respectively. Accelerometers and hydrophones are integrated to enhance the signal to noise ratio (Figure 9). LeakfinderRT principle is based on two sensors inserted into different access points (manhole, fire hydrant) which are used to estimate the similarity of two waveforms through application of time-lag (τ_{max})function (cross-correlation) using the following equations [20]:

$$L_1 = \frac{D - C * \tau_{max}}{2} \qquad (2.1)$$

$$L_2 = D - L_1 \qquad (2.2)$$

Where D is the distance between the two access point and c is the experimental propagation velocity of sound in the pipe. L_1 and L_2 are representing the leak positions according to the access point. LeakfinderRT provides high-resolution images of narrow-band leaks signals, where leak sounds are received and analyzed instantaneously, however sound analysis might take more time in case of background noise. The main limitation of this method is its inability to detect leak size [20].

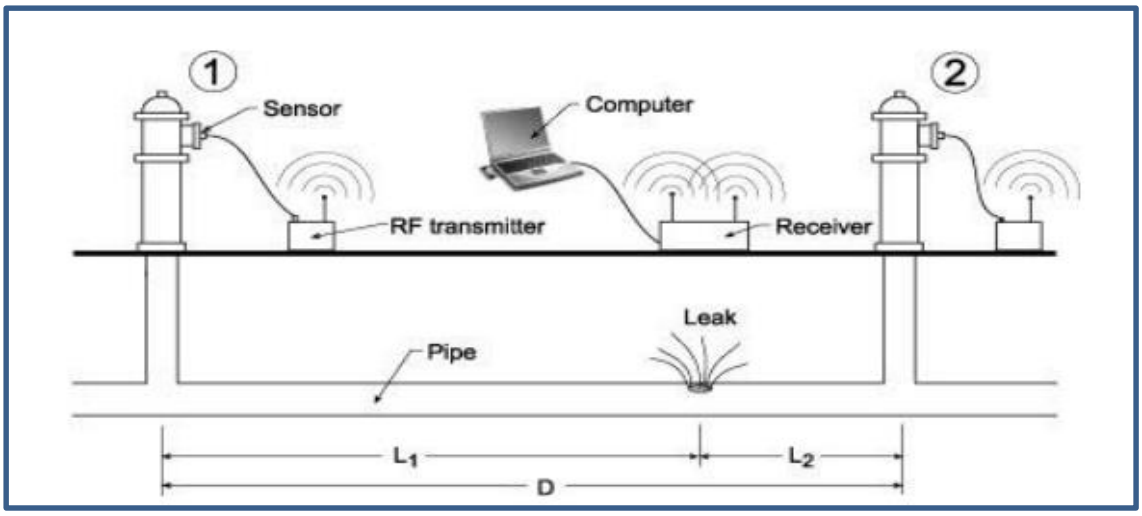

Figure 10. Principle of leakfinder RT [20]

2.4.3 Sahara System

Sahara system Figure 10 is considered as an acoustic approach for water leak detection that uses a hydrophone connected to an umbilical cable, which moves in-pipe (through an access point) and records leak signals and noises [25, 29]. The location of the hydrophone can be followed on the surface to locate the exact location of the leak noise to be excavated for repairing processes [30]. However, it might become difficult for the inspector to track the pipeline if it passes through a municipal construction (highway) or environmental obstacle (river).

The key factor in detecting leaks and its magnitude using this system is to identify the unique acoustic signals produced by leaks in the pipe joints, wall or steel welds [30].Also gas pockets can be detected similarly through its distinctive acoustic signatures. Sahara

system provides a video and lighting sensor which enables CCTV inspection of potable in-service water pipes.

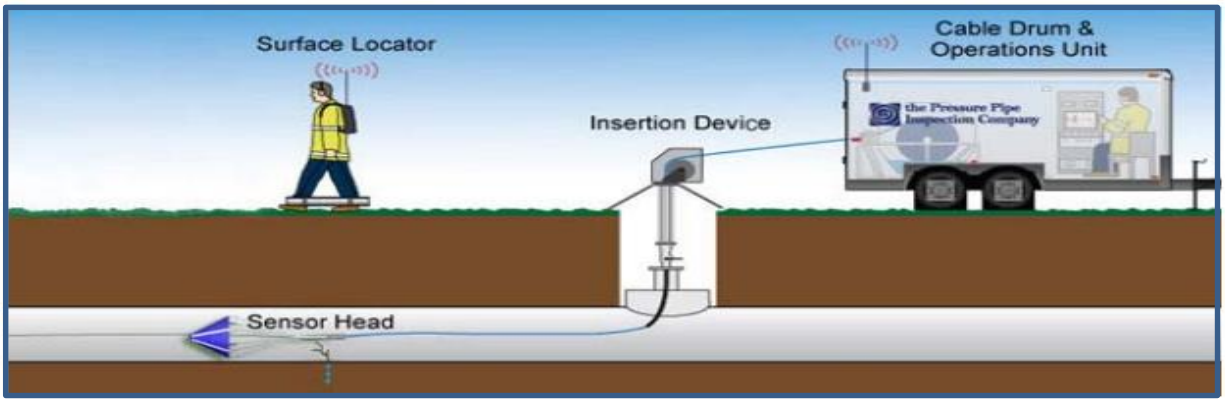

Figure 11. Sahara system [20]

2.4.4 Smartball

Smartball is an acoustic leak detector that travels in-pipe with the flow of water and locates, detects and calculates the leak magnitude using a set of the magnetometer, accelerometer, temperature sensors and ultrasonic transmitter enclosed in an aluminum alloy core Figure 11 with an electricity source and other electronic components [31]. The external surface of the ball gives an extra surface area helps in rolling the device and decreases the noise generated while moving in the pipe. The sphere outer diameter is dependent on the flow conditions and pipe diameter. Smartball captures and records acoustic information while rolling inside the pipe and emits an acoustic pulse each 3 seconds to be tracked by an acoustic receiver, then the acquired acoustic information can be analyzed based on a frequency analysis approach to ensure that the collected data is associated with a leak event, not any other anomaly. Smartball technique can inspect a pipeline up to 12 hours and

detects leaks within 1m accuracy. Bypass lines might be blocked if the ball route was not carefully planned [20].

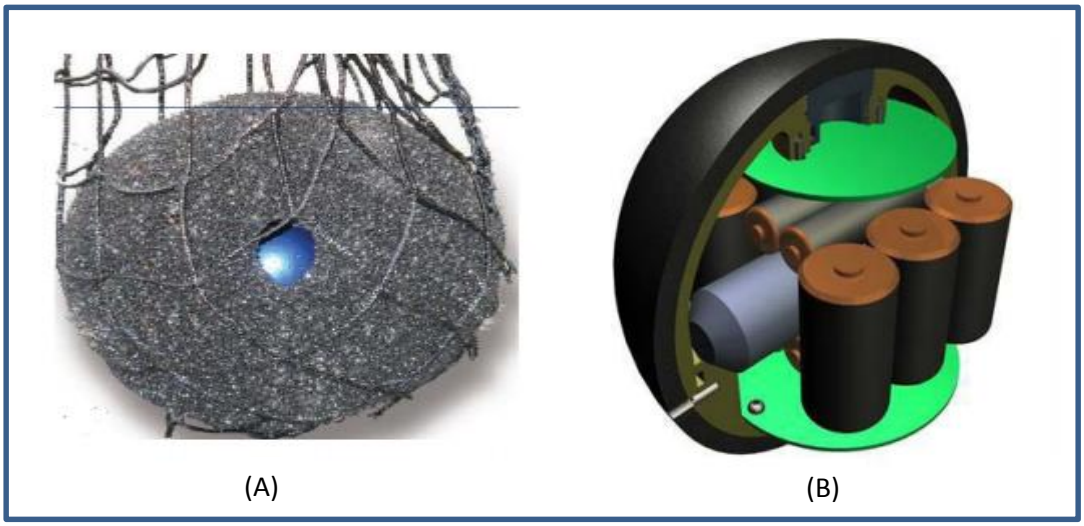

Figure 12. Smartball system, A :(External view), B: (Internal view) [20]

2.4.5 Impact Echo

Impact echo approach is widely used in assessing damaged pre-stressed concrete pipes [27]. It comprises a controlled impact (large hammer or falling weight) and geophones attached to the pipeline wall, once the hammer hits the pipe, for instance, waves of low frequency are produced, transmitted through the pipe wall and received by the geophones. The detected waves are dissimilar in properties (different penetration depths, traveling speed and frequencies), consequently such a difference can be correlated to the pipe condition and the soil embedding the pipe as well [27], through the use of impact-generated stress waves calculations implemented using the impact echo equation [32]:

$$T = \frac{V}{2F_p} \qquad (2.3)$$

Where T is the pipe thickness, V is the speed of the wave and F_p represents the peak frequency.

2.4.6 Permalog

Permalog Figure 12 is an acoustic system installed in-pipe for detection and classification of leak noise in water distribution networks. It can be installed semi-permanently or permanently through valves or pipe fittings and can be collected back using magnets. It usually operates at night where the background noises are minimum, and pressure is high. Once the leak is detected the unit produces an alarm sound and emits a radio signal to indicate a leak event [33]. Information carried by the loggers can be retrieved by removing the loggers and acquire the data manually (lift and shift) or by transmitting the data through radio through a patrol system to a moving patrol vehicle (drive by), or through transmitting the data directly to a lab computer using radio network (PermaNet). Due to its ease usage, Permalog has been implemented by several water authorities (Las Vegas Valley Water District, West Virginia American water, and Birmingham Water Works Board).

Figure 13. Permalog [20]

2.4.7 Listening stick

During this approach, sticks are used at the pipe in the suspected areas for listening to the leak propagation noise and estimating the time delay. However, this method is applicable in metallic pipes and not suitable for plastic pipes [21]. MLOG and STAR ZoneScan are also considered as acoustic techniques for leak detection that are similar in concept to the previous ones discussed [20]. Advantages, limitations, purpose and performance of acoustic and vibration approaches are summarized in Table 3.

Table 3. Acoustic and vibration water leak detection technique comparison

Techniques	Sonar Profiling system	LeakFinderRT	Sahara system	Smart ball	Impact echo	Permalog
Purpose	Determines internal pipe defects underwater by providing visual profiles.	Determines leaks in all type of water distribution pipes. (Computer based).	In-service water mains inspection to detect leaks, visible defects, gas pockets and a wall thickness of metallic pipelines.	Detects air pockets and leaks in large and medium pipes (diameter>8in.)	Determination of location and extent of deficiencies (surface cracks dimensions, voids).	-leak detection and monitoring.
Area of use	Applied to sewer pipes, however, no clue about its usage in water mains.	All fluids transmission pipelines.	-Used in large mains in addition to cast iron pipes. -can be used as a CCTV system.	-wastewater and water pipelines	-Used mainly in flat surfaces (bridge decks, concrete slabs, etc.). -In large water sewer PCCP and concrete pipes.(man access)	-Used mainly in water distribution systems.
Advantages	-able to operate without system disturbance (sewer). -can be integrated with a CCTV system to inspect submerged pipes.	- Able to operate without system disturbance. -locate leaks in a plastic pipe through low-frequency vibration sensors. -determines small leaks associated with high background noise. -uses advanced correlation method to enhanced leak detection process.	- Able to operate without system disturbance. -High sensitivity to small leaks. -can be tracked from the ground surface while inspection. -Able to work in large and small pipes.	-applicable for several pipe material (PVC, steel, concrete,etc.) -able to detect leaks and air pockets in pipes with large diameter (>20cm). -efficient in detecting small noise. - Able to operate without system disturbance.	-operated in various materials. -can be carried out easily. - Insulation coatings removal is not necessary. - single access point is needed (to excite the pipe).	- Permanent or semi-permanent. - Non-destructive method. -Rapid approach (without disturbance for neighborhood areas). -Cheap running cost (permalog operated with battery requires minimum maintenance and cheap cost). -monitor leaks automatically.

Limitations	-should be applied beneath the water. -Limited by the used functional frequency.	-unable to determine the leak size. -sensitive to the interference of low-frequency vibrations (road traffic or pumps). -sensor spacing is a function of the pipe diameter and material.	-access point is required. -Must be operated within particular frequency depends on pipeline flow rate and bends. -considered as intrusive technology (the system must be inserted into the pipe).	-inapplicable for high water pressure pipes (>400psi). -Provides qualitative results (need to be processed later).	-complicate frequency analysis (in case information other than geometry and thickness is needed). - inapplicable to metals. -Tests may get affected by the embedded items inside the pipe.	- The scanned length is a function of the pipe material where closer spacing is required in plastic pipes, unlike metallic pipes. -Must be operated in a time with minimum background noise.
Performance	Results in an accurate pipe cross-section data	-Detects small leak under low pressure in PVC pipes. -able to locate metal pipes small leaks. -efficient in high background noise locations. -Results accuracy are depending on sensor spacing and propagation velocity.	-Succeeded in determining small unknown leaks (≈0.25 gal/hr). - Able to detect leaks within an accuracy less than 1m).	-efficient in detecting leaks of less than 0.1 gal/hr. - Able to detect leaks with an accuracy of 1m).	-Impact echo system can test pipes with thickness ranges from 66mm to 1.8m). -Typical accuracy of impact echo system is 2%.	No information is available.

2.5 Ultrasonic Techniques

Ultrasonic techniques are implemented through sending sounds of high frequency towards the inspected object and receive and analyze the reflected echo. Such a technique has been utilized for monitoring of corrosion, delamination tests and thickness measurements of pipes.

2.5.1 Guided Wave Ultrasonic Testing

Propagated long distance waves are considered to be the core of using guided wave ultrasonic testing approach [34]. Two types of ultrasonic waves are the most common in this technique: torsional waves (move with a shearing motion) which require two transducers and longitudinal waves (move with a compressional motion) which should be operated by 3-4 transducers to be propagated along the pipe length. In case of in-service pipe inspection (filled with water), torsional waves are most applicable, while longitudinal waves are not. Once these guided waves (torsional or longitudinal) get obstructed by a certain pipe feature or anomaly, it returns to its original position (transducers), and then anomaly distance from the transducer can be estimated by measuring the time-of-flight for each reflected wave , also defect size can be determined by estimating the reflected wave amplitude.

An ultrasound waves are emitted in the both directions along the length of the pipe using a ring probe (Figure 13) of piezoelectric transducers tied around the pipe, where the vertical axials is representing the ultrasound wave amplitude that can be used to extract mean features/deficiencies of the pipe against the pipe length that is represented by the horizontal

axis. Guided wave technique is applicable for pipes with a diameter greater than 50mm and wall thicknesses less than 40mm, also elevated pipe can be inspected using such a technique. However, it is limited by 30m length away from the ring.

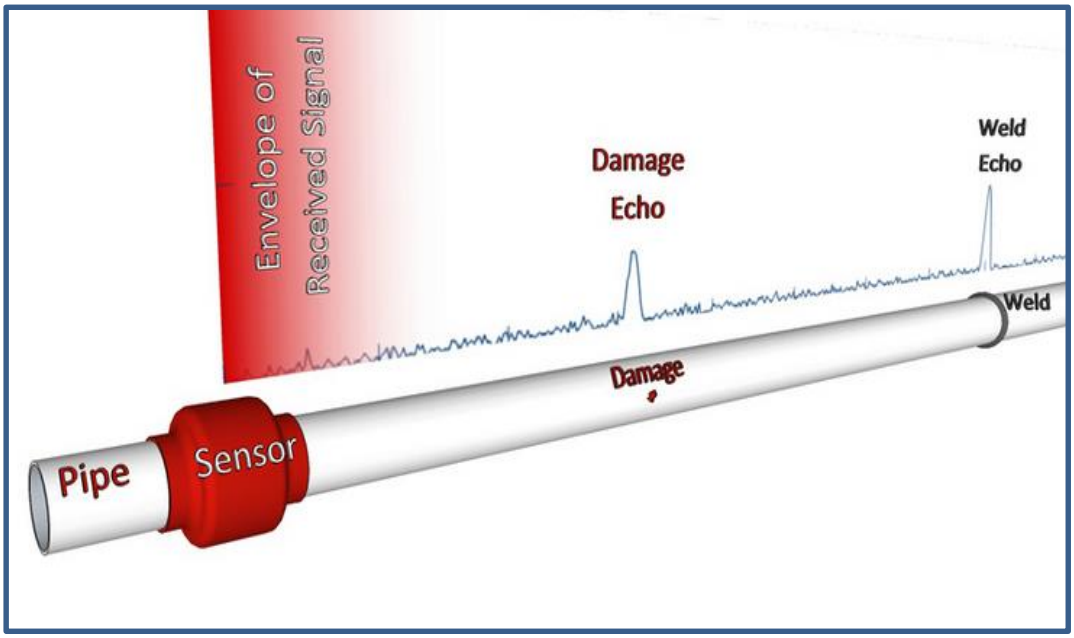

Figure 14. Ultrasonic guided wave pipeline inspection diagram). Courtesy of 164th Acoustical Society of Ameria Meeting

2.5.2 Discrete Ultrasound Measurement

Transmitter, receiver, monitor and transducer are creating the discrete ultrasound system, where a set of pulses are emitted using the transmitter within a high-frequency ultrasonic energy generated by the transducer to scan the pipe, where some of the ultrasound energy will be reflected back due to encountering an anomaly and reassembled in the form of electrical signal carrying out the anomaly significant features (location , size, and others) in side view, plan view and cross-section view of the experimented pipe. The defect location will be calculated by estimating the travel time of the reflected wave and its speed. This approach must be operated while the pipe is in service since energy propagation must pass through water. However it can be conducted internally and externally within high results accuracy. The name discrete represents the three different set of scans performed by the system (A-scan-scan and C-scan) [24].

2.5.3 Phased Array Technology

Phased array approach has been implemented towards medical imaging in the previous two decades and has recently been used for industrial purposes. Phased array system comprises a transducer and set of individual sensors element controlled using ultrasound electronics [35] that integrated to detect pipe wall thickness, cracks, and corrosion through one multi-element transducer. Sensor elements can be formed into different orders as a linear array, two-dimensional matrix array, circular array and other complicated forms, so for measuring a pipe wall thickness all of the sensor elements must be triggered simultaneously and a sound beam orthogonal to the surface of the wall is produced, however, an angular sound

beam is generated in case of crack detection Figure 14. Phased array systems are implemented in the nuclear industry for coarse-grained stainless steel materials monitoring since other ultrasound approaches were found to have a lack of accuracy and substantial limitations.

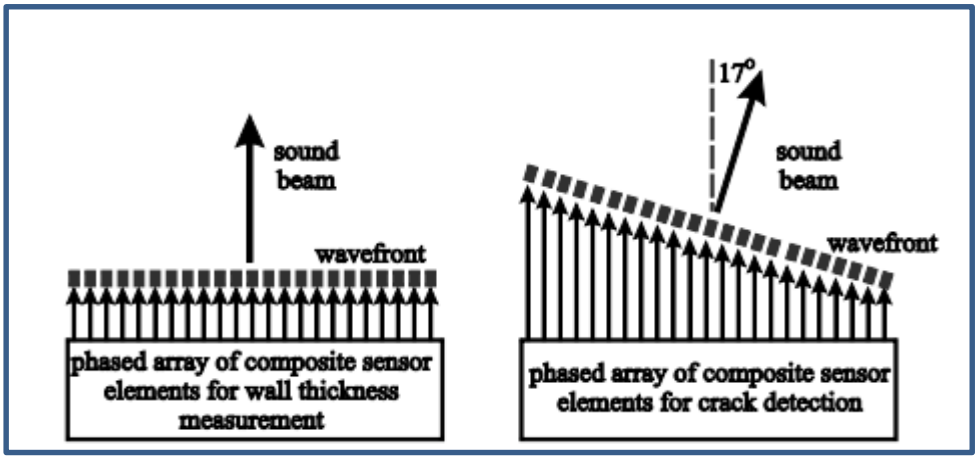

Figure 15. Sound beams generated by phased array of composite sensor elements [20]

2.5.4 Combined Ultrasound Inspection

This approach has been utilized towards pipeline inspection for simultaneous metal loss and cracks monitoring than can be implemented for gas and oil pipelines [36]. Sensor carrier was designed and optimized in order to conduct both inspections in one run by ground of ultrasound sensors (which operated using a pulse-echo mode in addition to high repletion frequency) placed to scan the pipe along its length. Similar to the phased array approach, straight pulses are used to examine the wall thickness. However cracks will be detected using the gradual pulses. Advantages, limitations, purpose and performance of acoustic and vibration approaches are summarized in Table 4.

Table 4. Ultrasound water leak detection technique comparison

Techniques	Guided Wave Ultrasonic Testing	Discrete Ultrasound Measurement	Phased Array Technology	Combined Ultrasound inspection
Purpose	Fast material loss inspection due to erosion and corrosion	External and internal pipes inspection for erosion and corrosion.	Wall thickness measurement and crack detection using phased array beams.	-Crack and metal loss detection
Area of use	-Above-ground insulated or exposed pipes.	-Used mainly for thickness measurements delamination checks in forgings, welds, and ferrous pipes.	-Used in nuclear power plants, aerospace, pipe mills, steel mills and petrochemical plants.	-Used mainly in oil and gas pipelines.
Advantages	-able to inspect coated and insulated structures. -Rapid approach.	-Rapid approach. -can be operated at various probe sizes and frequencies. -Pipe remains in-service while inspection.	-Quick inspection. - Inspection can be performed through different perspectives to monitor complicated anomalies.	-High inspection speed. -High resolution.
Limitations	-Inspection is limited to above ground pipes of 30 m long. -applied to limited buried pipes length (shorter than aboveground pipes). -Distinguish between external and internal corrosion is not possible. -not effective in heavily coated pipes.	-cannot perform in empty pipes. -Limited applicability for inspecting irregular shape, not homogeneous or rough materials (e.g. concrete). -Must be calibrated. -Pipe cleaning is required. -as a result of low transmission in sound and high signal noise, it is not applicable in CI and coarse-grained materials.	- Expensive. - Complex set-up for three-dimensional applications.	-pipes access is necessary. -Cracks and losses data need to be analyzed, processed and correlated by an expert to assess the integrity and status of the line at any given time.
Performance	-High sensitivity in calculating cross-section losses (can detect very tiny losses)	-Significant accuracy for wall thickness estimation.	-accurate discontinuity detection within minimum testing time. - No information about its use in water main pipelines.	-High accuracy in detecting the crack width and metal loss.

2.6 Other Techniques

2.6.1 Microwave Back-Scattering Sensor (MBS)

MBS sensor method comprises four staggered receiving patch antennae and four transmission patch antennae. It operates based on the concept of transmission of continuous electromagnetic microwaves that are being emitted at a frequency of 2.45 GHz, and back-scattered signals will be received back [37]. MBS sensor method detects deficiencies resulted in erosion and humidity changes that caused by water leaks, such anomalies can be investigated through monitoring changes in dielectric properties, through recording and analyzing the reflected signals that will be having information about the relative phase and amplitude of each signal. MBS sensor is an in-pipe leak detection approach, where the entire inner pipe surface is covered for inspection.

2.6.2 Continuous Wave Doppler Sensing Technique (CWDS)

CWDS system consists of a unit operated at 2.45 GHz, homodyne receiver, a digital signal processing unit, and power transmitter. The working mechanism of CWDS depends on detecting the Doppler frequency shift of the electromagnetic waves reflected because of the leaked water[38].CWDS technique is able to locate and detect the leakage source accurately regardless the soil, environment conditions and the pipe material as well ,unlike acoustic approaches that face difficulties in detecting leaks in polyvinylchloride (PVC) and high-density polyethylene (HDPE) pipes, thus this system is said to be promising and can be integrated with other commercial leak detection apparatus to provide an advanced

system toward enhancing water leaks locating and detecting. Research now are undergoing to come up with a digital signal processing algorithm able to acquire data rapidly.

2.6.3 Radiographic Testing

Radiographic techniques use radiation of gamma and x-rays, where gamma rays that are produced from isotopes are used in cementitious and ferrous materials, however, plastic materials can be noted using X-rays produced from cathode-ray tubes. Imperfections of the scanned pipe are illustrated once radiations pass through the pipe material and distorts the photographic film. Radiographic approach can be operated into three different setups: single wall-single image, where single object will be penetrated by the radiation onto the film, double wall-single image, where the radiation passes through two sections of the pipe wall, double loading where two films are used (one slow film and one fast film) Radiographic techniques are considered to be an accurate method, however pipes are having diameter not less than 38.1 cm must be emptied [24].

2.6.4 Acoustic Fiber Optics (AFO)

AFO system comprises of fiber optic sensors positioned along the pipe length and acquiring data through an optical data obtaining system connected to the sensors and is producing laser light among the fiber. Fibers are experiencing external stresses imposed by the acoustic waves; that results in light reflection through the fiber, where these reflections convey the pipe features to be analyzed using the data obtaining system. AFO system is considered to be costly since it is suspected to physical damages while installation, so special tests need to be run towards proper installation. However, AFO is

applied when the early leak detection is more vital than the running cost [39]. Advantages, limitations, purpose and performance of acoustic and vibration approaches are summarized in Table 5.

Table 5. Comparison between the other water leak detection techniques

Techniques	MBS	CWDS	Radiographic	AFO
Purpose	Pipe inspection for hidden objects and anomalies detection.	Minor water leaks detection in supply pipes	Valves inspection in addition to thicknesses changes monitoring in structures and materials.	Determination of pipe wall thickness
Area of use	Sewage system.	Plastic, PVC and HDPE pipes.	-Used mainly by the water sector.	-Petrochemical, oil, gas and chemical processing industries in addition to PCCP pipes.
Advantages	-provides useful information that can be integrated with other leak detection approaches.	-not affected by the environmental condition, soil condition or the pipe material. -can be integrated with other water leak detection equipment or techniques.	-applicable to all materials.	-applicable for long term inspections. -able to detect 12.4 miles of pipe using one sensor.
Limitations	Not available	-an advanced digital signal analyzing and processing method is required for data collection to accelerate the process.	-slow approach (limited zone can be inspected at a time). -requires access to the pipe. -Radiation safety precaution must kept in mind.	-Expensive. -Fibers are too sensitive.
Performance	Not available	-able to detect and locate the exact leakage point accurately.	-Results in accurate measurements, however, collected data needs and expert interpreter.	-The accuracy of AFO results is dependent on the pipe diameter, material, and initial thickness.

2.7 Used Technologies

2.7.1 Infrared Thermography

2.7.1.1 Introduction

Infrared thermography (IRT) is a technique used to measure objects' temperature and evaluate temperature differences (contrast) between two surfaces or objects. IRT has been established based on measuring the radiant energy distribution that is emitted from an object. At the early 1800s, Herschel discovered the infrared spectrum while trying to invent new optical filters that would decrease the degree of the image sun brightness in telescopes [40].Then Herschel discovered new rays that were similar to the visible rays in behavior since they were refracted, absorbed, transmitted and reflected [41]. Following Herschel's discovery and the debate induced by Seebeck about the nature of light and heat, after some experiments performed in closed circuits of dissimilar metallic conductors with small electric current flows inside, Nobili produced the first thermocouple based on the effect of the thermoelectric [42]. In 1840 using the differential evaporation of a thin film of oil exposed to a heat pattern, Herschel developed the first thermal image (thermograph) [43]. A breakthrough in the history of IR was achieved in 1880 by the inventor of the bolometer Samuel Langley, which was marked as a great success in the IR detection sensitivity [44], where the solar radiation intensity was measured at different wavelengths that allowed the examination of the solar irradiance. In 1929, Tihanyi invented the first infrared-sensitive camera that was implemented by the British anti-craft defense. In the period between Worlds Wars I and II significant improvements were conducted to develop the photo detectors and image converters, also infrared spectroscopy was introduced as an essential

chemical analysis technique, such improvements were helpful to the military since it introduced the night vision tactic. In the late 1950s, the US Military and Texas Instruments company produced the first single element detectors that enabled producing line images and scanning of scenes. Starting from the late 1960s, IR cameras became commercialized, and thermography became available for public [44].

2.7.1.2 Infrared Thermography Fundamentals

IRT and IR camera are operated by thermal radiation theory. Radiation consists of collection of discrete particles known scientifically as 'quanta' or 'photons,' each particle having an energy E (J) that equals [45]:

$$E=hv=\frac{hc}{\lambda} \qquad (2.4)$$

Where h is Planck's constant ($6.626x10^{-34}J$), C is the speed of light in vacuum (299,792,458 m/s) and λ is the wavelength. The electromagnetic spectrum is divided into a number of wavelength intervals (spectral bands) extends from (λ=0 → λ= ∞). The term radiation includes all the wavelengths in the electromagnetic spectrum. However, IRT's application is limited to radiation emitted by the temperature of an object, which is also known as thermal radiation that is given by the Stefan-Boltzmann equation [46]:

$$E_b = \sigma T^4 \qquad (2.5)$$

Where E_b is the total emissive power, σ is the Stefan-Boltzmann constant ($5.67051x10^{-8}\ W/m^2K^4$), and T is the surface absolute temperature in kelvin.

The total emissive power E_b gives the intensity of radiation as the summation of radiation at various wavelengths. Spectral emissive power indicates the emitted power as a function of a specific wavelength in addition to the surface temperature. In other words it is the emissive power in the wave band in the infinitesimal wave band between λ and $\lambda + d\lambda$. Spectral emissive power can be quantified using the following equation [45]:

$$I_{\lambda,b}(\lambda, T) = \frac{(2hc^2)\lambda^{-5}}{\exp^{hc/k\lambda T}-1} \qquad (2.6)$$

Where k is the Boltzmann's constant (1.3805 x 10^{-23} J/K). Integrating equation 2.6 over all wavelengths yields the maximum emissive power at a given temperature, known as blackbody emissive power [45]:

$$E_b = \int_0^{\infty} E_{\lambda,b}(\lambda, T)d\lambda = \int_0^{\infty} \frac{C_1\lambda^{-5}}{\exp^{(\frac{C_2}{\lambda T})}-1} d\lambda \equiv \sigma T^4 \qquad (2.7)$$

Where $C_1 = 2\pi hc^2 = 3.742x10^8\ W\mu m^4/m^2$, $C_2 = \frac{hc}{k} = 1.439x10^4\ \mu mK$. To calculate the spectral emissive power at specific wavelength range $\lambda 1$ and $\lambda 2$, integration of the Planck distribution should be conducted in this range as follows :

$$(\Delta E_b)_{\lambda 1 \to \lambda 2} = \int_{\lambda 1}^{\lambda 2} \frac{C_1\lambda^{-5}}{\exp^{\frac{C_2}{\lambda T}}-1} d\lambda \qquad (2.8)$$

2.7.1.3 Factors Affecting Thermal Contrast at Ground Surface

Several factors interfere with the process of an object energy radiation. For example, the physical properties of an object itself will affect the object's ability to emit energy as thermal radiation that is known as emissivity. The temperature transfer to the surface from

the surroundings can be considered as an independent factor (independent of the surface material), for example, the heat transfer process from the water pipe and its surroundings to the ground surface may be classified as independent factors. Conduction into the ground surface, convection, sunlight absorption, and gray-body irradiation to the surrounding are all kinds of heat transfer processes that contribute to forming a surface energy.

2.7.1.4 Conduction

Heat conduction can be defined as a molecular transfer of thermal energy in liquids, gasses and solids due to the temperature gradient. Particles of a substance are expected to experience a heat transfer in the form of conduction when they are directly in touch with each other and have temperature differences. For example water pipelines are in contact with the surrounding soil, therefore, if a leak occurs the adjacent soil particle will result in a temperature gradient that will change the soil temperature and will cause abrupt temperature variations at the ground surface. Mathematically, the process of heat flowing due to conduction is assumed to be a steady-state heat flow in one direction [47]:

$$Q_{cond} = \frac{K^{+}_{cond}(T_p - T_s)}{L} \quad (W/m^2) \quad (2.9)$$

Where K_{cond} is the average thermal conductivity of the soil and pavement surface in (w/m*K), $T_{p\,and}\,T_s$ are pipe temperature and surface temperature, respectively. L is the pipe burial depth (heat flowing path).

2.7.1.5 Convection

Convection is defined as the heat transfer due to gasses and liquids movement. Convection is considered as the main type of heat transfer in fluids. Convection comprises the

combined processes of advection and conduction. For example a ground surface would experience such type of heat transfer due to the heated air by sun radiation. Therefore temperature difference between the ground surface and the heated air drives energy to transfer toward the cooler areas that would affect the captured IR thermos-grams. Heat convection can be expressed mathematically as follows [48]:

$$Q_{conv} = h_{conv}(T_s - T_{ambient}) \ (^{W}/_{m^2}) \qquad (2.10)$$

Where h_{conv} is the convection coefficient in (w/m^2 *K) and $T_{ambiant}$ is the ambient temperature. Convection coefficient is defined as the amount of thermal power per unit area (heat flux) over the temperature difference between the fluid and the surface [48]:

$$h = \frac{q}{\Delta t} \qquad (2.11)$$

Where h is the heat transfer coefficient w/m^2 *K, q is the heat flux w/$m^2$and Δt temperature difference between the surrounding fluid area and the solid surface in kelvin Also, it can be expressed empirically in terms of the wind speed as follows [48]:

$$h_{conv} = 5.6 + 4.0xV_{wind} \qquad (2.12) \qquad \text{for } V_{wind} \leq 5 \text{ m/s}$$

$$h_{conv} = 7.2x(V_{wind})^{0.78} \qquad (2.13) \qquad \text{for } V_{wind} > 5 \text{ m/s}$$

Where Vwind is the wind speed in m/s

2.7.1.6 Sunlight absorptivity

Another factor that interferes with the process of heating up the ground surface is the amount of absorbed sunlight. This incoming heat flow can be quantified as follows [49]:

$$Q_{sun} = \gamma_{abs} x Q_{inc} \ (^{W}/_{m^2}) \qquad (2.14)$$

Where Q_{inc} is the incident solar radiation ($^{W}/_{m^2}$) and γ_{abs} is the solar absorptivity of the pavement. Emissivity can be defined as a measure of the object effectiveness in radiating energy. It can be defined as the ratio between the radiated energy from an object to the radiated energy from a black body under the same wavelength and temperature. Emissions from the ground surface to the sky should be taken into account as a radiative heat transfer factor, 1which can be mathematically expressed as follows [50]:

$$Q_{sky} = \sigma \epsilon * \left(T_s^4 - T_{sky}^4\right) \quad (^{W}/_{m^2}) \qquad (2.15)$$

Where ϵ is the pavment smissivity , σ is the Stefan-Boltzmann constant which equals 5.669x10^{-8} $^{W}/_{m^2 * C^4}$, T_s is the pavement surface temperature(K) and T_{sky} is the calculated sky temperature (K) that can be expressed as follows [51]:

$$Tsky = \epsilon_s^{0.25} * \ T_{ambient} \qquad (2.16)$$

Knowing that the sky emissivity can be calculated as [51]:

$$\epsilon_s = 0.787 + 0.764 * \log_e(T_{dew}/273) * F_{cloud} \qquad (2.17)$$

T_{dew} Is the dew point temperature in kelvin with the cloud cover factor F_{cloud} as follows [51]:

$$\mathrm{F_{cloud}} = 1.0 + 0.024\mathrm{N} - 0.0035\mathrm{N}^2 + 0.00028\mathrm{N}^3 \qquad (2.18)$$

Where N describes how cloudy the sky is, and taking values between 0% clear-100% overcast.

2.7.1.7 Thermography Infrared (IR) camera system

A *VarioCAM hr head* thermographic system was used in performing the set of field experiments Figure 15. The system has a Long Wave Infrared spectral range (LWIR) of 7.5 to14 µm. The lens reflects the object scene onto a microbolometer array at a resolution of 384 x 288 pixels, which means that each image will be translated to 110,592 temperature data points. A wide-angle lens was used to capture the IR radiation emitted by the object in the field of view (FOV) and to duplicate it onto the detector array with a focal length of 12.5mm and a minimum focus of 0.2m. Other properties and technical specifications of the *VarioCAM hr* system are stated in Table 6.

Figure 16. VarioCAM hr head thermographic system

Table 6. Technical specifications of VarioCAM hr head system

Spectral range	**7.5 to14 µm.**
Temperature measuring range	(-40 to 1,200) ^{o}C
Emissivity	Adjustable from 0.1 to 1.0 in increments of 0.01
Recording, image format (pixels)	384 x 288
Spectral range	Long Wave Infrared spectral range (LWIR) of 7.5 to14 µm
Standard lens (field of view)	1.0/25 mm (30 x 23)^{o} at (384 x 288)
IR frame rate	50/60 Hz
Zoom function	Up to 8 digital, infinitely variable
Operation temperature	(-15 to 50) ^{o}C
Storage temperature	(-40 to 70) ^{o}C
Humidity during operation and storage	Relative humidity 5% to 95%, non-condensing
Dimensions (complete system)	(133 x 106 x 110) mm
Weight (complete system)	Approx. 1.3 kg
Automatic functions	autofocus, auto-image, auto-level, alarm

2.7.2 Ground Penetrating Radar (GPR)

Ground-penetrating radar sends electromagnetic waves through the ground to the subsurface then reflections from the underground objects will be received again by the radar. The waves are emitted and received back through an antenna, creating a profile of the subsurface. In 1929, the first attempt to determine the depth of ice in a glacier was performed in Austria using ground penetrating radar demonstrating that electromagnetic energy is capable of traveling in media other than air. Forty-three years later, NASA had built a prototype GPR system to be sent on Apollo17 to the moon to study the geological and electrical properties of the moon's crust. The potential of using GPR had become attractive to the archeological community because of its ability to detect buried

archeological features and associated sediments. Thus, in 1975 the first application of GPR in archeology was conducted in Chaco Canyon New Mexico. From the late 1970s to the mid-1980s, several surveys had been conducted in Cyprus, El Salvador and Japan to locate burial rises and buried houses. Cultural resource management projects (CRM) gained some attention in the period between the late 1980s and early 1990s that encouraged the use of GPR in some archeological contexts. In the late 1990s to mid-2000s extra efforts were performed in the area of GPR data processing, where various research had been implemented to demonstrate the differences in data collection and analysis [52, 53].

2.7.2.1 Ground Penetrating Radar (GPR) System

A MALÅ Ground Penetrating Radar (GPR), placed on a Terraplus Rough Terrain Cart (RTC), was used in this study Figure 16. The MALÅ GPR was equipped with two shielded antennas, 250 MHz antenna (Dimensions: 0.74 x 0.44 x 0.16 m – Weight: 7.85 kg) and the shielded 500 MHz antenna (Dimensions: 0.50 x 0.30 x 0.16 m – Weight: 5.0 kg).

Figure 17. Ground Penetrating Radar (GPR), on a Terraplus Rough Terrain Cart

2.8 Scope and Objectives

In this study, two non-invasive and non-destructive methods have been developed to detect and determine leak locations effectively and at the same time overcome limitations associated with currently utilized leak inspection and detection methods. In method one a combined methodology of using ground penetrating radar (GPR) for accurate determination of pipe location, followed by an infrared (IR) thermography imaging technique for determining leak location has been proposed. The infrared thermography imaging technique will be used for the first time in extremely hot weather conditions instead of cold or moderate weather conditions.

In this method the following factors will be studied:

- The impact of the IR camera height from the ground surface.
- The impact of the IR camera speed.
- The impact of different kinds of surface grounds.

In method two: the GPR alone will be used to predict the existence and location of a leak in a water pipe. GPR data processing will be performed based on the refined radargram images collected from the GPR.

The proposed methods will assist in (i) reducing water losses in water distribution networks by early detection of leaks; and (ii) increasing water system's safety, functionality, and its targeted levels of service by speeding up the detection of leaks and thereby the response to them.

Chapter 3: Methodology

Several factors might interfere in the leak detection process. Physical factors (e.g. pipe size, pipe age, pipe type), environmental factors (e.g. surface type, soil type) and operational factors. In the proposed methodology the only factors that would affect the leak detection process can be reduced to environmental and operational factors. The GPR relies on the dielectric contrast of the soil surrounding the pipe and the IR relies on the temperature contrast of the ground surface regardless of the pipe material or size. [55]. Accordingly, operational and environmental factors had been included in this study. Two methods were proposed to detect and predict a leak location in water mains.

3.1 Method One (GPR+IR)

A combination of using both GPR to define the buried pipes locations and IR thermography to identify leak locations were used. The methodology is based on on-site experimental work. Data was collected from one simulated leak and one real leak scenarios. The simulated scenario was performed to study the applicability of the proposed methodology under controlled conditions and predefined leaks. The real case scenario, on the other hand, was performed to study the effect of altered conditions surrounding the pipe (emissivity and ambient temperature) on the results and to validate the applicability of the proposed methodology. Two parameters were varied in the scenarios tested: the height of the camera from the ground and the speed of the camera. Table 8 summarizes the different combinations studied.

Once the images were collected by the IR camera, the scale of each image was adjusted to obtain a strong color contrast. The resolution of the used IR camera is 384 x 288 pixels, which means that each image was translated to 110,592 temperature data points. The thermographic images were statistically analyzed using analysis of variance (ANOVA) and pairwise comparison methods. In the ANOVA analysis that was performed using R-studio and Minitab softwares, the mean temperature of each image was compared with the mean temperature of the whole set. If the null hypothesis (H_o: equal mean temperatures throughout ($\mu_1 = \mu_2 = \ldots = \mu_n$ where n: is the number of thermographic images in a set) is rejected this could be an indication of a leak existence. The failure to reject the null hypothesis means that equal mean temperatures exist which indicates that no leak is present, and no temperature contrast will be recorded. Based on the test statistics that resulted from the ANOVA analysis enough evidence was obtained to reject or not to reject the null hypothesis. After the ANOVA analysis, the pair-wise comparison proceeded to identify the location of the leak. A pairwise comparison between the mean temperatures of each image within the same set was performed using a Tukey procedure in Minitab, and the differences were summed up for each image.

The most suitable operating conditions of the IR camera regarding detecting and locating water leaks were determined in all scenarios. Finally, a validation of the proposed methodology was done by comparing detected leak locations and the actual leak location. The methodology of the study is described in Figure 17.

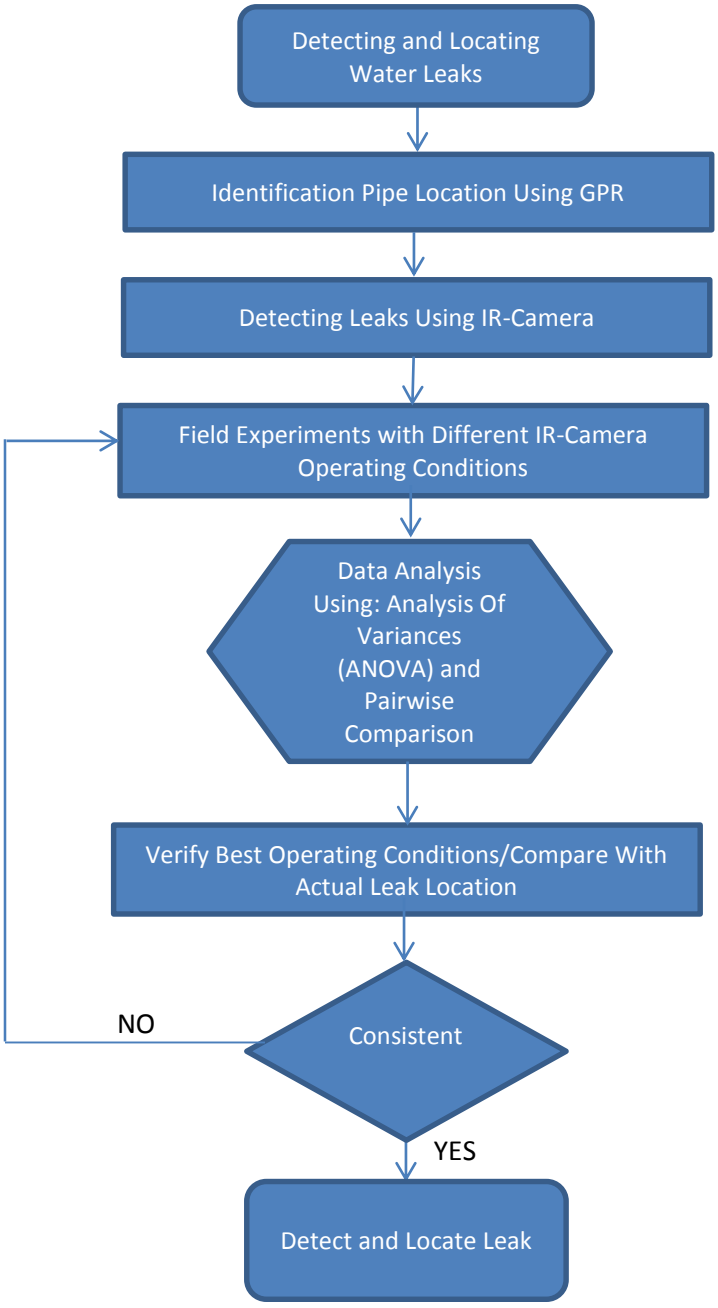

Figure 17. Proposed methodology of method 1

Four operating conditions were developed as summarized in Table 7.

Table 7. IR camera experimental operating conditions

Operating Condition	Height from ground surface (m)	Speed (km/h)	Number of frames
1	1	2	1 (frame/second)
2	2	5	
3	1	5	
4	2	2	

3.2 Method Two (GPR)

In method two only ground penetrating radar was utilized for the prediction of both pipe and leak locations.

3.2.1 Radargram Refinement

Method two starts with collecting GPR profiles along the pipeline length. After collecting the required profiles, the raw data need to be refined. The refinement process

Includes removing diffractions and modifying the effects of dipping layers (also known as migration). The refinement process was implemented using Reflex2DQuick software.

Migration is a process that shifts dipping reflectors to their proper position on the subsurface and collapses hyperbolic diffractions. Hyperbolic reflectors may appear as a sign of the existence of objects with finite dimensions. Shallower objects and steeply dipping surfaces are two reasons that may cause misinterpretation of the size and geometry of subsurface objects. Radar energy may be diffracted as a result of steeply dipping surfaces. Also shallower objects may obscure deeper objects that appear as interfering hyperbolic reflectors.

In this study fk migration technique that is also known as Stolt migration has been implemented to enhance efficiently and mute the irritating subsurface reflections and pulses, create more interpretable and cohesive radargram images and improve wave traces. fk migration technique is a rapid 2D migration method based on performing a constant velocity and it works in the frequency-wavenumber range[56]. In case of GPR data analysis, constant propagation velocity of the electromagnetic waves had been calculated through Equation 3.1 [54]:

$$V = c/\sqrt{\varepsilon} \quad (3.1)$$

Where V is the propagation velocity , c is the speed of light in air (0.3m/ns) and ε is the material dielectric constant.

Figure 18 shows the difference between the raw radargram data and the refined data (after migration).

Additional refinement includes eliminating the undesirable features of the radargram profile such as the area of the ground surface (separation between the antenna and the ground surface). This area is illustrated by the negative values of the depth scale. Those anomalies were processed using the static correction function. As mentioned earlier, electromagnetic properties of the scanned medium or mediums identify the nature of the reflected GPR waves (signatures). Signatures such as reflection strength, polarity, signal attenuation, two-way travel time and hyperbolic reflection are fundamental for the qualification and identification of subsurface features.

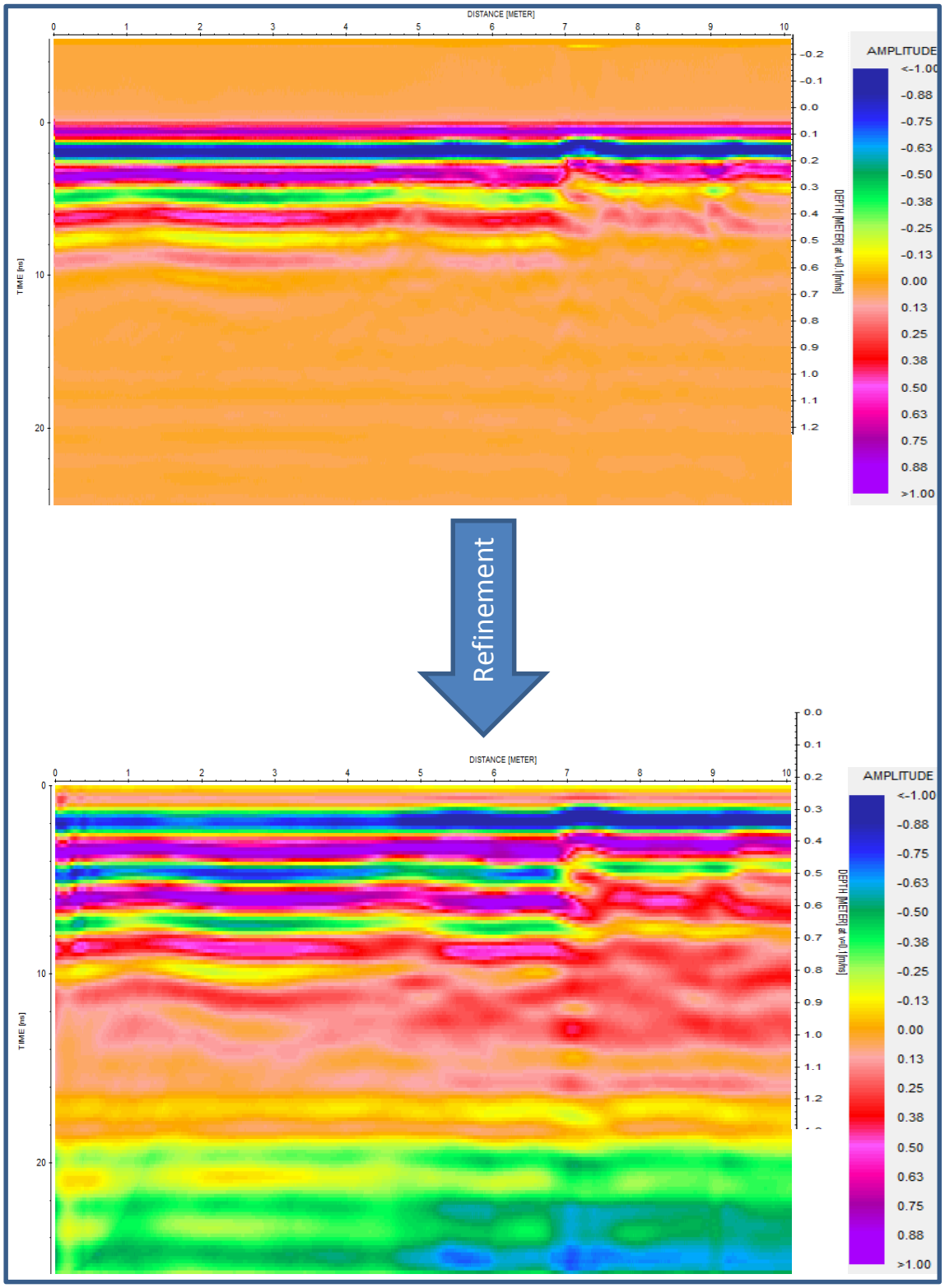

Figure 18. Difference between the raw radargram data and the refined data (after migration)

Table 8 summarizes the main features of the proposed two methods .

Table 8. Features summary of method 1 and 2

Method 1 (GPR+IR)	Method 2 (GPR)
GPR is used for pipe exploration only	GPR is used for subsurface exploration
IR is the leak detector	GPR is the leak detector
Depends on temperature contrast	Depends on electromagnetic properties contrast
Sensitive to weather conditions	Sensitive to ground conditions(soil type, soil composition)
Statistical based technique	Visual based technique
modify operating conditions for better results	modify migrations options for better results

Chapter 4: Results and Discussion

4.1 Method 1

4.1.1 Simulated leak

In the first phase of the study, a leak from a 1 inch (2.5 cm) diameter PVC pipe was simulated under specific controlled conditions to verify the applicability of the proposed methodology. The pipe was 16.5 m long and was buried at a 0.9 m depth surrounded by clayey soil. The leak was simulated by wetting a specific location along the length of the pipe. The wetted location had a wetted area with a radius of around 50 cm Figure 19. The temperature of the water used in the simulated leak was 23^{o}C, while the ground surface and the ambient air temperatures were 35 ^{o}C and 32 ^{o}C respectively. The relative humidity was 55%. The GPR was utilized to identify accurately the location of pipes under the surface by moving in a specific path where it had to intercept perpendicularly with the expected location of the pipe at several points as shown in Figure 20(A). The location of the pipe is indicated by the hyperbola as shown in Figure 20(B). After defining the exact location of the pipe, thermo-graphic images of the ground surface above the pipeline were taken under the different studied operating conditions. Four sets of images, corresponding to four different operating conditions were collected.

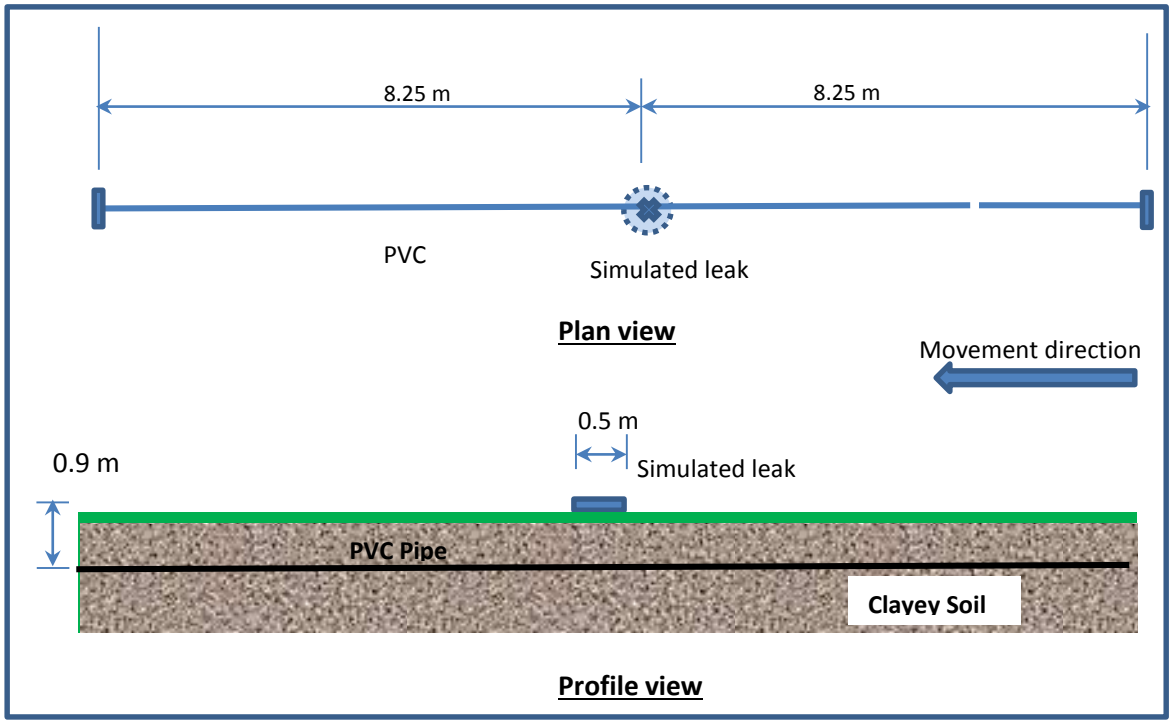

Figure 19. Simulated leak experimental layout

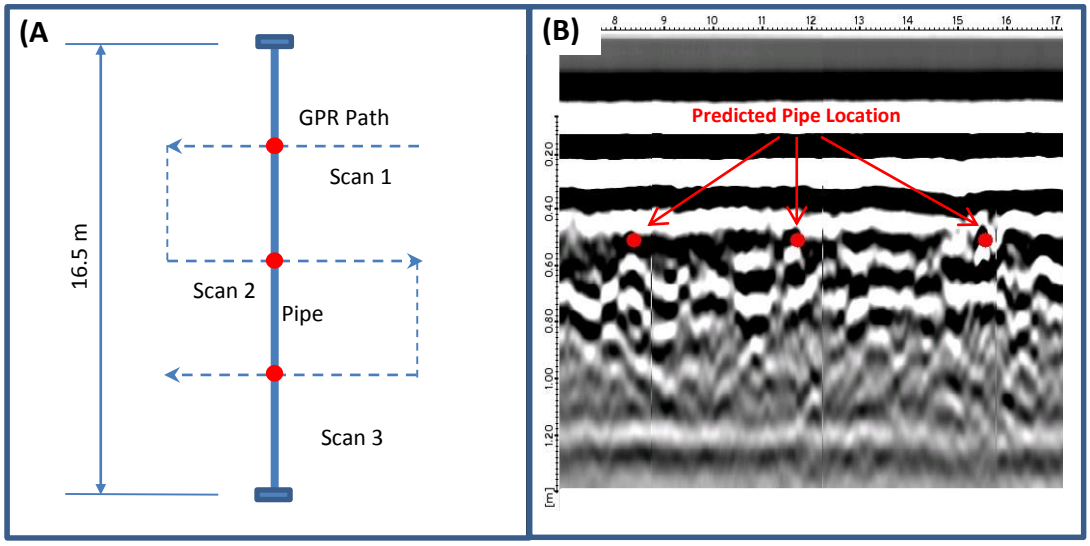

Figure 20. (A) Profile of the subsurface using the MALÅ Ground Penetrating Radar (GPR) equipped with the 500 MHz shielded antenna, location of the pipe is indicated by the hyperbola indicated by the red dots (B) Path of the GPR on top of the buried pipe

4.1.1.1 Operating Condition 1

At a height of 1 meter and speed of 2 km/h the first trial of thermography was performed resulting in 15 thermal images distributed along the 16.5 meters pipe. After collecting the IR images, their scale was adjusted to obtain a strong color contrast. As shown in Figure 21(A) the color degradation for the simulated leak ranged from pink (37^{o}C), representing the highest temperature, to blue, representing the lowest temperature (26^{o}C). Since the temperature of the water used to simulate the leak (i.e. 24^{o}C) was less than the surrounding ground surface temperature, the orange color in Figure 21(B) could represent the leak. In the same manner, the scale of images collected from each operating condition was adjusted.

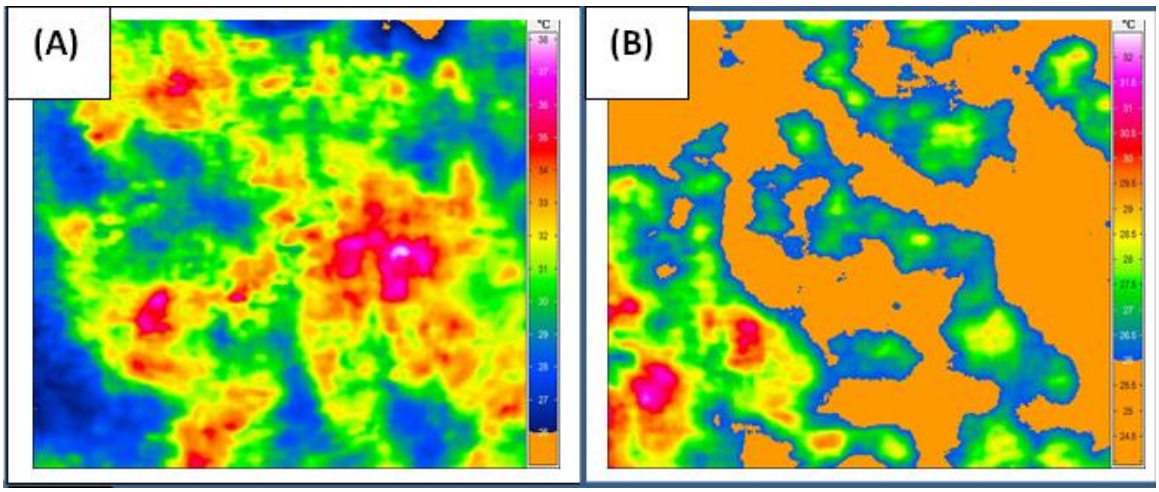

Figure 21. (A) IR image for simulated leak case study “dry location” (B) IR image for simulated leak case study “wet location”

4.1.1.1.1 ANOVA

The existence of a leak throughout the whole set of collected images will be a function of the mean temperature differences between images of the same set. An Analysis of the Variance (ANOVA) was performed on the set of the IR images. In the ANOVA analysis, the temperature of each image was compared with the mean temperature of each image in the whole set. As mentioned earlier if the null hypothesis (H_o: equal mean temperatures throughout ($\mu_1 = \mu_2 = \ldots = \mu_n$ where n: is the number of thermographic images in a set)) is rejected this could be an indication of a leak existence. The failure to reject the null hypothesis means that equal mean temperatures exist which indicates that no leak is present, and no temperature contrast will be recorded.

Test statistics associated with the ANOVA Table 9 showed a probability value of zero as shown in Table 11. In other words the calculated p-value was less than the significant level of the test (p-value$< \alpha=0.05$) thus, enough evidence exists to reject the null hypothesis (H_o). This means that there is a difference between the mean temperatures of the collected thermal images, which could indicate the existence of a leak.

Table 9. Test statistics of O.C.1 of the simulated leak

	Degree of freedom	sum square	mean square	F-value	P-value
Image.ID	14	5513	393.8	1024	0.00<0.05
Residuals	8625	3316	0.4		

4.1.1.1.2 Pairwise Comparison

Pairwise comparison between the mean temperatures of each image within the same set was performed using a Tukey procedure in Minitab, and the differences were summed up for each image. Thermal images with the increasing trend were considered as the leak location. Pairwise comparison table 10 illustrates the results where the first column encompasses the values of the mean temperatures subtraction between thermal image number 1 and all the other images and so on for the other columns.

Table 4. Pair wise comparison of O.C.1 for the simulated leak

Images	1	2	3	4	5	6	7	8	9	10	11	12	13	14	15
1	0	0.049	1.295	1.397	1.051	0.223	0.169	0.554	1.55	0.913	0.28	1.655	1.273	0.927	0.914
2	0.049	0	1.246	1.348	1.561	0.173	0.177	0.505	1.501	0.864	0.225	1.406	1.004	0.878	0.865
3	1.295	1.246	0	0.102	0.313	0.927	0.873	1.259	0.255	0.618	0.985	0.659	0.0223	0.368	1.618
4	1.397	1.348	0.102	0	0.211	0.826	0.772	1.157	0.153	0.516	0.883	0.258	0.124	0.471	1.517
5	1.051	1.561	0.313	0.211	0	0.614	0.561	0.946	0.0586	0.304	0.671	0.246	0.646	0.65	1.305
6	0.223	0.173	0.927	0.826	0.614	0	0.122	1.331	1.673	1.311	0.575	0.768	0.951	1.301	0.891
7	0.169	0.177	0.873	0.772	0.561	0.122	0	2.385	2.619	2.256	2.111	3.011	2.869	3.242	1.745
8	0.554	0.505	1.259	1.157	0.946	1.331	2.385	0	1.004	1.641	1.274	1.899	2.281	2.627	2.021
9	1.55	1.501	0.255	0.153	0.0586	1.673	2.619	1.004	0	2.363	2.731	2.105	1.552	1.623	1.363
10	0.913	0.864	0.618	0.516	0.304	1.311	2.256	1.641	2.363	0	0.367	0.258	0.641	0.986	1.001
11	0.28	0.225	0.985	0.883	0.671	0.575	2.111	1.274	2.731	0.367	0	0.127	0.645	0.353	0.214
12	1.655	1.406	0.659	0.258	0.246	0.768	3.011	1.899	2.105	0.258	0.127	0	0.065	0.121	0.0122
13	1.273	1.004	0.0223	0.124	0.646	0.951	2.869	2.281	1.552	0.641	0.645	0.065	0	0.0212	0.058
14	0.927	0.878	0.368	0.471	0.65	1.301	3.242	2.627	1.623	0.986	0.353	0.121	0.0212	0	0.054
15	0.914	0.865	1.618	1.517	1.305	0.891	1.745	2.021	1.363	1.001	0.214	0.0122	0.058	0.054	0

Summing up all the differences as shown in Table (11) showed that thermal images number 7,8 and 9 gained the highest summation among the others, accordingly, it can be claimed that the leak source was found to be at a distance of 8.25meter from the beginning of the scanned pipe, which was calculated as follows:

$$\frac{(6.6 + 7.7 + 8.8 + 9.9)}{4} = 8.25m$$

A graphical representation of the total mean temperature differences is illustrated in Figure 22, showing a temperature contrast oscillation along the pipeline length and a sudden increase between 6.6m to 11 m.

Table 5. Scoring table of O.C.1 for the simulated leak

Image Boundaries(m)		Images	Total score
0	1.1	1	12.25
1.1	2.2	2	11.802
2.2	3.3	3	10.5403
3.3	4.4	4	9.735
4.4	5.5	5	9.1376
5.5	6.6	6	11.686
6.6	7.7	7	22.912
7.7	8.8	8	20.884
8.8	9.9	9	20.5506
9.9	11	10	14.039
11	12.1	11	11.441
12.1	13.2	12	12.5902
13.2	14.3	13	12.1525
14.3	15.4	14	13.6222
15.4	16.5	15	13.5782

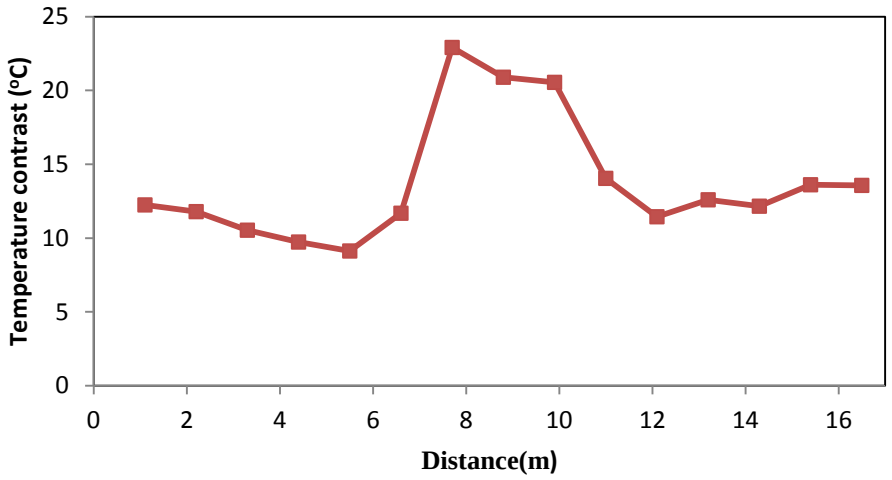

Figure 22. Distance-Temperature contrast relation of O.C.1 for the simulated leak

The accuracy of the processes was checked by comparing the predicted leak location with the actual leak location. The actual leak location was at the center of the pipe at 8.25 m. The predicted leak was at thermal images 7, 8 and 9 which represents a distance from 6.6 m to 9.9 m as shown in Figure 23. Consequently, the center of the predicted leak is 8.25 meters away from the pipe beginning, so the accuracy of the proposed operating combination is given by:

$$\text{Approach accuracy} = 1 - \frac{leak(measured) - (center\ the\ predicted\ leak)}{pipe\ length} = 1 - \frac{8.25 - 8.25}{16.5} = 100\%$$

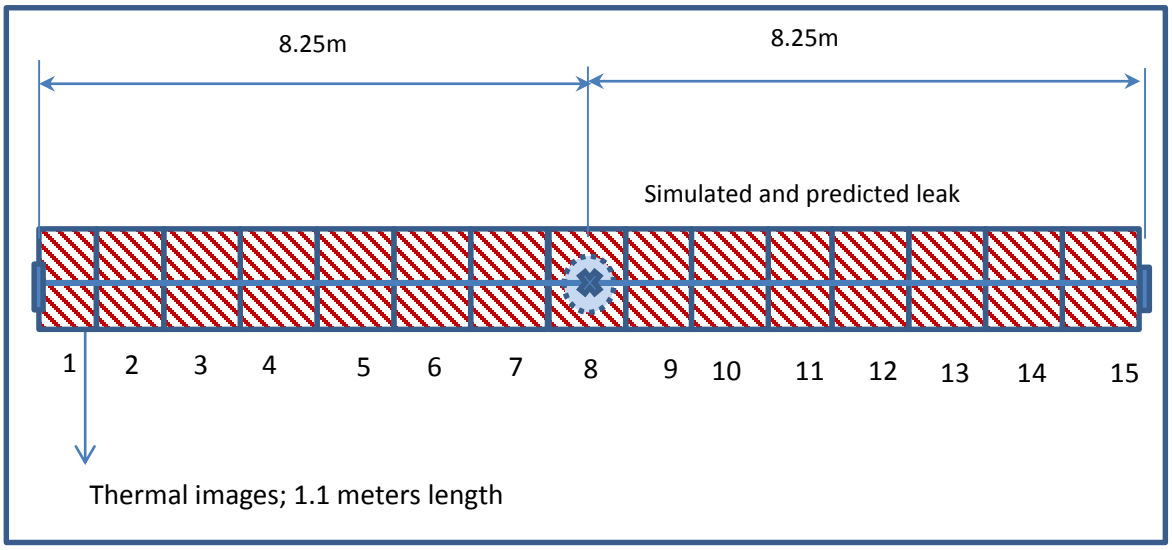

Figure 23. Predicted leak location using O.C.1 of simulated leak case

Characteristics and results of the performed experiment are summarized in Table (12)

Table 12. Characteristics and results of O.C.1-simulated leak

Apparatus used	**GPR: pipe locator**
	IR: Leak detector
no. of thermal images	15
ANOVA	
P-value	0.00<0.05 proceed to the pairwise comparison
pairwise	
highest contrast images	Thermal images 7,8,9
predicted leak center	8.25 m
O.C. Accuracy	100%

4.1.1.2 Operating Condition 2

At a height of 2 meters and speed of 5 km/h the first trial of thermography was performed resulting in 10 thermal images distributed along the 16.5 meters pipe as shown in Figure 25.

4.1.1.2.1 ANOVA

Test statistics associated with the ANOVA showed a probability value of zero as shown in Table 13. In other words the calculated p-value was less than the significant level of the test (p-value< α=0.05) thus, enough evidence exists to reject the null hypothesis (H_o). This means that there is a difference between the mean temperatures of the collected thermal images, which could indicate the existence of a leak.

Table 6. Test statistics of O.C.2-simulated leak

	Degree of freedom	sum square	mean square	F-value	P-value
Image.ID	9	1434	159.3	366.8	0.00<0.05
Residuals	5170	2245	0.43		

4.1.1.2.2 Pairwise Comparison

Pairwise comparison table 14 illustrates the results where the first column encompasses the values of the mean temperatures subtraction between thermal image number 1 and all the other images and so on for the other columns.

Table 14. Pairwise comparison of O.C.2-simulated leak

Images	1	2	3	4	5	6	7	8	9	10
1	0	0.776	1.682	1.362	0.401	0.651	0.229	1.109	1.256	1.333
2	0.776	0	0.907	0.586	0.375	0.124	0.547	0.333	0.481	0.557
3	1.682	0.907	0	0.321	1.283	1.032	1.454	0.574	0.423	0.351
4	1.362	0.586	0.321	0	0.961	0.711	1.133	0.253	0.106	0.0292
5	0.401	0.375	1.283	0.961	0	0.251	0.171	0.709	0.856	0.933
6	0.651	0.124	1.032	0.711	0.251	0	0.422	0.458	0.605	0.682
7	0.229	0.547	1.454	1.133	0.171	0.422	0	0.881	1.027	1.104
8	1.109	0.333	0.574	0.253	0.709	0.458	0.881	0	0.147	0.224
9	1.256	0.481	0.423	0.106	0.856	0.605	1.027	0.147	0	0.0766
10	1.333	0.557	0.351	0.0292	0.933	0.682	1.104	0.224	0.0766	0

Unlike O.C. 1, pairwise comparison for O.C.2 data resulted in ambiguous leak location since two thermal images were found to have similar total mean temperature difference. Also total mean temperature difference of the other thermal images were very close Table 15, moreover no ascending trend were noticed which could not give a clear indication of the leak source as can be seen from the graphical representation of the total mean differences in the Figure 24.

Table 15. Scoring table of O.C.2-simulated leak

Image Boundaries(m)		Images	Total score
0	1.65	1	8.799
1.65	3.3	2	4.686
3.3	4.95	3	8.027
4.95	6.6	4	5.4622
6.6	8.25	5	5.94
8.25	9.9	6	4.936
9.9	11.55	7	6.968
11.55	13.2	8	4.688
13.2	14.85	9	4.9776
14.85	16.5	10	5.2898

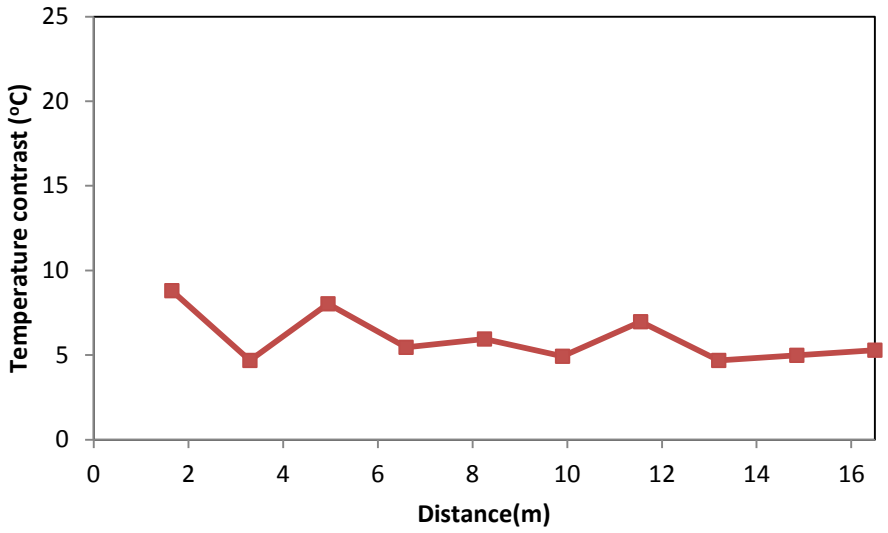

Figure 18. Distance-Temperature contrast relation of O.C.2-simulated leak

Characteristics and results of experiment associated with operating condition 2 are summarized in Table 16.

Table 16. Characteristics and results of O.C.2-simulated leak

Apparatus used	**GPR: pipe locator**
	IR: Leak detector
no. of thermal images	10
ANOVA	
P-value	0.00<0.05 proceed to the pairwise comparison
pairwise	
highest contrast images	Thermal Image 1
predicted leak center	No leak prediction, since the summation of mean temperature differences, are close
O.C. Accuracy	

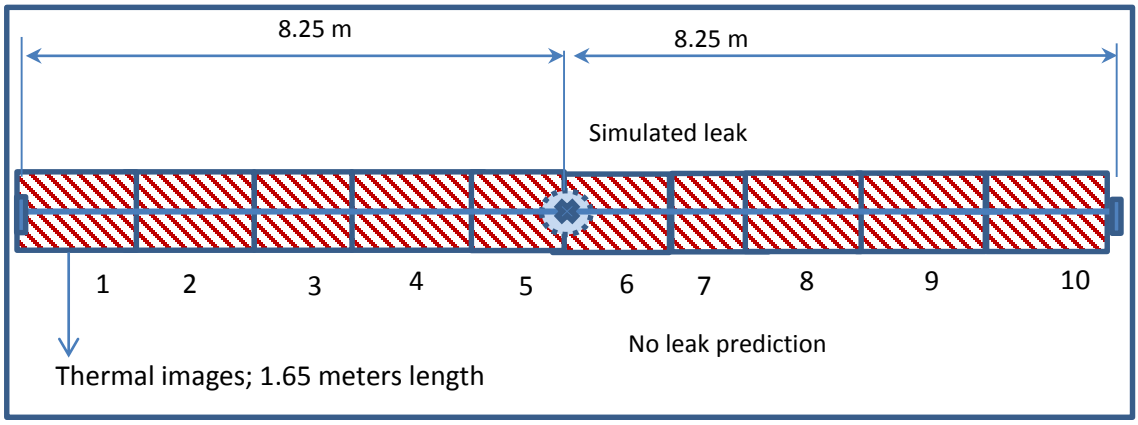

Figure 19. Predicted leak location using O.C.2 of simulated leak case

4.1.1.3 Operating Condition 3

At a height of 1 meter and speed of 5 km/h the first trial of thermography was performed resulting in 9 thermal images distributed along the 16.5 meters pipe as shown in Figure 27.

4.1.1.3.1 ANOVA

Test statistics associated with the ANOVA showed a probability value of zero as shown in Table 17. In other words the calculated p-value was less than the significant level of the test (p-value< α=0.05) thus, enough evidence exists to reject the null hypothesis (H_o). This means that there is a difference between the mean temperatures of the collected thermal images, which could indicate the existence of a leak.

Table 7. Test statistics of O.C.3-simulated leak

	Degree of freedom	sum square	mean square	F-value	P-value
Image.ID	8	3338	417.2	523.3	0.00<0.05
Residuals	5175	4126	0.8		

4.1.1.3.2 Pairwise comparison

Pairwise comparison Table 18 illustrates the results where the first column encompasses the values of the mean temperatures subtraction between thermal image number 1 and all the other images and so on for the other columns.

Table 18. Pairwise comparison of O.C.3-simulated leak

Images	1	2	3	4	5	6	7	8	9
1	0	3.346	0.539	0.00116	0.312	0.141	1.341	1.804	0.867
2	3.346	0	1.807	1.347	2.658	1.486	1.405	1.541	2.713
3	0.539	1.807	0	0.541	0.851	0.679	1.902	1.265	0.906
4	0.00116	1.347	0.541	0	1.311	1.141	1.442	1.806	0.366
5	0.312	2.658	0.851	1.311	0	0.171	1.753	1.116	1.0554
6	0.141	1.486	0.679	1.141	0.171	0	1.582	1.945	1.226
7	1.341	1.405	1.902	1.442	1.753	1.582	0	0.363	1.508
8	1.804	1.541	1.265	1.806	1.116	1.945	0.363	0	1.171
9	0.867	2.713	0.906	0.366	1.0554	1.226	1.508	1.171	0

Summing up all the differences as shown in Table 19 showed that thermal images number 2 gained the highest summation among the others, accordingly, it can be claimed that the leak source was found to be at a distance of 2.75m from the beginning of the scanned pipe. Which was calculated as follows:

$$\frac{1.83 + 3.66}{2} = 2.75m$$

A graphical representation for the total mean temperature differences is illustrated in Figure 26, showing a slight temperature contrast oscillation along the pipeline length, but a dramatic contrast jump between 0m-5.49m .

Table 19. Scoring table of O.C.3-simulated leak

Image Boundaries(m)		Images	Total score
0	1.83	1	8.35116
1.83	3.66	2	16.303
3.66	5.49	3	8.49
5.49	7.32	4	7.95516
7.32	9.15	5	9.2274
9.15	10.98	6	8.371
10.98	12.81	7	11.296
12.81	14.64	8	11.011
14.64	16.47	9	9.8124

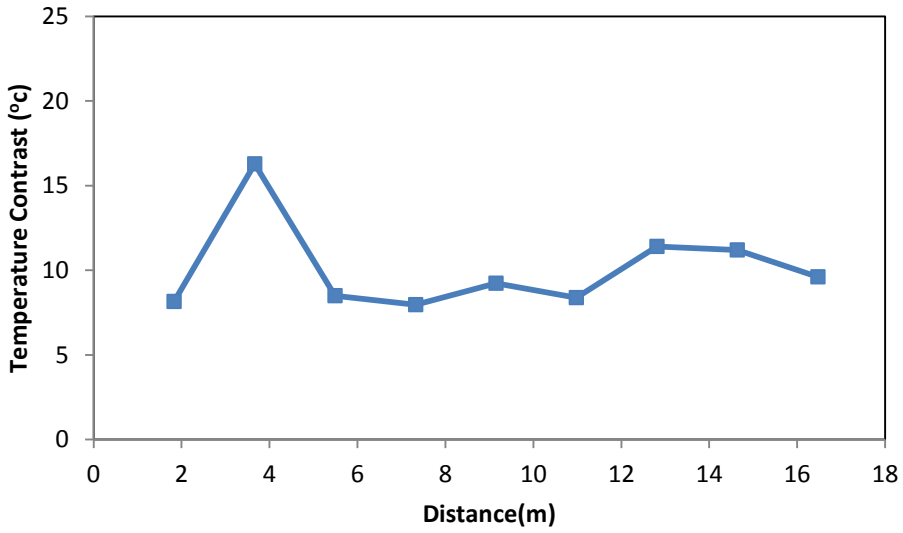

Figure 26. Distance-Temperature contrast relation of O.C.3-simulated leak

The accuracy of the processes was checked by comparing the predicted leak location with the actual leak location. The actual leak location was at the center of the pipe at 8.25 m. The predicted leak was at thermal image 2 which represents a distance from 1.83 m to 3.66 m as shown in Figure 27. Consequently, the center of the predicted leak is 2.75 m away from the pipe beginning, so the accuracy of the proposed operating combination is given by:

Approach accuracy =1- $\frac{leak(measured)-(average\ location\ of\ the\ predicted\ leak)}{pipe\ length}$=$1-\frac{8.25-2.75}{16.5}=66.6\%$

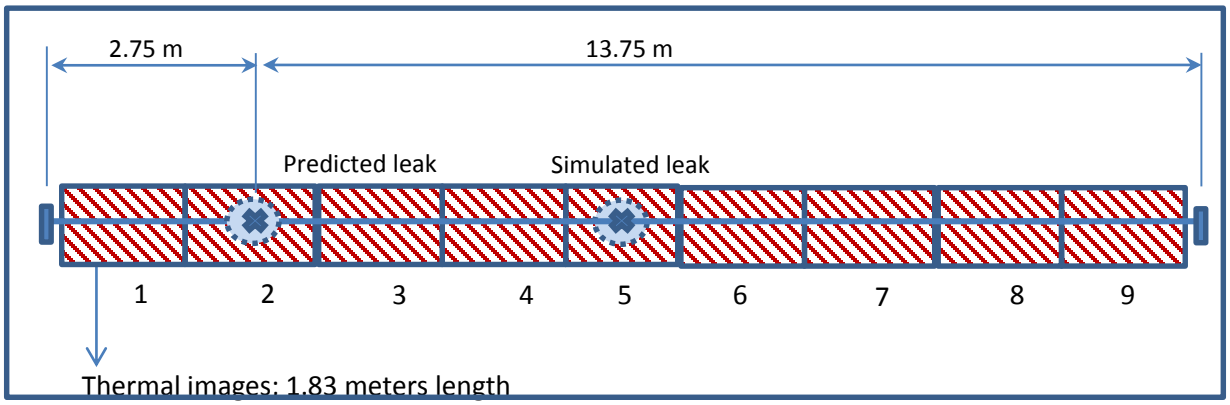

Figure 20. Predicted leak location using O.C.3 of simulated leak case

Characteristics and results of experiment associated with operating condition 2 are summarized in Table 20.

Table 20. Characteristics and results of O.C.3-simulated leak

Apparatus used	**GPR: pipe locator**
	IR: Leak detector
no. of thermal images	9
ANOVA	
P-value	0.00<0.05 proceed to the pairwise comparison
pairwise	
highest contrast images	Thermal Image 2
predicted leak center	2.75 m
O.C. Accuracy	66.6%

4.1.1.4 Operating Condition 4

At a height of 2 meters and speed of 2 km/h the first trial of thermography was performed resulting in 14 thermal images distributed along the 16.5 meters pipe as shown in Figure 29.

4.1.1.4.1 ANOVA

Test statistics associated with the ANOVA showed a probability value of zero as shown in Table 21. In other words the calculated p-value was less than the significant level of the test (p-value< α=0.05) thus, enough evidence exists to reject the null hypothesis (H_o). This means that there is a difference between the mean temperatures of the collected thermal images, which could indicate the existence of a leak.

Table 21. Test statistics of O.C.4-simulated leak

	Degree of freedom	sum square	mean square	F-value	P-value
Image.ID	13	4220	324.6	806.9	0.00<0.05
Residuals	7238	2912	0.4		

4.1.1.4.2 Pairwise comparison

Pairwise comparison Table 22 illustrates the results where the first column encompasses the values of the mean temperatures subtraction between thermal image number 1 and all the other images and so on for the other columns.

Table 8. Pairwise comparison of O.C.4-simulated leak

Images	1	2	3	4	5	6	7	8	9	10	11	12	13	14
1	0	1.528	0.888	0.561	0.631	1.181	0.906	0.633	0.405	0.916	0.137	0.041	0.383	2.036
2	1.528	0	0.959	1.032	1.101	0.652	1.378	1.104	0.877	0.387	0.608	0.0885	0.254	0.508
3	0.888	0.959	0	1.0732	1.142	0.692	0.418	0.146	0.0819	0.571	0.351	1.047	0.704	0.451
4	0.561	1.032	1.0732	0	1.0692	0.619	0.345	0.0723	0.155	0.645	0.424	1.121	0.778	0.524
5	0.631	1.101	1.142	1.0692	0	0.551	0.275	0.003	0.224	0.714	0.493	1.191	0.847	0.594
6	1.181	0.652	0.692	0.619	0.551	0	2.274	2.547	2.774	2.264	2.043	0.141	1.397	1.144
7	0.906	1.378	0.418	0.345	0.275	2.274	0	1.272	0.501	0.991	0.769	0.466	1.122	0.869
8	0.633	1.104	0.146	0.0723	0.003	2.547	1.272	0	0.227	0.717	0.496	0.193	0.851	0.596
9	0.405	0.877	0.0819	0.155	0.224	2.774	0.501	0.227	0	0.489	0.269	0.865	0.622	0.369
10	0.916	0.387	0.571	0.645	0.714	2.264	0.991	0.717	0.489	0	0.221	0.476	0.133	0.121
11	0.137	0.608	0.351	0.424	0.493	2.043	0.769	0.496	0.269	0.221	0	0.697	1.353	0.101
12	0.041	0.0885	1.047	1.121	1.191	0.141	0.466	0.193	0.865	0.476	0.697	0	1.343	0.597
13	0.383	0.254	0.704	0.778	0.847	1.397	1.122	0.851	0.622	0.133	1.353	1.343	0	0.253
14	2.036	0.508	0.451	0.524	0.594	1.144	0.869	0.596	0.369	0.121	0.101	0.597	0.253	0

Summing up all the differences as shown in Table 23 showed that thermal images number 6 gained the highest summation among the others, accordingly, it can be claimed that the leak source was found to be at a distance of 6.49m from the beginning of the scanned pipe, which was calculated as follows:

$$\frac{5.9 + 7.08}{2} = 6.49m$$

A graphical representation of the total mean temperature differences is illustrated in Figure 28, showing a slight temperature contrast oscillation along the pipeline length, but a dramatic contrast jump at image number 6 .

Table 9. Scoring table of O.C.4-simulated leak

Image Boundaries(m)		**Images**	**Total score**
0	1.18	1	10.246
1.18	2.36	2	10.4765
2.36	3.54	3	8.5241
3.54	4.72	4	8.4187
4.72	5.9	5	8.8352
5.9	7.08	6	18.279
7.08	8.26	7	11.586
8.26	9.44	8	8.8573
9.44	10.62	9	7.8589
10.62	11.8	10	8.645
11.8	12.98	11	7.962
12.98	14.16	12	8.2665
14.16	15.34	13	10.04
15.34	16.52	14	8.163

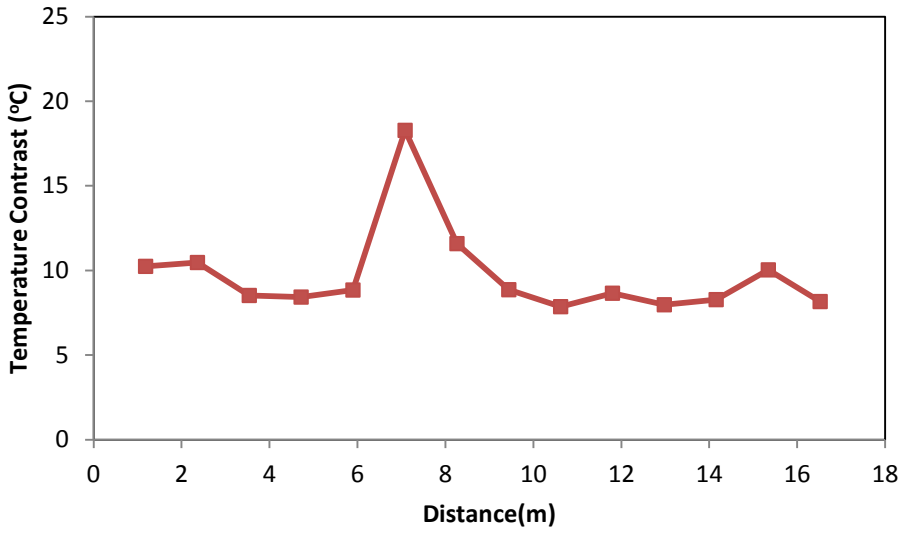

Figure 21. Distance-Temperature contrast relation of O.C.4-simulated leak

The accuracy of the processes was checked by comparing the predicted leak location with the actual leak location. The actual leak location was at the center of the pipe at 8.25 m. The predicted leak was at thermal image 6 which represents a distance from 5.9 m to 7.09 m as shown in Figure 29. Consequently, the center of the predicted leak is 6.49 m away from the pipe beginning, so the accuracy of the proposed operating combination is given by:

Approach accuracy =1- $\frac{leak(measured)-(average\ location\ of\ the\ predicted\ leak)}{pipe\ length}$=$1-\frac{8.25-6.49}{16.5}=$ 89.3%

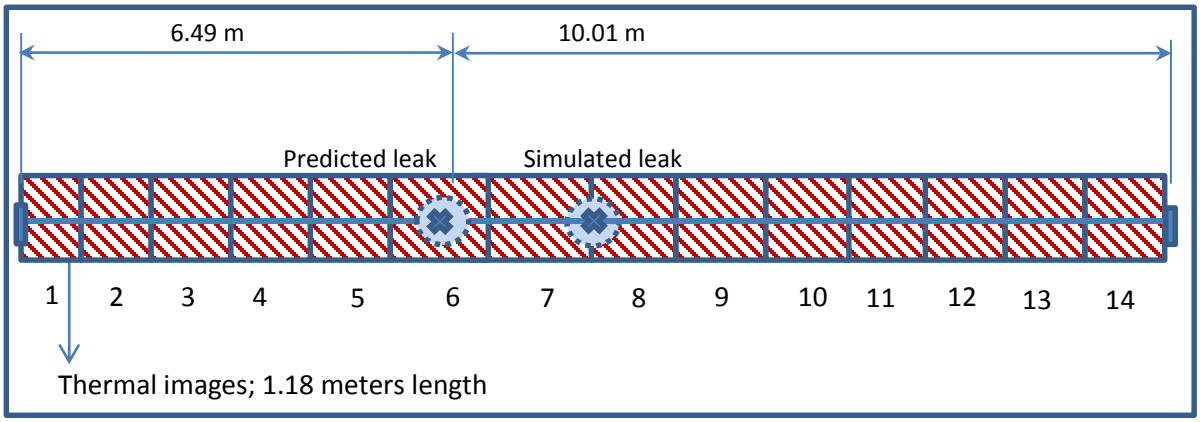

Figure 29. Predicted leak location using O.C.4 of simulated leak case

Characteristics and results of experiment associated with operating condition 2 are Summarized in Table 24.

Table 10. Characteristics and results of O.C.4-simulated leak

Apparatus used	**GPR: pipe locator**
	IR: Leak detector
no. of thermal images	14
ANOVA	
P-value	0.00<0.05 proceed to the pairwise comparison
pairwise	
highest contrast images	Thermal image 6
predicted leak center	6.49 m
O.C. Accuracy	89.3%

4.1.1.5 Summary of Results

Results of the four operating conditions are summarized in Table 25.

Table 11. Simulated leak case result summary

	O.C. 1	**O.C. 2**	**O.C. 3**	**O.C. 4**
Characteristics	1m,2km/h	2m,5km/h	1m,5km/h	2m,2km/h
P-value	<0.05	<0.05	<0.05	<0.05
highest contrast	Thermal Image 7,8,9	Thermal Image 1	Thermal Image 2	Thermal Image 6
Accuracy	100%	N/A	66.60%	89.30%

Performing the four operating conditions on the suspected leak location have yielded different outcomes, where slow speed operating conditions(O.C 1&4) resulted in more accurate results than operating conditions with high speed (O.C 2&3). Operating condition 1 has predicted the leak location exactly at the actual leak location, also operating condition 4 has predicted the leak within a very small error value, however operating condition 2 failed to detect leak since all the temperature contrast values were close and an error value of more than 30% resulted from operating condition 3.Accuracy deviation among the four operating conditions can be attributed to the weathering conditions (ambient temperature, humidity, solar radiation, etc...) and some physical conditions of the experimented media such as emissivity. The interaction between the camera operating conditions and the weathering conditions in addition to surface emissivity will be discussed later.

4.1.2 Real Leak Scenario 1 (Mesaeed location)

In collaboration with Qatar General Electricity and water Corporation (KAHRAMAA), a 10 meter long PVC pipe, buried 0.9 m under the surface and surrounded by crushed sandstone and bricks pavement, was tested. According to KAHRAMAA, the pipeline was experiencing a leak, but the exact location of the leak was unknown. Figure 30 shows the layout of the location of the study area for the real leak scenario. Thermographic images of the ground surface above the pipeline were taken with the different operating conditions. Four sets of images corresponding to each operating condition were collected. After collecting the images, the exact leak location was determined by KAHRAMAA through excavation and visual inspection. The temperature of the dry surface varied between 47

and 50ºC; meanwhile, the ambient air temperature and the relative humidity were 42ºC and 75%, respectively.

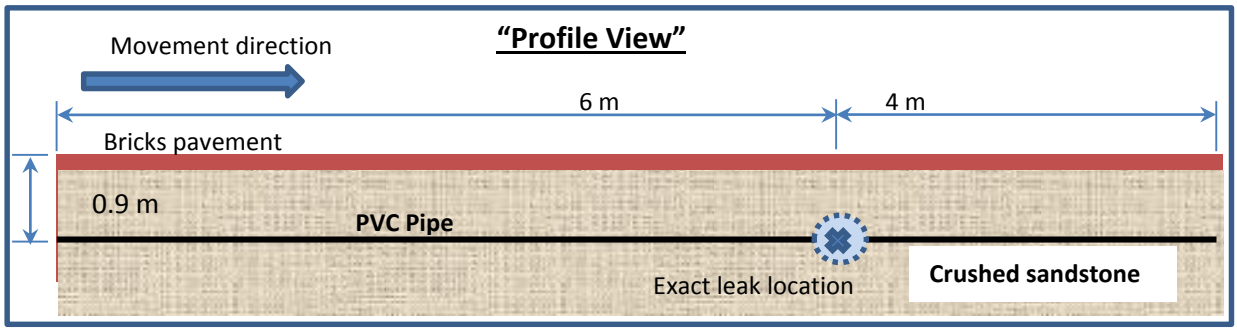

Figure 30. Real leak case 1 layout

4.1.2.1 Operating Condition 1

At a height of 1 meter and speed of 2 km/h the first trial of thermography was performed resulting in 8 thermal images distributed along the 10 meters pipe as shown in Figure 33. After collecting the IR images, their scale was adjusted to obtain a strong color contrast. Figure 31(A) shows that in the case of the real leak, the color degradation was minimal with the color being mainly dark blue. Contrary to that, Figure 31 (B) which represents the location of leak in the real leak case, degradation in color was observed. The temperature of water on the surface due to the real leak (i.e. 51-53oC) was higher than the surrounding ground surface temperature (i.e. 47 – 50oC).

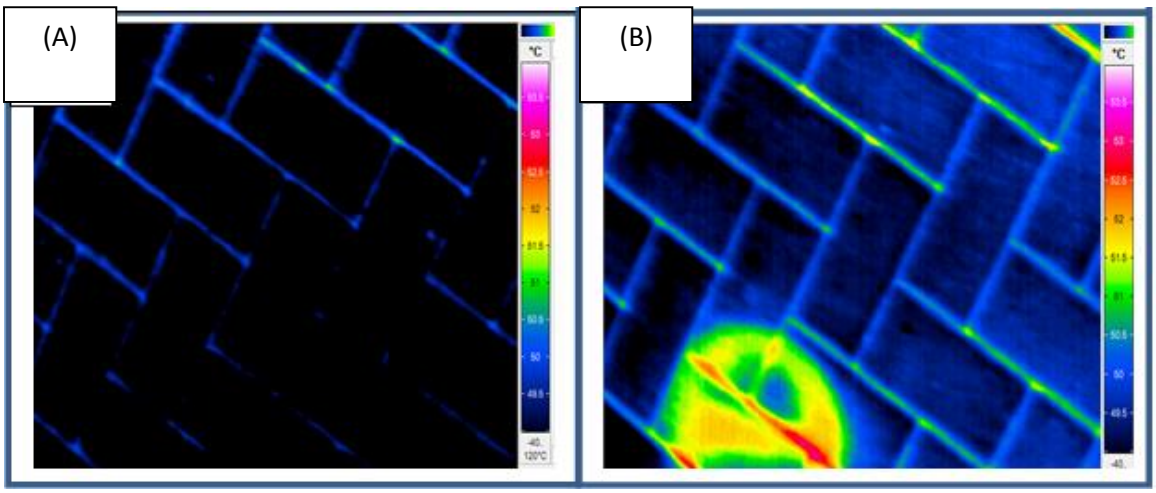

Figure 31. (A) IR image for real leak case study “dry location” (B) IR image for real leak case study “wet location”

4.1.2.1.1 ANOVA

Test statistics associated with the ANOVA showed a probability value of zero as shown in Table 26. In other words the calculated p-value was less than the significant level of the test (p-value< α=0.05) thus, enough evidence exists to reject the null hypothesis (H_o). This means that there is a difference between the mean temperatures of the collected thermal images, which could indicate the existence of a leak.

Table 12 Test statistics of O.C.1-real leak 1

	Degree of freedom	sum square	mean square	F-value	P-value
Image.ID	7	220507	31500.9	103240	0<2e-16
Residuals	858520	261955	0.3		

4.1.2.1.2 Pairwise Comparison

Pairwise comparison Table 27 illustrates the results where the first column encompasses the values of the mean temperatures subtraction between thermal image number 1 and all the other images and so on for the other columns.

Table 13Pairwise comparison of O.C.1- real leak 1

Images	1	2	3	4	5	6	7	8
1	0	0.23766	0.326	0.223	0.258	0.207	0.402	0.85623
2	0.23766	0	0.26352	0.38538	0.3406	0.27031	0.23438	0.91143
3	0.326	0.26352	0	0.1489	0.22412	0.23383	0.30914	1.06791
4	0.223	0.38538	0.1489	0	0.46522	0.33507	0.43976	1.79681
5	0.258	0.3406	0.22412	0.46522	0	0.25029	0.45498	0.63203
6	0.207	0.27031	0.23383	0.33507	0.25029	0	0.80469	1.20174
7	0.402	0.23438	0.30914	0.43976	0.45498	0.80469	0	0.00705
8	0.85623	0.91143	1.06791	1.79681	0.63203	1.20174	0.00705	0

Summing up all the differences as shown in Table 28 showed that thermal images number 8 gained the highest summation among the others, accordingly, it can be claimed that the leak source was found to be at a distance of 9.375 m from the beginning of the scanned pipe, which was calculated as follows:

$$\frac{8.75 + 10}{2} = 9.375m$$

A graphical representation of the total mean temperature differences is illustrated in Figure 32, showing a significant temperature contrast oscillation along the pipeline length, especially between 8.75m to 10m where it increased abnormally.

Table 28. Scoring table of O.C.1- real leak 1

Image Boundaries (m)		Images	Total score
0	1.25	1	2.50989
1.25	2.5	2	2.64328
2.5	3.75	3	2.57342
3.75	5	4	3.79414
5	6.25	5	2.62524
6.25	7.5	6	3.30293
7.5	8.75	7	2.652
8.75	10	8	6.4732

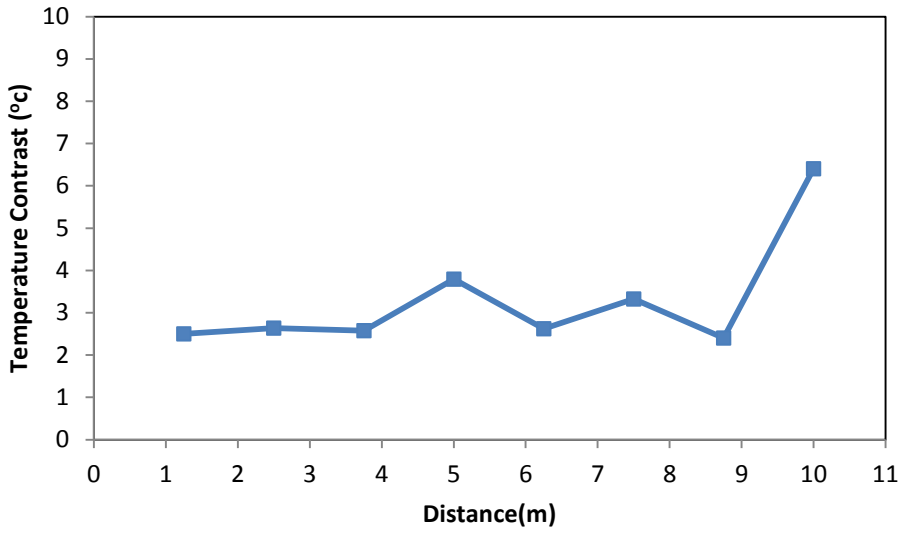

Figure 32. Distance-Temperature contrast relation of O.C.1- real leak 1

The accuracy of the processes was checked by comparing the predicted leak location with the actual leak location. The actual leak location was at the center of the pipe at 6 m. The predicted leak was at thermal image 8 which represents a distance from 8.75 m to 10m as shown in Figure 33. Consequently, the center of the predicted leak is 9.375 m away from the pipe beginning, so the accuracy of the proposed operating combination is given by:

$$\text{Approach accuracy} = 1 - \frac{leak(exact) - (center\ of\ the\ predicted\ leak)}{pipe\ length} = 1 - \left|\frac{6 - 9.375}{10}\right| = 66.25\%$$

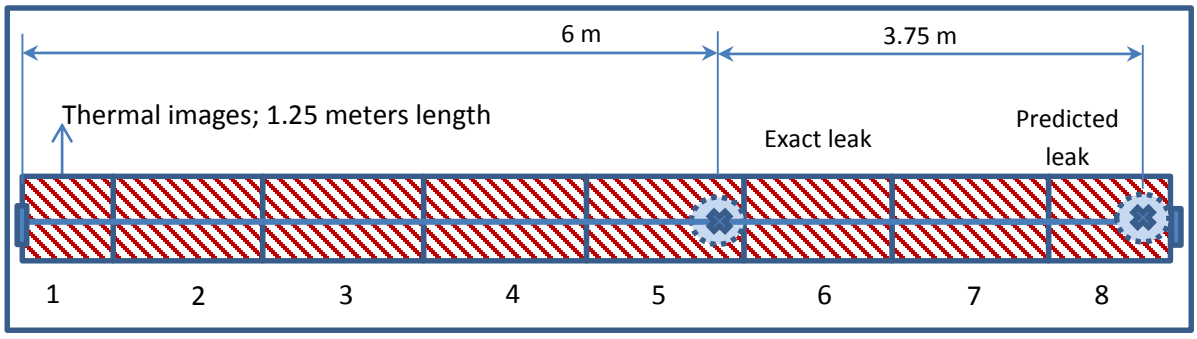

Figure 33. Predicted leak location using O.C.1 of real leak 1case

Table 29. Characteristics and results of O.C.1- real leak 1

Apparatus used	GPR: not used
	IR: Leak detector
no. of thermal images	8
ANOVA	
P-value	0.00<0.05 proceed to the pairwise comparison
pairwise	
highest contrast images	Thermal Image 8
predicted leak center	9.375 m
O.C. Accuracy	66.25%

4.1.2.2 Operating condition 2

At a height of 2 meters and speed of 5 km/h the first trial of thermography was performed resulting in 5 thermal images distributed along the 10 meters pipe as shown in Figure 35.

4.1.2.2.1 ANOVA

Test statistics associated with the ANOVA showed a probability value of zero as shown in Table 30. In other words the calculated p-value was less than the significant level of the test (p-value< α=0.05) thus, enough evidence exists to reject the null hypothesis (H_o). This means that there is a difference between the mean temperatures of the collected thermal images, which could indicate the existence of a leak.

Table 30. Test statistics of O.C.2-real leak 1

	Degree of freedom	sum square	mean square	F-value	P-value
Image.ID	4	23627	5906.79	13494.10	0.00<0.05
Residuals	416630	182372	0.44		

4.1.2.2.2 Pairwise Comparison

Pairwise Comparison Table 31 illustrates the results where the first column encompasses the values of the mean temperatures subtraction between thermal image number 1 and all the other images and so on for the other columns.

Table 14. Statistics of O.C.2-real leak 1

Images	1	2	3	4	5
1	0	0.29609	0.59694	0.04689	0.02781
2	0.29609	0	0.30085	0.24921	0.3239
3	0.59694	0.30085	0	0.55006	0.62475
4	0.04689	0.24921	0.55006	0	0.07469
5	0.02781	0.3239	0.62475	0.07469	0

Summing up all the differences as shown in Table (32) showed that thermal images number 3 gained the highest summation among the others, accordingly, it can be claimed that the leak source was found to be at a distance of 5 m from the beginning of the scanned pipe. which was calculated as follows:

$$\frac{4+6}{2} = 5m$$

A graphical representation of the total mean temperature differences is illustrated in Figure 34, showing a slight difference in temperature contrast along the pipeline length, except between 4m to 6m where a sudden increase noticed.

Table 15. Scoring table of O.C.2- real leak 1

Image Boundaries (m)		Images	Total score
0	2	1	0.96773
2	4	2	1.17005
4	6	3	2.0726
6	8	4	0.92085
8	10	5	1.05115

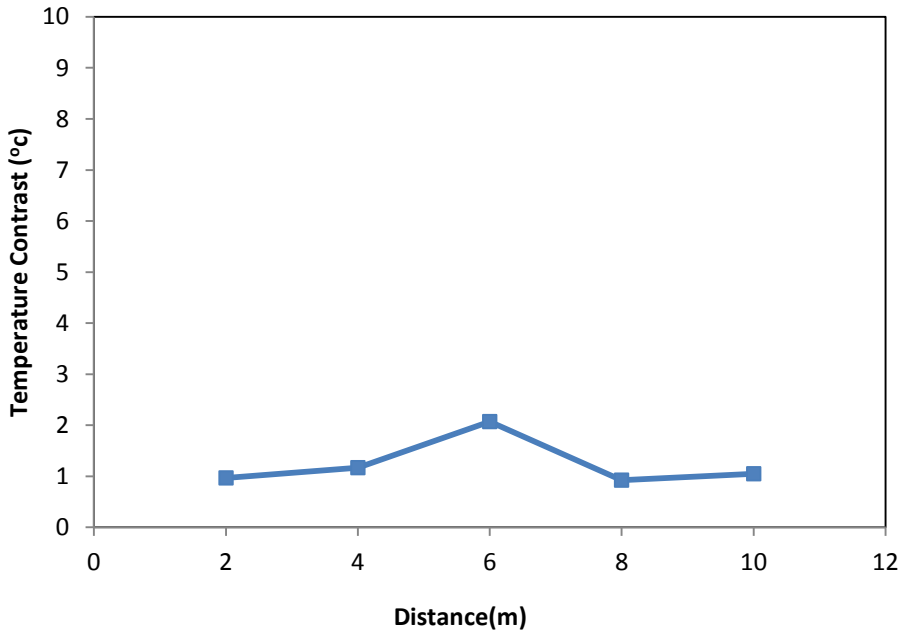

Figure 34. Distance-Temperature contrast relation of O.C.2- real leak 1

The accuracy of the processes was checked by comparing the predicted leak location with the actual leak location. The actual leak location was at the center of the pipe at 6 m. The predicted leak was at thermal image 3 which represents a distance from 4 m to 6m as shown in Figure 35. Consequently, the center of the predicted leak is 5 m away from the pipe beginning, so the accuracy of the proposed operating combination is given by:

Approach accuracy =1- $\frac{leak(exact)-(average\ location\ of\ the\ predicted\ leak)}{pipe\ length}$=$1-\frac{6-5}{10}=90\%$

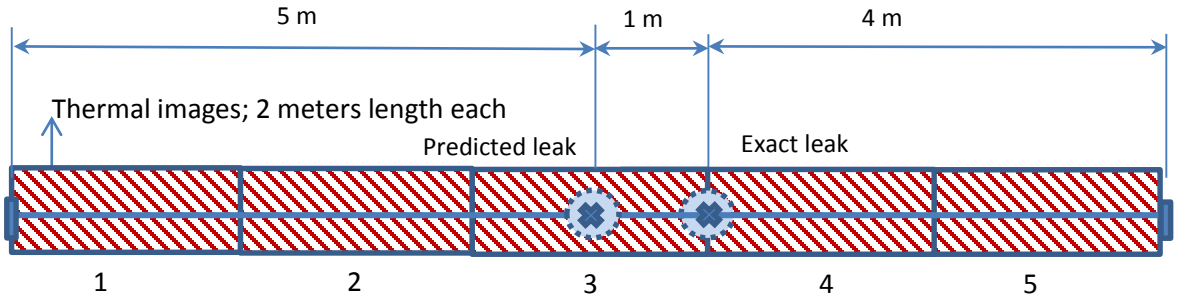

Figure 35. Predicted leak location using O.C.2 of real leak 1case

Characteristics and results of the performed experiment are summarized in Table 33.

Table 16. Characteristics and results of O.C.2- real leak 1

Apparatus used	**GPR: not used**
	IR: Leak detector
no. of thermal images	5
ANOVA	
P-value	0.00<0.05 proceed to the pairwise comparison
pairwise	
highest contrast images	Thermal Image 3
predicted leak center	5 m
O.C. Accuracy	90%

4.1.2.3 Operating Condition 3

At a height of 1 meter and speed of 5 km/h the first trial of thermography was performed resulting in 5 thermal images distributed along the 10 meters pipe as shown in Figure 37.

4.1.2.3.1 ANOVA

Test statistics associated with the ANOVA Table 34 showed a probability value close to be zero, in other words the calculated p-value was less than the significant level of the test (p-value< α=0.05) thus enough evidence were existed to reject the null hypothesis(H_o) which claimed that there are no differences between the mean temperature of the collected thermal images.

Table 17. Test statistics of O.C3-real leak 1

	Degree of freedom	sum square	mean square	F-value	P-value
Image.ID	4	87311	21827.7	77780.8	0.00<0.05
Residuals	326690	91679	0.3		

4.1.2.3.2 Pairwise Comparison

Pairwise Comparison Table 35 illustrates the results where the first column encompasses the values of the mean temperatures subtraction between thermal image number 1 and all the other images and so on for the other columns.

Table 18. Pairwise comparison of O.C.3- real leak 1

Images	1	2	3	4	5
1	0	0.1236	0.857	0.9044	0.0358
2	0.1236	0	0.73372	0.78077	0.08781
3	0.857	0.73372	0	0.04705	0.82153
4	0.9044	0.78077	0.04705	0	0.86858
5	0.0358	0.08781	0.82153	0.86858	0

Summing up all the differences as shown in Table 36 showed that thermal images number 3 and 4 gained the highest summation among the others, accordingly, it can be claimed that

the leak source was found to be at a distance of 6 m from the beginning of the scanned pipe, which was calculated as follows:

$$\frac{4+8}{2} = 6m$$

A graphical representation of the total mean temperature differences is illustrated in Figure 36, showing a moderate difference in temperature contrast along the pipeline length, especially between 4m to 8m.

Table 19. Scoring table of O.C.3- real leak 1

Image Boundaries(m)		Images	Total score
0	2	1	1.9208
2	4	2	1.725
4	6	3	2.4593
6	8	4	2.6008
8	10	5	1.81372

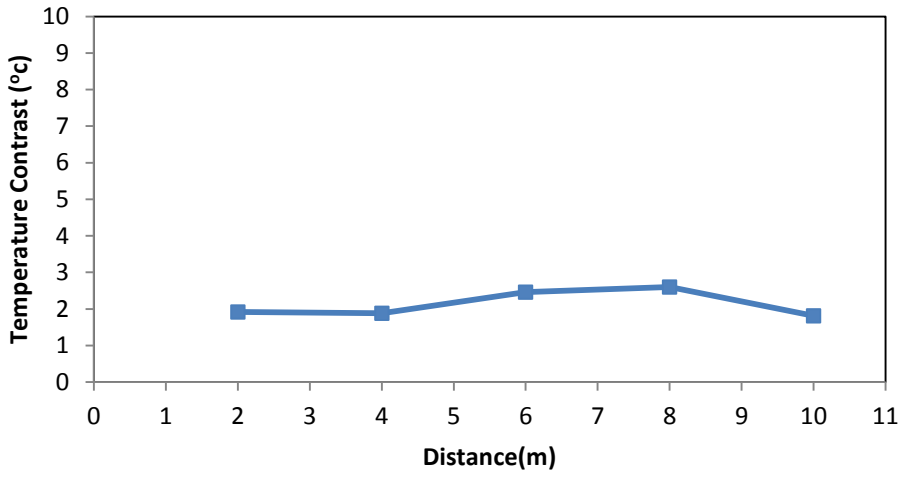

Figure 36. Distance-Temperature contrast relation of O.C.3- real leak 1

The accuracy of the processes was checked by comparing the predicted leak location with the actual leak location. The actual leak location was at the center of the pipe at 6 m. The predicted leak was at thermal images 3 and 4 which represent a distance from 4 m to 6m as shown in Figure 37. Consequently, the center of the predicted leak is 6 m away from the pipe beginning, so the accuracy of the proposed operating combination is given by:

$$\text{Approach accuracy} = 1 - \frac{leak(exact) - (center\ of\ the\ predicted\ leak)}{pipe\ length} = 1 - \frac{6-6}{10} = 100\%$$

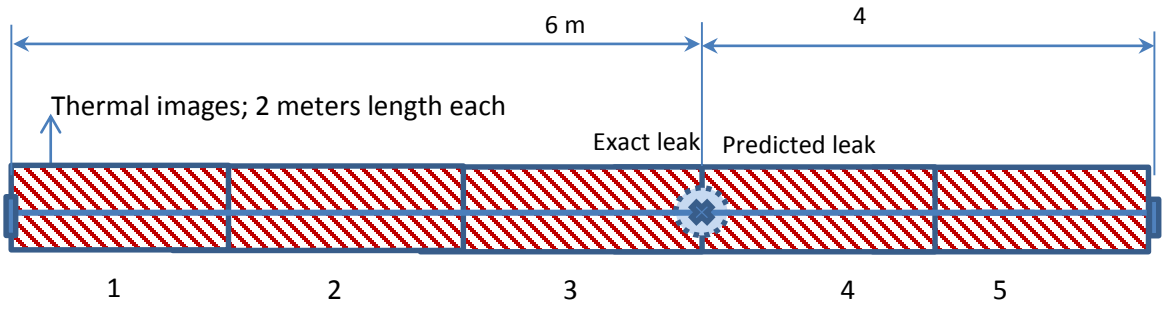

Figure 37. Predicted leak location using O.C.3 of real leak 1case

Characteristics and results of the performed experiment are summarized in Table 37.

Table 20. Characteristics and results of O.C.3- real leak 1

Apparatus used	**GPR: not used**
	IR: Leak detector
no. of thermal images	5
ANOVA	
P-value	0.00<0.05 proceed to the pairwise comparison
pairwise	
highest contrast images	Thermal image 3,4
predicted leak center	6 m
O.C. Accuracy	100%

4.1.2.4 Operating condition 4

At a height of 2 meters and speed of 2 km/h the first trial of thermography was performed resulting in 7 thermal images distributed along the 10 meters pipe as shown in Figure 39.

4.1.2.4.1 ANOVA

Test statistics associated with the ANOVA Table 38 showed a probability value close to be zero, in other words the calculated p-value was less than the significant level of the test (p-value< α=0.05) thus enough evidence were existed to reject the null hypothesis (H_o) which claimed that there are no differences between the mean temperature of the collected thermal images.

Table 38. Test statistics of O.C4-real leak 1

	Degree of freedom	sum square	mean square	F-value	P-value
Image.ID	7	62623	8946.16	21142.04	0.00<0.05
Residuals	566832	239852	0.42		

4.1.2.4.2 Pairwise Comparison

Pairwise Comparison Table 39 illustrates the results where the first column encompasses the values of the mean temperatures subtraction between thermal image number 1 and all the other images and so on for the other columns.

Table 39. Pairwise comparison of O.C.4- real leak 1

Images	1	2	3	4	5	6	7	8
1	0	0.31548	0.04806	0.10641	0.4286	0.34974	0.92375	0.07108
2	0.31548	0	0.06354	0.08189	0.10408	0.30522	0.90923	0.14439
3	0.04806	0.06354	0	0.45835	0.38054	0.20168	0.97569	0.31915
4	0.10641	0.08189	0.45835	0	0.12219	0.14333	0.51266	0.9075
5	0.4286	0.10408	0.38054	0.12219	0	0.38114	0.20485	0.44969
6	0.34974	0.30522	0.20168	0.14333	0.38114	0	0.22598	0.42082
7	0.92375	0.90923	0.97569	0.51266	0.20485	0.22598	0	0.49484
8	0.07108	0.14439	0.31915	0.9075	0.44969	0.42082	0.49484	0

Summing up all the differences as shown in Table 40 showed that thermal image number 7 gained the highest summation among the others, accordingly, it can be claimed that the leak source was found to be at a distance of 8.125 m from the beginning of the scanned pipe, which was calculated as follows:

$$\frac{7.5 + 8.75}{2} = 8.125m$$

A graphical representation of the total mean temperature differences is illustrated in Figure 38, showing a slight difference in temperature contrast along the pipeline length, except at image 7 that experienced a sudden increase.

Table 21. Scoring table of O.C.4- real leak 1

Image Boundaries (m)		Images	Total score
0	1.25	1	2.243
1.25	2.5	2	1.923
2.5	3.75	3	2.447
3.75	5	4	2.332
5	6.25	5	2.071
6.25	7.5	6	2.027
7.5	8.75	7	4.247
8.75	10	8	2.807

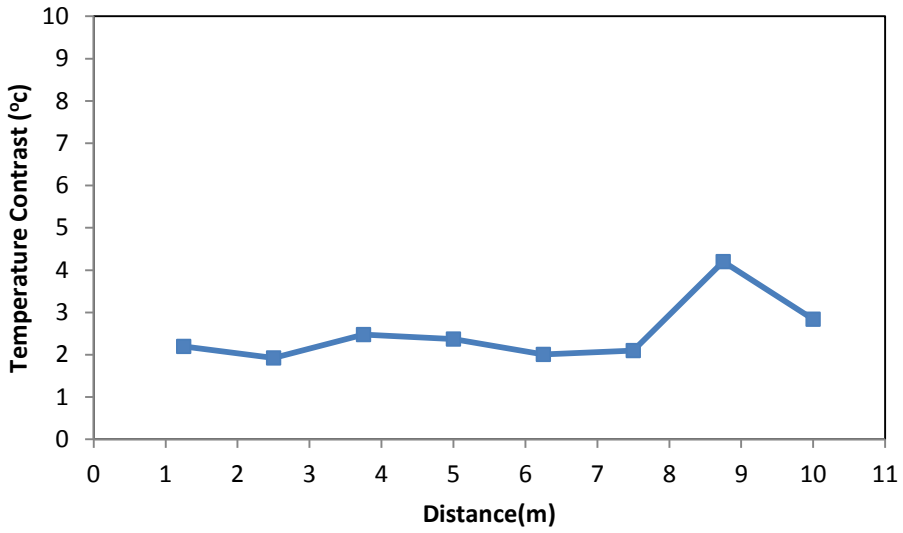

Figure 38. Distance-Temperature contrast relation of O.C.4- real leak 1

The accuracy of the processes was checked by comparing the predicted leak location with the actual leak location. The actual leak location was at the center of the pipe at 6 m. The predicted leak was at thermal 7 which represent a distance from 7.5 m to 8.75 m as shown in Figure 39. Consequently, the center of the predicted leak is 8.125 m away from the pipe beginning, so the accuracy of the proposed operating combination is given by:

$$\text{Approach accuracy} = 1 - \frac{leak(exact) - (center\ of\ the\ predicted\ leak)}{pipe\ length} = 1 - \left|\frac{6 - 8.125}{10}\right| = 78.7\%$$

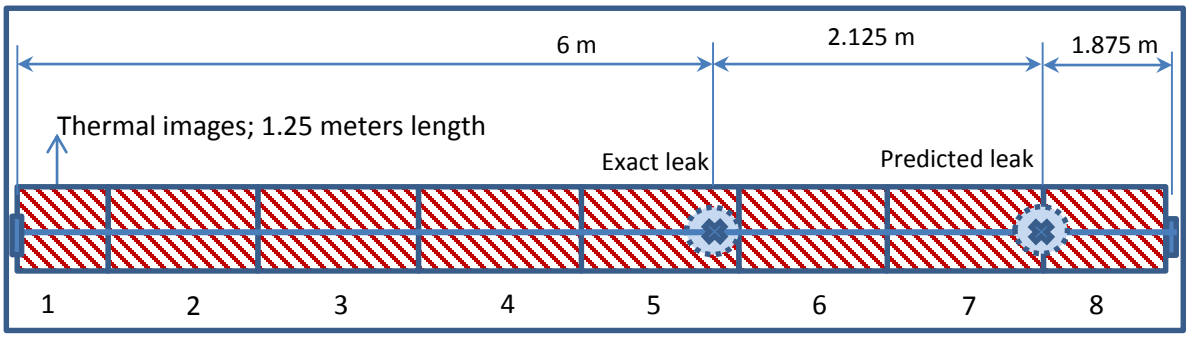

Figure 39. Predicted leak location using O.C.4 of real leak 1case

Characteristics and results of the performed experiment are summarized in Table 41

Table 22. Characteristics and results of O.C.4- real leak 1

Apparatus used	GPR: not used
	IR: Leak detector
no. of thermal images	8
ANOVA	
P-value	0.00<0.05 proceed to the pairwise comparison
pairwise	
highest contrast images	Thermal Image 7
predicted leak center	8.125 m
O.C. Accuracy	78.7%

4.1.2.5 Summary of Results

Results of the four operating conditions are summarized in Table 42.

Table 23. Real leak 1 result summary

	O.C. 1	O.C. 2	O.C. 3	O.C. 4
Characteristics	1m,2km/h	2m,5km/h	1m,5km/h	2m,2km/h
P-value	<0.05	<0.05	<0.05	<0.05
highest contrast	Thermal Image 8	Thermal Image 3	Thermal Image 3-4	Thermal Image 7
Accuracy	66.25%	90%	100%	78.7%

Unlike the simulated scenario, higher speed operating conditions (O.C 2&3) resulted in more accurate results than operating conditions with low speed (O.C 1&4). Operating condition 2 has predicted the leak location within a zero error accuracy, also operating condition 3 has predicted the leak with only 10% of error, however operating conditions 1, 4 failed have detected the leak meters away from the actual leak location that could make them inappropriate for such a scenario. Variations in operating condition accuracy are

function of changing the weathering conditions and site characteristics that will be discussed at the end of this section.

4.1.3 Real Leak Scenario 2 (Mansoora Location)

Another real leak event was introduced in collaboration with KAHRAMA located in Doha city.an unjustified decline was noted on the pavement surface that was located directly above a water pipeline as shown in Figure 40.10 meters long ductile iron pipe was scanned through the IR camera and GPR. The pipe was buried at a depth of 0.9 meters from the asphalt pavement surface, having an emissivity of $\epsilon = 0.93$ and surrounded by crushed sandstone. Thermographic images of the ground surface above the pipeline were taken with the different operating conditions. Four sets of images corresponding to each operating condition were collected. After collecting the images, the exact leak location was determined by KAHRAMAA through excavation and visual inspection. The temperature of the dry surface is varied between 24^{o} C and 29^{o} C; meanwhile, the ambient air temperature and the relative humidity were 35^{o} C and 50%, respectively. Note that GPR was used as a leak detector as well. However it will be discussed later as part of method 2 of leak detection.

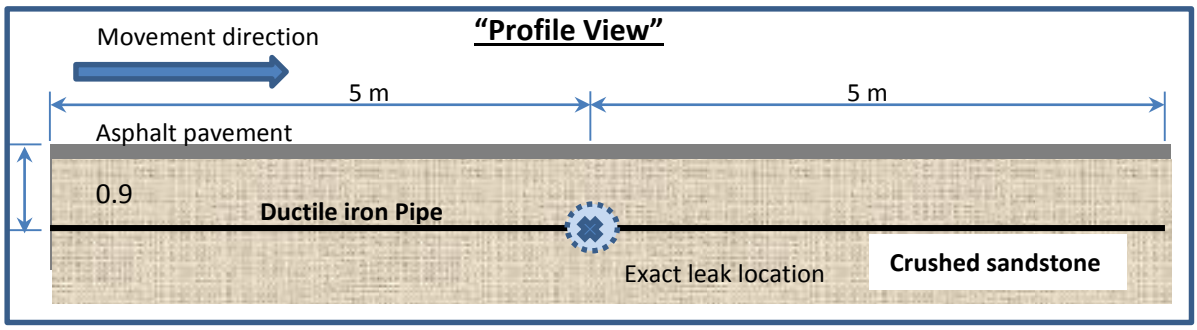

Figure 40. Real leak case 2 layout

4.1.3.1 Operating Condition 1

At a height of 1 meter and speed of 2 km/h the first trial of thermography was performed resulting in 20 thermal images distributed along the 10 meters pipe as shown in Figure 43. After collecting the IR images, their scale was adjusted to obtain a strong color contrast. Figure 41(A) shows that in the case of the real leak, the color degradation was minimal with the color being mainly dark red to pink. Contrary to that, Figure 41 (B) which represents the location of a leak in the real leak case, degradation in color was observed.

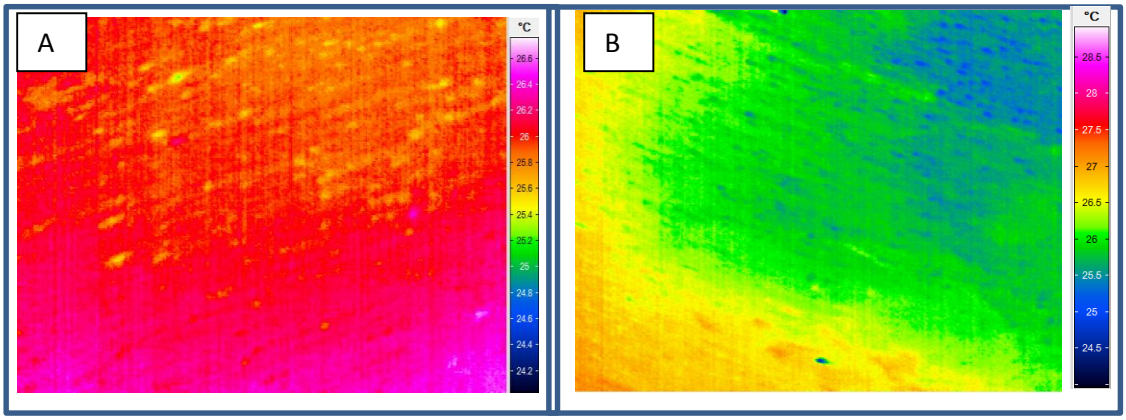

Figure 41. (A) IR image for real leak case 2 study "dry location" (B) IR image for real leak case 2 study "wet location"

4.1.3.1.1 ANOVA

Test statistics associated with the ANOVA Table 43 showed a probability value close to be zero, in other words the calculated p-value was less than the significant level of the test (p-value< α=0.05) thus enough evidence were existed to reject the null hypothesis (H_o) which claimed that there are no differences between the mean temperature of the collected thermal images.

Table 24. Test statistics of O.C1-real leak 2

	Degree of freedom	sum square	mean square	F-value	P-value
Image.ID	19	4614.5	242.870	6912.61	0.00<0.05
Residuals	9170	322.2	0.035		

4.1.3.1.2 Pairwise Comparison

Pairwise Comparison Table 44 illustrates the results where the first column encompasses the values of the mean temperatures subtraction between thermal image number 1 and all the other images and so on for the other columns. Summing up all the differences as shown in Table 45 showed that thermal image number 11 gained the highest summation among the others, accordingly, it can be claimed that the leak source was found to be at a distance of 5.25 m from the beginning of the scanned pipe, which was calculated as follows:

$$\frac{5 + 5.5}{2} = 5.25m$$

A graphical representation of the total mean temperature differences is illustrated in Figure 42, showing a stable trend for the temperature contrast along the pipeline length, except between 4m-6.5m that experience a dramatic jump.

Table 25. Pairwise comparison of O.C.1- real leak 2

Images	1	2	3	4	5	6	7	8	9	10	11	12	13	14	15	16	17	18	19	20
1	0	0.0206	0.102	0.192	0.361	0.554	0.886	1.202	1.646	2.168	2.908	1.784	1.069	0.994	0.811	0.629	0.684	0.675	0.589	0.674
2	0.026	0	0.076	0.166	0.335	0.527	0.86	1.176	1.62	2.142	2.882	1.758	1.043	0.968	0.785	0.603	0.658	0.649	0.562	0.648
3	0.102	0.076	0	0.0894	0.258	0.451	0.783	1.099	1.543	2.065	2.805	1.682	0.966	0.891	0.708	0.526	0.581	0.572	0.486	0.571
4	0.192	0.166	0.0894	0	0.168	0.361	0.694	1.01	1.453	1.976	2.715	1.592	0.877	0.802	0.619	0.437	0.492	0.4834	0.396	0.482
5	0.361	0.335	0.258	0.168	0	0.192	0.525	0.841	1.284	1.807	2.546	1.423	0.708	0.633	0.451	0.268	0.323	0.314	0.227	0.313
6	0.554	0.527	0.451	0.361	0.192	0	0.332	0.648	1.092	1.614	2.354	1.231	0.515	0.44	0.257	0.0755	0.13	0.121	0.0351	0.12
7	0.886	0.86	0.783	0.694	0.525	0.332	0	0.316	0.759	1.282	2.021	0.898	0.183	0.108	0.0746	0.256	0.201	0.21	0.297	0.211
8	1.202	1.176	1.099	1.01	0.841	0.648	0.316	0	0.443	0.965	1.705	0.582	0.133	0.208	0.39	0.573	0.518	0.526	0.613	0.527
9	1.646	1.62	1.543	1.453	1.284	1.092	0.759	0.443	0	0.522	1.261	0.138	0.576	0.651	0.834	1.016	0.961	0.97	1.057	0.971
10	2.168	2.142	2.065	1.976	1.807	1.614	1.282	0.965	0.522	0	0.739	0.383	1.098	1.173	1.356	1.538	1.483	1.492	1.579	1.493
11	2.908	2.882	2.805	2.715	2.546	2.354	2.021	1.705	1.261	0.739	0	1.123	1.838	1.913	2.096	2.278	2.223	2.232	2.319	2.233
12	1.784	1.758	1.682	1.592	1.423	1.231	0.898	0.582	0.138	0.383	1.123	0	0.715	0.79	0.973	1.155	1.1	1.109	1.195	1.11
13	1.069	1.043	0.966	0.877	0.708	0.515	0.183	0.133	0.576	1.098	1.838	0.715	0	0.075	0.257	0.439	0.385	0.393	0.48	0.394
14	0.994	0.968	0.891	0.802	0.633	0.44	0.108	0.208	0.651	1.173	1.913	0.79	0.075	0	0.182	0.364	0.309	0.318	0.405	0.319
15	0.811	0.785	0.708	0.619	0.451	0.257	0.0746	0.39	0.834	1.356	2.096	0.973	0.257	0.182	0	0.182	0.127	0.136	0.222	0.136
16	0.629	0.603	0.526	0.437	0.268	0.0755	0.256	0.573	1.016	1.538	2.278	1.155	0.439	0.364	0.182	0	0.0548	0.0461	0.0407	0.0453
17	0.684	0.658	0.581	0.492	0.323	0.13	0.201	0.518	0.961	1.483	2.223	1.1	0.385	0.309	0.127	0.0548	0	0.00868	0.0953	0.00951
18	0.675	0.649	0.572	0.4834	0.314	0.121	0.21	0.526	0.97	1.492	2.232	1.109	0.393	0.318	0.136	0.0461	0.00868	0	0.0866	0.00083
19	0.589	0.562	0.486	0.396	0.227	0.0351	0.297	0.613	1.057	1.579	2.319	1.195	0.48	0.405	0.222	0.0407	0.0953	0.0866	0	0.0858
20	0.674	0.648	0.571	0.482	0.313	0.12	0.211	0.527	0.971	1.493	2.233	1.11	0.394	0.319	0.136	0.0453	0.00951	0.00083	0.0858	0

Table 26. Scoring table of O.C.1- real leak 2

Image Boundaries(m)		Images	Total score
0	0.5	1	17.954
0.5	1	2	17.4786
1	1.5	3	16.2544
1.5	2	4	15.0048
2	2.5	5	12.977
2.5	3	6	11.0496
3	3.5	7	10.8966
3.5	4	8	13.475
4	4.5	9	18.797
4.5	5	10	26.875
5	5.5	11	40.191
5.5	6	12	20.741
6	6.5	13	12.144
6.5	7	14	11.543
7	7.5	15	10.5966
7.5	8	16	10.5264
8	8.5	17	10.34329
8.5	9	18	10.34261
9	9.5	19	10.7705
9.5	10	20	10.34344

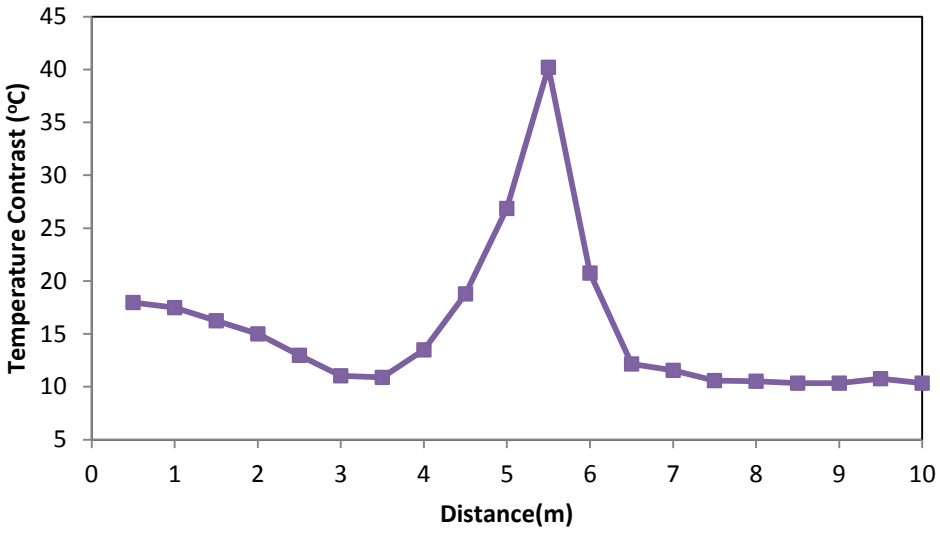

Figure 42. Distance-Temperature contrast relation of O.C.1- real leak 2

The accuracy of the processes was checked by comparing the predicted leak location with the actual leak location. The actual leak location was at the center of the pipe at 5 m. The predicted leak was at thermal 11 which represent a distance from 5 m to 5.5 m as shown in Figure 43. Consequently, the center of the predicted leak is 5.25 m away from the pipe beginning, so the accuracy of the proposed operating combination is given by:

$$\text{Approach accuracy} = 1 - \frac{leak(exact) - (center\ of\ the\ predicted\ leak)}{pipe\ length} = 1 - \left|\frac{5-5.25}{10}\right| = 97.5\%$$

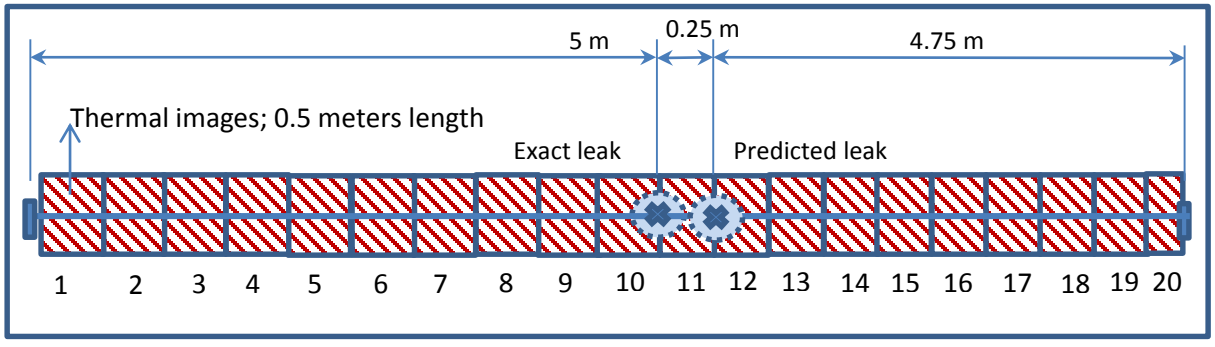

Figure 43. Predicted leak location using O.C.1 of real leak 2

Characteristics and results of the performed experiment are summarized in Table 46.

Table 27. Characteristics and results of O.C.1- real leak 2

Apparatus used	**GPR: not used**
	IR: Leak detector
no. of thermal images	20
ANOVA	
P-value	0.00<0.05 proceed to the pairwise comparison
pairwise	
highest contrast images	Thermal Image11
predicted leak center	5.25 m
O.C. Accuracy	97.5%

4.1.3.2 Operating Condition 2

At a height of 2 meters and speed of 5 km/h the first trial of thermography was performed resulting in 7 thermal images distributed along the 10 meters pipe as shown in Figure 45.

4.1.3.2.1 ANOVA

Test statistics associated with the ANOVA Table 47 showed a probability value close to be zero, in other words the calculated p-value was less than the significant level of the test (p-value< α=0.05) thus enough evidence were existed to reject the null hypothesis (H_o) which claimed that there are no differences between the mean temperature of the collected thermal images.

Table 28. Test statistics of O.C.2-real leak 2

	Degree of freedom	sum square	mean square	F-value	P-value
Image.ID	6	396734	66122.3	696319.39	0<0.05
Residuals	652449	61956	0.1		

4.1.3.2.2 Pairwise Comparison

Pairwise Comparison Table 48 illustrates the results where the first column encompasses the values of the mean temperatures subtraction between thermal image number 1 and all the other images and so on for the other columns

Table 48. Pairwise comparison of O.C.2- real leak 2

Images	1	2	3	4	5	6	7
1	0	0.78493	2.11833	0.43334	0.00107	0.16957	0.31386
2	0.78493	0	1.33341	0.35159	0.786	0.9545	1.09879
3	2.11833	1.33341	0	1.68499	2.1194	2.28791	2.4322
4	0.43334	0.35159	1.68499	0	0.43441	0.60291	0.7472
5	0.00107	0.786	2.1194	0.43441	0	0.1685	0.31279
6	0.16957	0.9545	2.28791	0.60291	0.1685	0	0.14429
7	0.31386	1.09879	2.4322	0.7472	0.31279	0.14429	0

Summing up all the differences as shown in Table 49 showed that thermal image number 3 gained the highest summation among the others, accordingly, it can be claimed that the leak source was found to be at a distance of 3.575 m from the beginning of the scanned pipe, which was calculated as follows:

$$\frac{2.86 + 4.29}{2} = 3.575m$$

A graphical representation of the total mean temperature differences is illustrated in Figure 44, showing a stable trend for the temperature contrast along the pipeline length, except the increase associated with image 3.

Table 29. Scoring table of O.C.2- real leak 2

Image Boundaries(m)		Images	Total score
0	1.43	1	3.8211
1.43	2.86	2	4.52429
2.86	4.29	3	9.85791
4.29	5.72	4	3.8211
5.72	7.15	5	3.8211
7.15	8.58	6	4.15811
8.58	10	7	4.73527

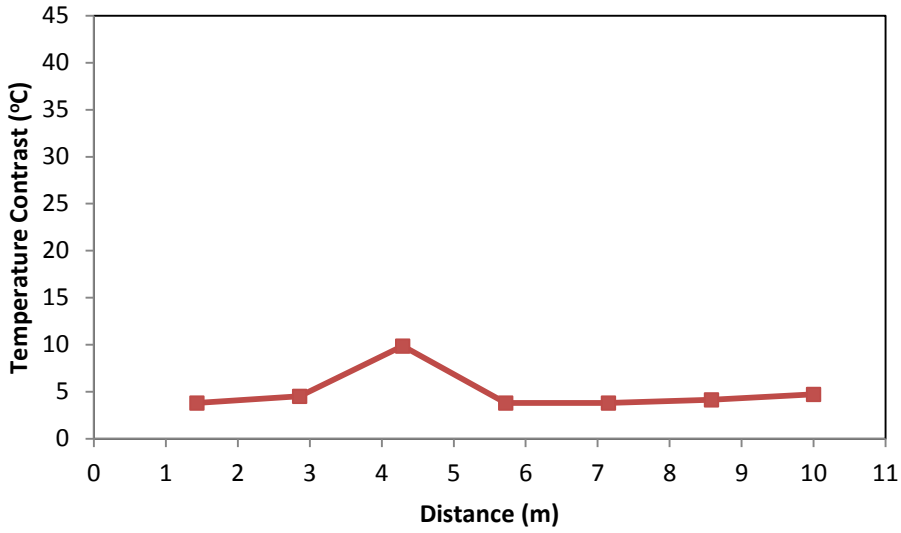

Figure 44. Distance-Temperature contrast relation of O.C.2- real leak 2

The accuracy of the processes was checked by comparing the predicted leak location with the actual leak location. The actual leak location was at the center of the pipe at 5 m. The predicted leak was at thermal 7 which represent a distance from 2.86 m to 4.29 m as shown in Figure 45. Consequently, the center of the predicted leak is 3.575 m away from the pipe beginning, so the accuracy of the proposed operating combination is given by:

$$\text{Approach accuracy} = 1 - \frac{leak(exact) - (center\ of\ the\ predicted\ leak)}{pipe\ length} = 1 - \frac{5 - 3.575}{10} = 85.75\%$$

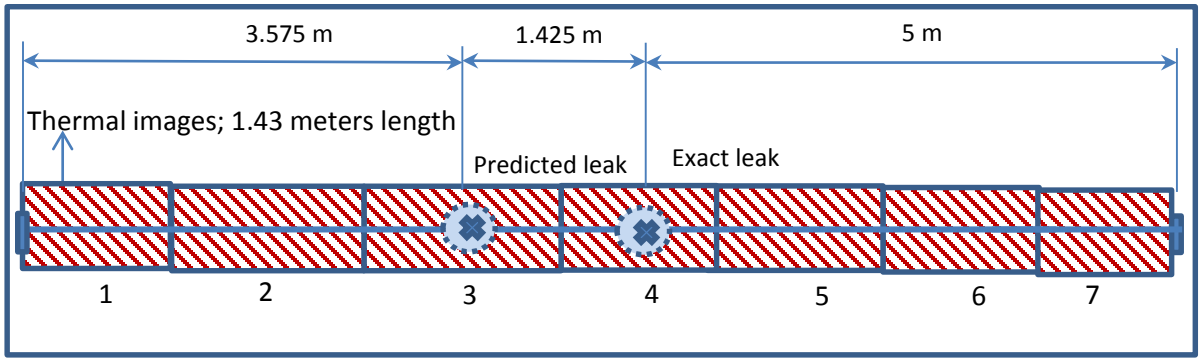

Figure 45. Predicted leak location using O.C.2 of real leak 2

Characteristics and results of the performed experiment are summarized in Table 50

Table 50. Characteristics and results of O.C.2- real leak 2

Apparatus used	**GPR: not used**
	IR: Leak detector
no. of thermal images	7
ANOVA	
P-value	0.00<0.05 proceed to the pairwise comparison
pairwise	
highest contrast	Thermal Image 3
predicted leak center	3.575 m
O.C. Accuracy	85.75%

4.1.3.3 Operating Condition 3

At a height of 1 meter and speed of 5 km/h the first trial of thermography was performed resulting in 7 thermal images distributed along the 10 meters pipe as shown in Figure 47.

4.1.3.3.1 ANOVA

Test statistics associated with the ANOVA Table 51 showed a probability value close to be zero, in other words the calculated p-value was less than the significant level of the test (p-value< α=0.05) thus enough evidence were existed to reject the null hypothesis (H_o)

which claimed that there are no differences between the mean temperature of the collected thermal images.

Table 51. Test statistics of O.C.3-real leak 2

	Degree of freedom	sum square	mean square	F-value	P-value
Image.ID	6	347075	57845.8	603163.74	0<0.05
Residuals	774137	74243	0.1		

4.1.3.3.2 Pairwise Comparison

Pairwise comparison Table 52 illustrates the results where the first column encompasses the values of the mean temperatures subtraction between thermal image number 1 and all the other images and so on for the other columns.

Table 30. Pairwise comparison of O.C.3- real leak 2

Images	1	2	3	4	5	6	7
1	0	1.09543	1.82949	0.35288	0.04727	0.02397	0.02159
2	1.09543	0	0.73405	0.74256	1.04816	1.1194	1.11702
3	1.82949	0.73405	0	1.47661	1.78222	1.85345	1.85108
4	0.35288	0.74256	1.47661	0	0.30561	0.37685	0.37447
5	0.04727	1.04816	1.78222	0.30561	0	0.07124	0.06886
6	0.02397	1.1194	1.85345	0.37685	0.07124	0	0.00238
7	0.02159	1.11702	1.85108	0.37447	0.06886	0.00238	0

Summing up all the differences as shown in Table 53 showed that thermal image number 3 gained the highest summation among the others, accordingly, it can be claimed that the leak source was found to be at a distance of 3.575 m from the beginning of the scanned pipe, which was calculated as follows:

$$\frac{2.86 + 4.29}{2} = 3.575m$$

A graphical representation of the total mean temperature differences is illustrated in Figure 46, showing a stable trend for the temperature contrast along the pipeline length, except the increase associated with image 3.

Table 31. Scoring table of O.C.3- real leak 2

Image Boundaries(m)		Images	Total score
0	1.43	1	3.37063
1.43	2.86	2	4.76119
2.86	4.29	3	7.69741
4.29	5.72	4	3.2761
5.72	7.15	5	3.27609
7.15	8.58	6	3.42332
8.58	10	7	3.41381

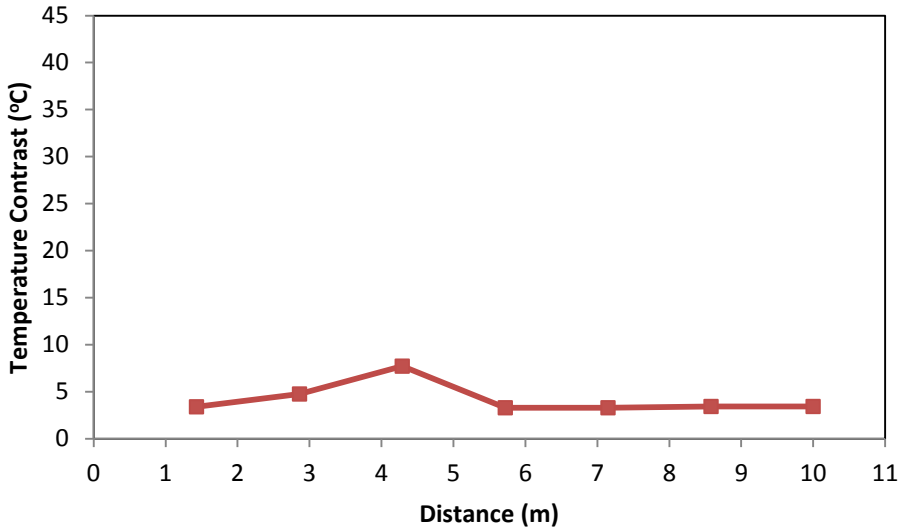

Figure 46. Distance-Temperature contrast relation of O.C.3- real leak 2

The accuracy of the processes was checked by comparing the predicted leak location with the actual leak location. The actual leak location was at the center of the pipe at 5 m. The predicted leak was at thermal 7 which represent a distance from 2.86 m to 4.29 m as shown

in Figure 47. Consequently, the center of the predicted leak is 3.575 m away from the pipe beginning, so the accuracy of the proposed operating combination is given by:

$$\text{Approach accuracy} = 1 - \frac{leak(exact) - (center\ of\ the\ predicted\ leak)}{pipe\ length} = 1 - \frac{5 - 3.575}{10} = 85.75\%$$

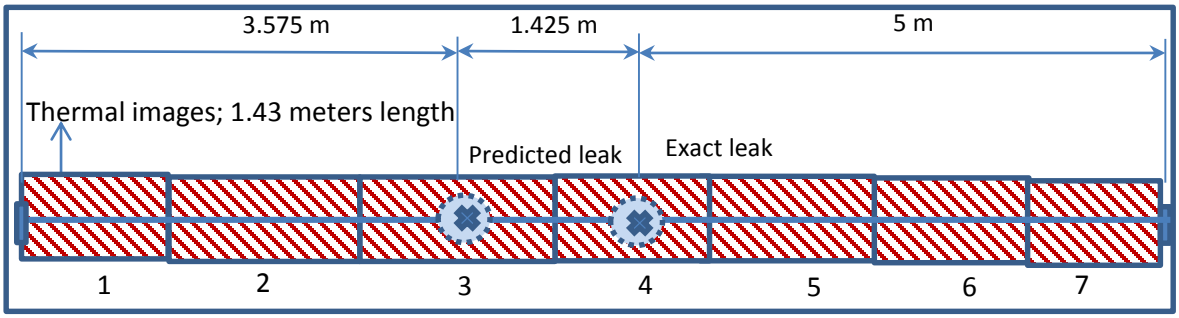

Figure 47. Predicted leak location using O.C.3 of real leak 2

Characteristics and results of the performed experiment are summarized in Table 54.

Table 54. Characteristics and results of O.C.3- real leak 2

Apparatus used	**GPR: not used**
	IR: Leak detector
no. of thermal images	7
ANOVA	
P-value	0.00<0.05 proceed to the pairwise comparison
pairwise	
highest contrast	Thermal Image 3
predicted leak center	3.575 m
O.C. Accuracy	85.75%

4.1.3.4 Operating Condition 4

At a height of 2 meters and speed of 2 km/h the first trial of thermography was performed resulting in 13 thermal images distributed along the 10 meters pipe as shown in Figure 49.

4.1.3.4.1 ANOVA

Test statistics associated with the ANOVA Table 55 showed a probability value close to be zero, in other words the calculated p-value was less than the significant level of the test (p-value< α=0.05) thus enough evidence were existed to reject the null hypothesis (H_o) which claimed that there are no differences between the mean temperature of the collected thermal images.

Table 55. Test statistics of O.C.4-real leak 2

	Degree of freedom	sum square	mean square	F-value	P-value
Image.ID	12	535276	44606.3	347491.88	0<0.05
Residuals	1142843	146703	0.1		

4.1.3.4.2 Pairwise Comparison

Pairwise Comparison Table 56 illustrates the results where the first column encompasses the values of the mean temperatures subtraction between thermal image number 1 and all the other images and so on for the other columns.

Table 32. Pairwise comparison of O.C.4- real leak 2

Images	1	2	3	4	5	6	7	8	9	10	11	12	13
1	0	0.18778	0.62293	1.31422	2.34828	1.74847	0.73256	0.46383	0.3378	0.28811	0.21531	0.2096	0.43515
2	0.18778	0	0.43515	1.12643	2.16049	1.56069	0.54478	0.27604	0.15002	0.10032	0.02753	0.02182	0.0563
3	0.62293	0.43515	0	0.69129	1.72535	1.12554	0.10963	0.1591	0.28513	0.33482	0.40762	0.41333	0.49144
4	1.31422	1.12643	0.69129	0	1.03406	0.43425	0.58165	0.85039	0.97641	1.02611	1.0989	1.10462	1.18273
5	2.34828	2.16049	1.72535	1.03406	0	0.59981	1.61571	1.88445	2.01047	2.06017	2.13296	2.13868	2.21679
6	1.74847	1.56069	1.12554	0.43425	0.59981	0	1.01591	1.28464	1.41067	1.46036	1.53316	1.53887	1.61698
7	0.73256	0.54478	0.10963	0.58165	1.61571	1.01591	0	0.26874	0.39476	0.44445	0.51725	0.52296	0.60108
8	0.46383	0.27604	0.1591	0.85039	1.88445	1.28464	0.26874	0	0.12602	0.17572	0.24851	0.25423	0.33234
9	0.3378	0.15002	0.28513	0.97641	2.01047	1.41067	0.39476	0.12602	0	0.0497	0.12249	0.1282	0.20632
10	0.28811	0.10032	0.33482	1.02611	2.06017	1.46036	0.44445	0.17572	0.0497	0	0.07279	0.07851	0.15662
11	0.21531	0.02753	0.40762	1.0989	2.13296	1.53316	0.51725	0.24851	0.12249	0.07279	0	0.00571	0.08383
12	0.2096	0.02182	0.41333	1.10462	2.13868	1.53887	0.52296	0.25423	0.1282	0.07851	0.00571	0	0.07811
13	0.43515	0.0563	0.49144	1.18273	2.21679	1.61698	0.60108	0.33234	0.20632	0.15662	0.08383	0.07811	0

Summing up all the differences as shown in Table 57 showed that thermal image number 5 gained the highest summation among the others, accordingly, it can be claimed that the leak source was found to be at a distance of 3.461 m from the beginning of the scanned pipe, which was calculated as follows:

$$\frac{3.076 + 3.845}{2} = 3.461m$$

A graphical representation of the total mean temperature differences is illustrated in Figure 48, showing a stable trend for the temperature contrast along the pipeline length, except the increase associated with image 5.

Table 33. Scoring table of O.C.4- real leak 2

Image Boundaries(m)		Images	Total score
0	0.769	1	8.90404
0.769	1.538	2	6.64735
1.538	2.307	3	6.80133
2.307	3.076	4	11.42106
3.076	3.845	5	21.92722
3.845	4.614	6	15.32935
4.614	5.383	7	7.34948
5.383	6.152	8	6.32401
6.152	6.921	9	6.19799
6.921	7.69	10	6.24768
7.69	8.459	11	6.46606
8.459	9.228	12	6.49464
9.228	10	13	7.45769

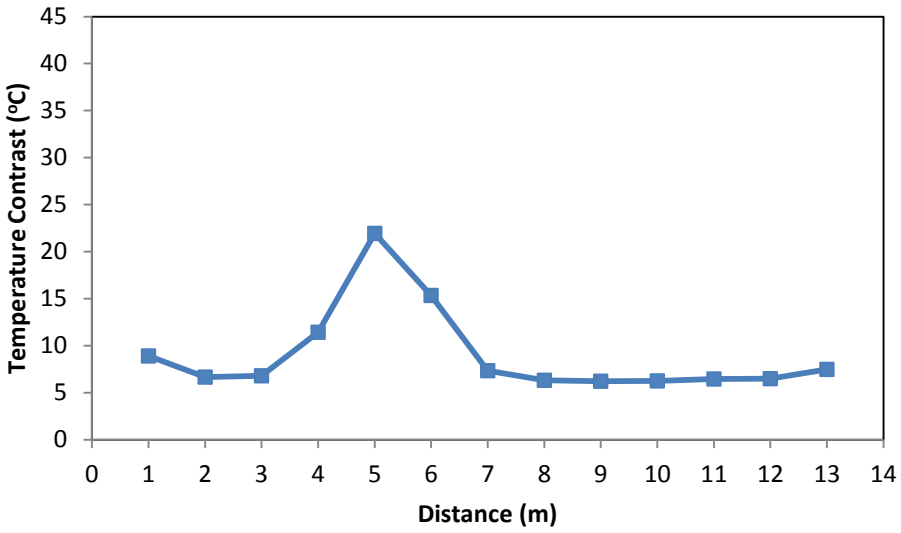

Figure 48. Characteristics and results of O.C.4- real leak 2

The accuracy of the processes was checked by comparing the predicted leak location with the actual leak location. The actual leak location was at the center of the pipe at 5 m. The predicted leak was at thermal 7 which represent a distance from 3.076 m to 3.845 m as shown in Figure 49. Consequently, the center of the predicted leak is 3.461 m away from the pipe beginning, so the accuracy of the proposed operating combination is given by:

$$\text{Approach accuracy} = 1 - \frac{leak(exact) - (center\ of\ the\ predicted\ leak)}{pipe\ length} = 1 - \frac{5 - 3.461}{10} = 84.6\%$$

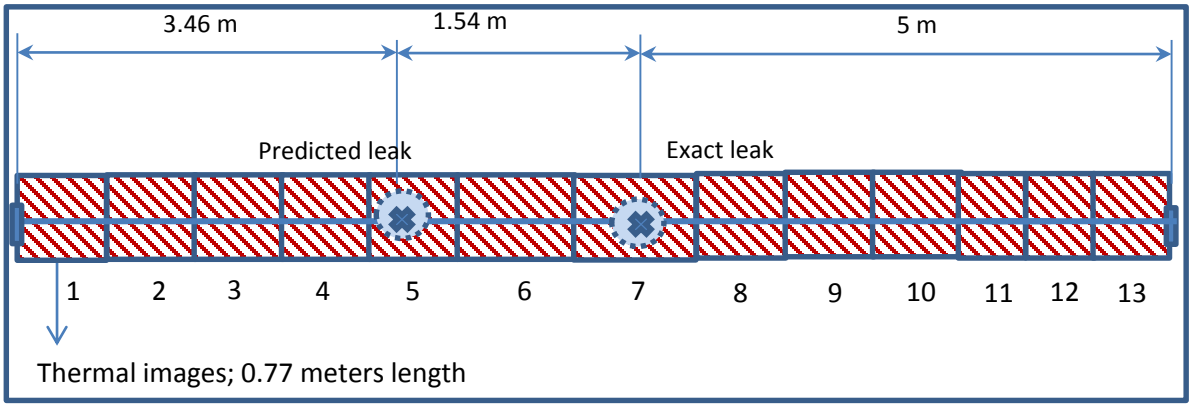

Figure 49. Predicted leak location using O.C.4 of real leak 2

Characteristics and results of the performed experiment are summarized in Table 58.

Table 58. Characteristics and results of O.C.4- real leak 2

Apparatus used	**GPR: not used**
	IR: Leak detector
no. of thermal images	13
ANOVA	
P-value	0.00<0.05 proceed to the pairwise comparison
pairwise	
highest contrast	Thermal Image 5
predicted leak center	3.46 m
O.C. accuracy	84.6%

4.1.3.5 Summary of Results

Results of the four operating conditions are summarized in Table 59.

Table 59. Real leak 2 result summary

	O.C. 1	**O.C. 2**	**O.C. 3**	**O.C. 4**
Characteristics	1m,2km/h	2m,5km/h	1m,5km/h	2m,2km/h
P-value	<0.05	<0.05	<0.05	<0.05
highest contrast	Thermal Image 11	Thermal Image 3	Thermal Image 3	Thermal Image 5
Accuracy	97.5%	85.75%	85.75%	84.6%

Since the weathering conditions of Al mansoora real leak location were not as severe as mesaeed leak location(because of spring season), it can be noticed that all of the operating conditions have resulted in relatively precise outcomes in which their accuracies were above 84%, consequently ,having a high emissive surface (such as bricks or asphalt) and appropriate weathering conditions (moderate ground and ambient air temperature and humidity) will result in acceptable outcomes regardless the operating conditions.

4.1.4 Method 1 Results Summary

As mentioned earlier four sets of scans were performed along the pipeline (one set of images for each operating condition). The resolution of the used camera is 384 x 288 pixels, which means that each image will be translated to 110,592 temperature data points. Temperature values from the collected images were then statistically analyzed using ANOVA. In the case of simulated and real leak the resulted F-values were very high and the associated p-values were less than the specified significance level ($\alpha = 0.05$). This gives enough evidence to reject the null hypothesis (H_o) under all operating conditions, which means that a temperature contrast does exist among the collected data sets.

Consequently pairwise comparison between the mean temperatures of each image within the same set was performed using a Tukey procedure in Minitab, and the differences were summed up for each image. The same process was repeated for all the operating conditions in the simulated and real leak cases. In the case of the simulated leak; operating condition (1) (camera height 1 m and camera speed 2 km/h) had the best prediction results followed by operating condition (4) (camera height 2 m and camera speed 2 km/h). As for the first real leak(mesaeed location) the best prediction results were obtained at operating conditions (2) and (3) (condition (2): 1m height and camera speed 5 km/h, and condition (3): 2 m height and camera speed 5 km/h) ,however operating condition (1) was the most appropriate in detecting the second real leak (Mansoora).

The best prediction results were determined according to two factors: firstly the ability to predict the existence of a leak and secondly the ability to locate the leak. For the first factor, in all cases (simulated and real leaks) and under all running conditions the ANOVA

analysis gave enough evidence to reject the null hypothesis (p-value less than $\alpha = 0.05$) which indicated the existence of a leak. For the prediction of the location of the leak, from the pairwise comparison results it was found that several factors had an impact on the enhancement of the thermal contrast and therefore, affected the prediction of the location of the leak. The factors that were taken into consideration in this study were categorized into three main categories: characteristics of the studied surface (emissivity), characteristics of the surrounding environment (ambient temperature and relative humidity), and the operating conditions of the IR camera (speed and height from the surface).

4.1.4.1 Impact of the Characteristics of the Studied Surface (Emissivity)

It was found that the captured thermal contrast depends on the characteristics of the surface emitting the energy. The emissivity of the surface is very important as it defines how much thermal energy an object of interest can radiate; rougher and darker surfaces have the highest emissivity [57]. In the case of the simulated leak the surface was a low emissive surface (clayey soil ($\epsilon = 0.39$)) while in the real leak cases (mesaeed and mansoora) the surface was highly emissive (bricks and asphalt respectively ($\epsilon = 0.93$)).

Operation condition (1) and (4) have successfully detected the exact location of the simulated leak scenario where lower IR camera speed was required for the low emissive surface for the camera to acquire the thermal contrast at the simulated leak case. Consequently, at higher speed the IR camera would fail in capturing appropriate thermal contrast that represents the exact leak location. At the highly emissive (bricks) surface leak location (Mesaeed) camera operating conditions with lower speed failed to capture

appropriate thermal contrast where the predicted leak location of operation condition (1) and (4) at two different camera heights was shifted almost the same distance away from the real leak location in the direction of movement .This could be because the real leak case was performed in the summer at high ambient temperature (42 ^{o}C) and high relative humidity (75%).Although the second real leak location (Mansoora) was a high emissive surface, the desired outcomes were resulted at high and low speed of the IR camera as well , this could be due to conducting the test at the spring where anomaly sources(high ground and ambient air temperature and severe humidity) were less than summer, in other words weathering condition of Al Mansoora leak location were friendly to the IR device in which extra tactics to reduce eccentricity were not necessary .

4.1.4.2 Impact of the Characteristics of the Surrounding Environment (Ambient Temperature and Relative Humidity)

It is anticipated that high relative humidity and high ambient temperature would also create thermal contrasts in the IR thermography process Thus; the accuracy of the readings in IR thermography would be affected [57]. Therefore, in summer days with high humidity, lower IR detection ranges would be anticipated than for conditions of spring at low humidity season since humidity will act as a shield that repels the radiated energy from being captured by the IR camera sensors [58]. It was found in this study that under high ambient temperature and relative humidity conditions the higher speed of the IR camera would reduce the impact of such side factors (noise) on the thermal contrast and therefore, would give better results in predicting the location of the leak, however in moderate weathering conditions and highly emissive surface such as the second real leak case the IR

camera will not be affected by the side factors and the leak can be detected at any of the camera operating conditions (any height , any speed) with varying accuracy.

4.1.4.3 Impact of the Operating Conditions of the IR Camera (Speed and Height from the Surface)

It was found that in the simulated leak case (low ambient temperature, low relative humidity and low emissive surface) the lower speed of the camera gave better results in identifying the location of the leak than the higher camera speed ,whereas, in the real leak case (high ambient temperature, high relative humidity and highly emissive surface), better results were obtained when the speed of the camera was higher, however in the second real leak case (moderate ambient temperature, moderate relative humidity and highly emissive surface) at any IR camera speed and height the results still accurate, since the external factors are not too severe to affect the IR camera capturing sensors. Whereas, in the simulated leak scenario (low ambient temperature, low relative humidity, and low emissive surface) the lower speed of the camera gave better results in identifying the location of the leak than the higher camera speed.

Furthermore, in the case of the simulated leak the height of camera had a direct impact on the enhancement of the thermal contrast compared to the real leak case. It was found that at a lower height of the camera better leak predictions were obtained. However, the height of the camera had minimal impact on enhancing the captured thermal contrasts in the real leak case. The height of the camera from the surface would affect the field of view (FOV) of the camera. The FOV of the used camera is 1.0/25 mm (30 x 23)^{o} at (384 x 288) this

translates to a field of view of 0.34m x 0.45m at a 1m distance with a 1.2mm pixel, and 0.68m x 0.90m at a distance of 2m with a 2.4mm pixel. Therefore, at lower heights less area will be covered per frame which means more homogenous temperature distribution per frame. Consequently, the contrast between the different frames will be higher. The error of leak location prediction was calculated for both case studies by comparing the difference of distances between the beginning and the end of the actual leak location with the beginning and the end of the predicted leak location. Table 5 summarizes the error of prediction in the simulated and real leak cases under the four different operating conditions.

4.1.4.4 IRT Limitations

Similar to the other leak detection techniques, IR thermography encounters some obstacles in which its application becomes limited. Environment conditions appear to be one of these limitations, since it was found that the acquired thermal data is affected by ambient humidity and temperature. Moreover, thermographic leak investigations are associated with the temperature contrasts along the tested ground surface above the pipeline, which might be an issue if the water did not reach the surface where a temperature contrast will not be captured.

4.2 Method 2

In method two the GPR was the only leak detector device used. MALA GPR device was used to collect subsurface profiles along the pipe length using an electromagnetic wave frequency of 500 MHz.

4.2.1 Pipe Locating

To accurately detect the leak location, precise pipeline profile should be performed. A process similar to the one utilized in section 6.1.1 was used where the pipe was located through a set of runs perpendicular to the suspected location of the pipe. Hyperbolic shapes would indicate the location of the pipe at the predefined depth of 0.8 m Figure 50. Magnitude and phase analysis were focused at the pipe depth as will be discussed in the next section.

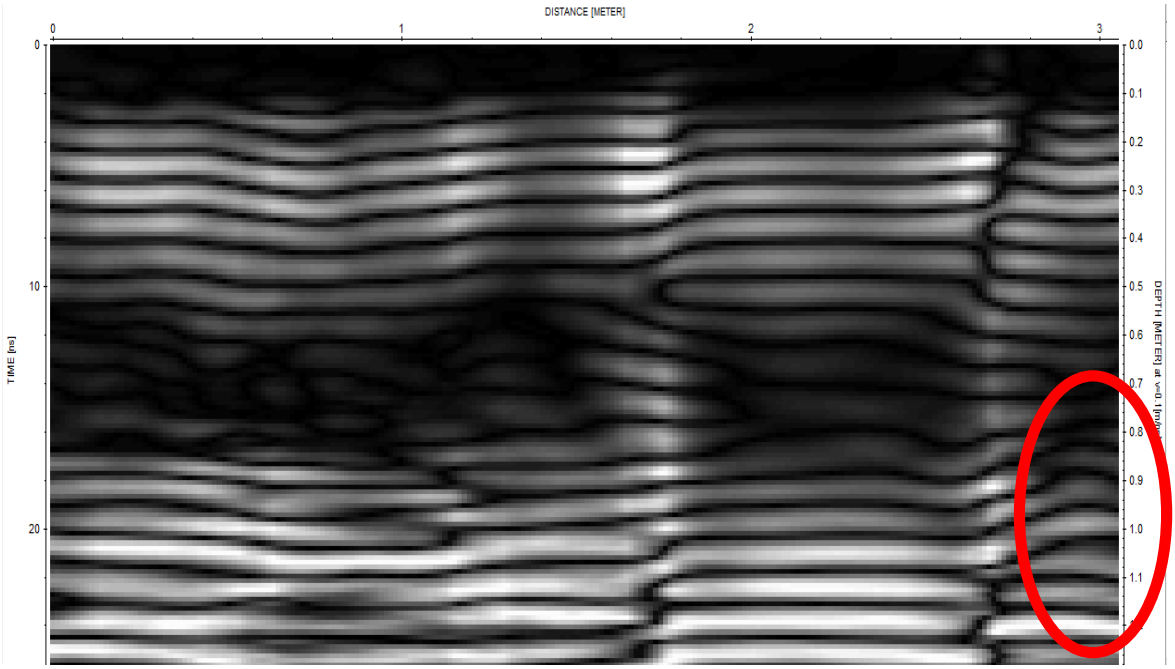

Figure 50. Radargram of the pipe location

4.2.2 Radargram Analysis

A refinement process has been carried out which is based on the fk-migration function in Reflex2DQuick software discussed earlier. Figure 51 shows the radargram before and after refinement. Since the important features that need to be tracked from the acquired

radargram data were all related to the leak event, fk migration was adjusted based on the propagation velocity of the electromagnetic waves passing through the wet sand with a dielectric constant of ε = 20-30. Consequently, the velocity of migration was calculated as follows:

$$V = \frac{c = \frac{0.3m}{ns}}{\sqrt{\varepsilon} = \sqrt{\frac{20+30}{2}}} = 0.06\frac{m}{ns}$$

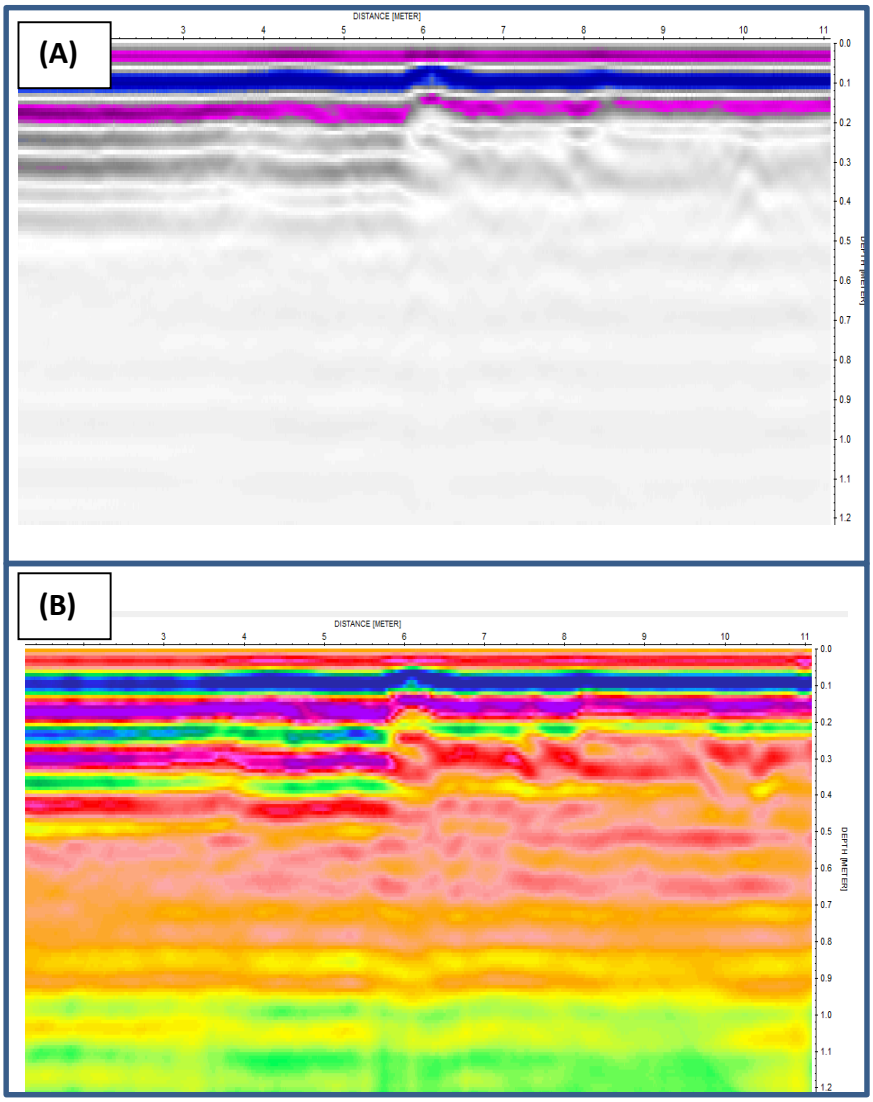

Figure 51 (A): Raw radargram , (B): Refined radagram

A radargram image for the dry location Figure 52 collected after pipe repairing shows a consistent and smooth profile surrounding the pipe with almost no anomalies detected. Distortions associated with the repairing and rehabilitation of the leaked pipe can be clearly highlighted due to excavation and soil refill processes.

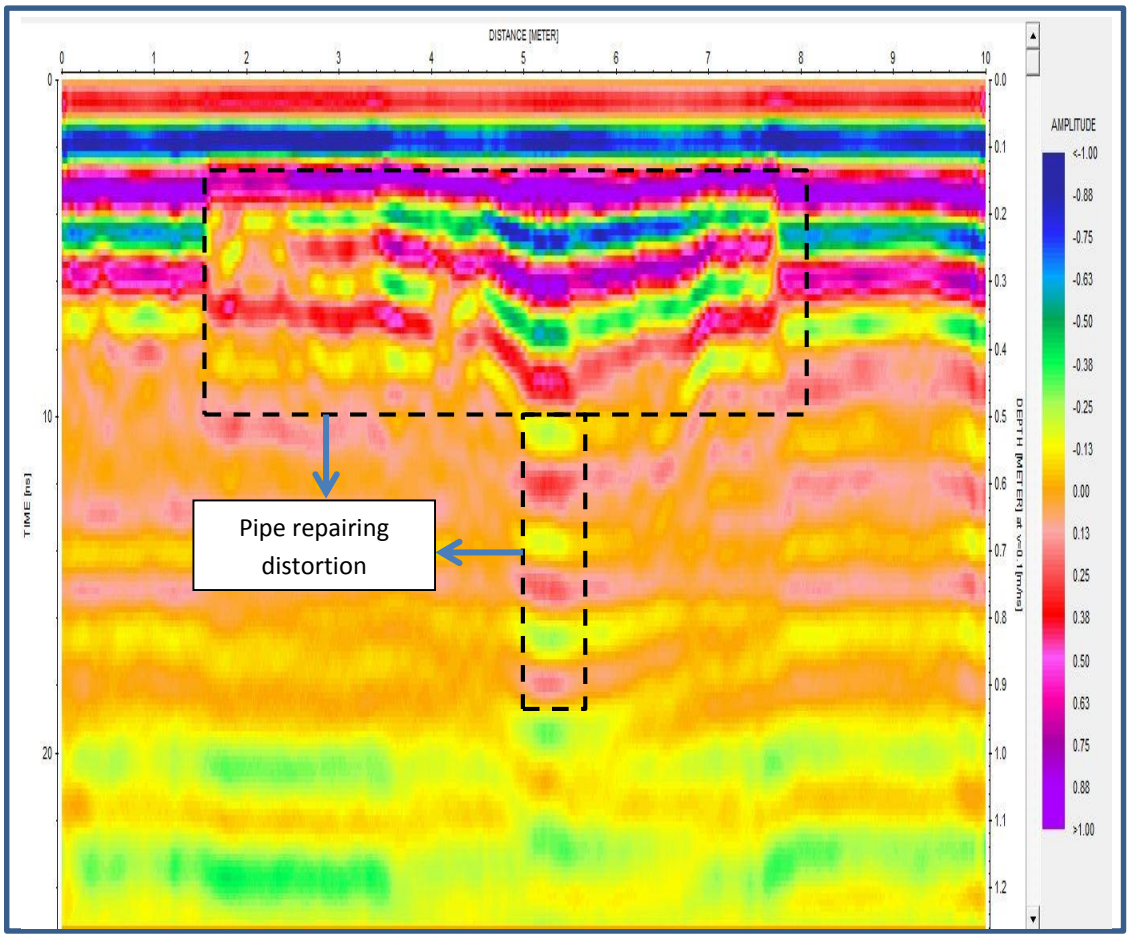

Figure 52. Refined radargram of the dry case

In the leak case (Before rehabilitation), it can be noticed that the radargram included two distinct zones Figure 53; Zone 1 from 0-5.8 m and Zone 2 from 5.8 m – 10 m along the pipe length. Zone 1 characterizes the dry situation, where the reflected EM waves drew gentle subsurface layout (free of discontinuities or disturbances). At the length of 5.8 m until the end of the pipe an abnormal anomaly appeared 10 cm below the ground surface. The layers disorder continues to a depth of 35 cm. Another disturbance was noted at the pipe expected location, where a trend discontinuity has been monitored along the pipe length between 5.8 m - 6.4 m and 7.8 m - 10m represented by the color degradation change from yellow (indicates negative reflection) to light brown (indicates positive reflection).

All of the observed anomalies in zone 2 conclude that the subsurface condition had been changed from that in the dry radargram, which can be attributed to a leak event.

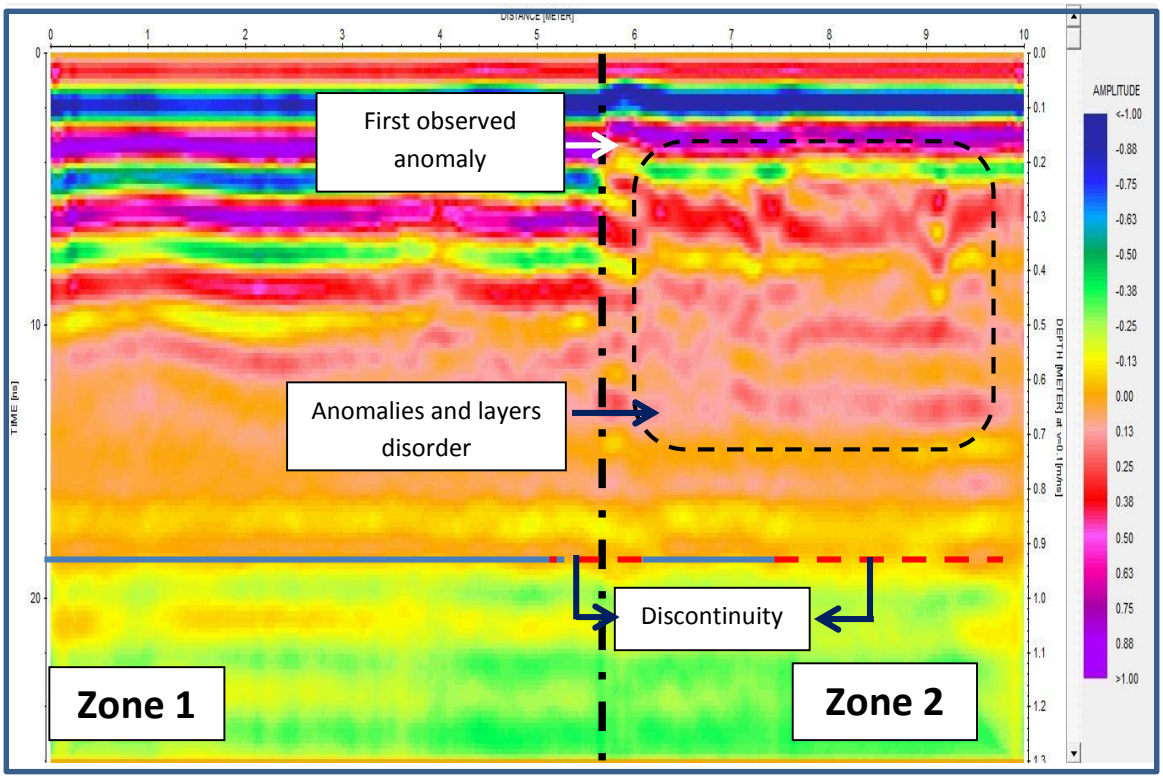

Figure 53. Refined radaragram of the wet case

Results from the use of IR technology for the same case study were superimposed on the wet radargram Figure 54. A consistency of outcomes can be observed where the anomaly location in the radargram (10 cm below ground surface between 5.8 m – 6 m) meets the location associated with the highest temperature contrast in the IR analysis. Further studies are still required to investigate the applicability of method two for leak detection under controlled conditions.

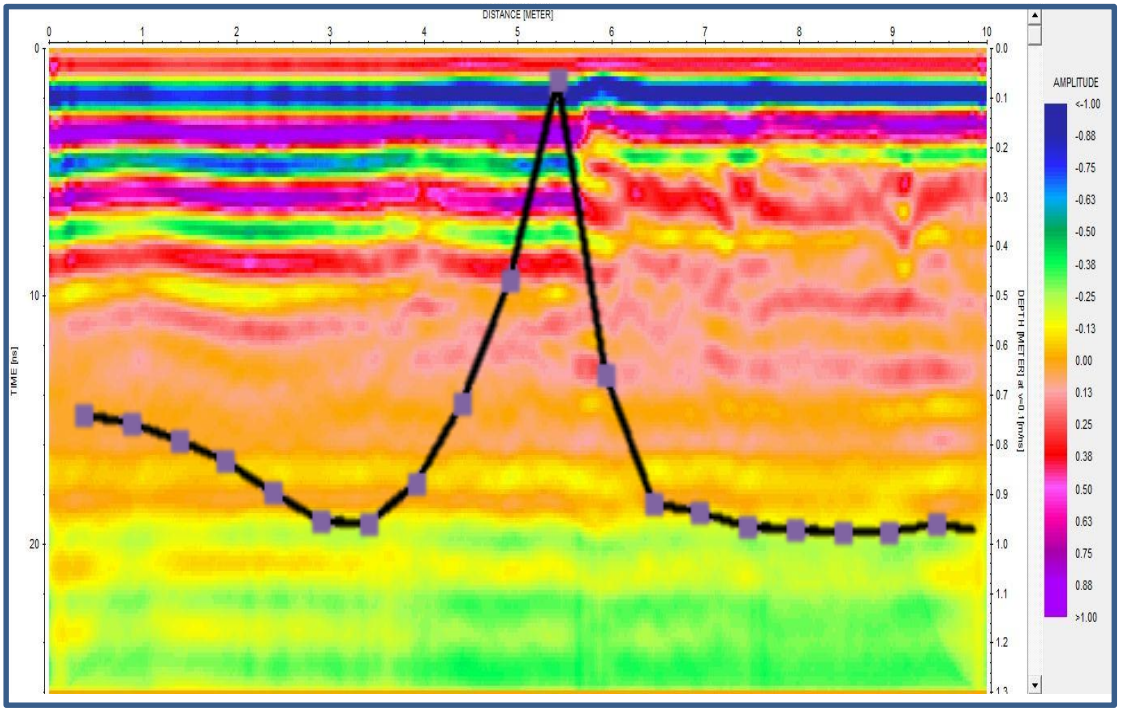

Figure 54. IR Results superimposed on the refined wet radargram

Chapter 5: Conclusions

In this study, two noninvasive and nondestructive methodologies for detecting leaks in water networks were proposed and tested. The first method combines the use of Ground Penetrating Radar (GPR) for accurate determination of pipe location, followed by infrared (IR) thermographic imaging for determining the leak location. The second method uses GPR alone to predict the existence and location of a leak in water networks.

In method one the collected IR thermographic images were statistically analyzed using analysis of variance (ANOVA) and pairwise comparison methods. A simulated and real life leaks were studied. Several factors were found to affect the accuracy of the proposed methodology in predicting the leak location, namely, the characteristics of the studied surface (i.e. emissivity), the characteristics of the surrounding environment (i.e. ambient temperature and relative humidity), and the operating conditions of the IR camera (i.e. speed and height of the camera). In the case of low emissive surfaces (ε=0.39 for clay), a slower camera speed (2km/h) would be required for the camera to be able to capture the thermal contrast at the simulated leak location that yield an accuracy greater than 89%, however at speed of 5km/h the leak was detected within an error more than 33%.

The results obtained in this study have also shown that under high ambient temperatures (42^{o}C) and high relative humidity (75%) conditions, a higher speed of the IR camera (5km/h) would reduce the impact of noise on the collected thermal contrast and therefore, would give better leak location prediction results with 90% accuracy. The accuracy of leak location prediction dropped to 66% when the camera was operated at a speed of 2km/h. The field of view (FOV) is affected by the camera's height from the surface. At lower

heights, less area will be covered per frame; therefore, a more homogenous temperature distribution per frame will be obtained. Consequently, the contrast between the different frames will be higher and better leak predictions would be expected.

It was found that the best operating conditions of the IR camera would be at low ambient air temperature (24 ^{o}C - 29 ^{o}C), low humidity (<50%), and high emissive surface (asphalt pavement ε=0.93).

The tested methodology proved the flexibility of the approach and the ability of accurately predicting the leak locations under different conditions. However, the main limitation of using IR thermography for leak prediction in water networks is that the leak should reach the upper surface close to the ground surface for the camera to be able to capture the thermal contrast. Otherwise, no thermal contrast will be captured. In cases of deeper pipes, IR thermography may not be the best choice for potential leak inspection. Therefore, GPR had been implemented in this study for leak detection in addition to pipe location determination. GPR leak detection was based on subsoil features extraction. A refinement process for the collected diagram has been carried out based on the fk-migration function in Reflex2DQuick software. After the refinement process, it was noticed that the radargram included observed anomalies that could conclude that the subsurface conditions had been changed which could be attributed to a leak event. The GPR method requires further investigations to proof the applicability of the method under different condition.

References

[1] World Economic Forum, 2014. Global Risks 2014, ninth edition World Economic Forum, Geneva. Available online at: http://www3.weforum.org/docs/WEF_ GlobalRisks_Report_2014.pdf. [Accessed January 2015].

[2] World Economic Forum, 2015. Global Risks 2015, 10th edition World Economic Forum, Geneva. Available online at: http://www3.weforum.org/docs/WEF_Global_Risks_2015_Report15.pdf [Accessed April 2015]

[3] Wu, P., Tan, M. (2012, . Challenges for sustainable urbanization: a case study of water shortage and water environment changes in Shandong, China. Paper presented at the 18th Biennial Conference of International Society for Ecological Modeling (China)(pp. 919-927). Procedia Environmental Sciences.

[4] EU, 2007. Addressing the Challenge of Water Scarcity and Droughts in the European Union, Communication from the Commission to the European Parliament and the Council, Eur. Comm., DG Environ., Brussels, 2007.

[5] Vardon, M., Lenzen, M., Peevor, S., Creaser, M., 2007. Water accounting in Australia. Ecol. Econ. 61, 650–659.

[6] Tsakiris, G., Vangelis, H., 2005. Establishing a drought index incorporating evapotranspiration. Eur. Water 9 (10), 3–11.

[7] Kim, S. L., Paul Chen, J. & Ting, Y. P. 2002. Study on feed pretreatment membrane filtration of secondary effluemt. Spearation and Purification Technology, 29, 171-179.

[8] Qatar Environment and Energy Institute, 2013. Available online at: http://www.qf.org.qa/content/the-foundation/issue-58/qeeri-takes-an-integrated-approach-to-securing-water-supply. [Accessed January 2015].

[9] Qatar General Secretariat for Development Planning (GSDP), 2011. Qatar National Development Strategy 2011~2016: Towards Qatar National Vision 2030. [pdf] Doha: Gulf Publishing and Printing Company. Available at: http://www.gsdp.gov.qa/portal/page/portal/gsdp_en/knowledge_center/Tab/Qatar_NDS_reprint_complete_lowres_16May.pdf [Accessed December 2014].

[10] Cataldo A, Persico R, Leucci G, De Benedetto E, Cannazza G., 2014. Time Domain Reflectometry, Ground Penetrating Radar and Electrical Resistivity Tomography: A Comparative Analysis of Alternative Approaches for Leak Detection in Underground Pipes. NDT&E International , 62: 14-28.

[11] Kingdom B, Liemberger R, Marin P., 2006. The Challenge of Reducing Non-Revenue Water (NRW) in Developing Countries. The International Bank for Reconstruction and Development, Paper Series 8, 1-52.

[12] Xu Q, Liu R, Chen Q, Li R., 2014. Review on water leakage control in distribution networks and the associated environmental benefits. Journal of Environmental Sciences, 26: 955-961.

[13] Ishido, Y, Takahashi S., 2014. A New Indicator for Real-time Leak Detection in Water Distribution Networks: Design and Simulation Validation. Procedia Engineering, 89: 411-417.

[14] Kuiper N, Rowell C, Shomar B., 2015. High levels of molybdenum in Qatar's groundwater and potential impacts. Journal of Geochemical Exploration , 150: 16-24.

[15] Qatar General Electricity and Water Corporation. Available at: http://www.siww.com.sg/pdf/Biz_Opps_in_Water_Industry_in_Qatar.pdf [Accessed May 2014].

[16] Statistics Authority in Qatar (SAQ) (2010). "The Millennium Development Goals for the State of Qatar 2010,"http://www.qsa.gov.qa/eng/pdf/Millinum_development_goals/MDGEng2010.pdf

[17] Duffy, M., 2015. Innovative solutions in the water industry: Leak detection.

[18] Sousa, J., Ribeiro, L., Muranho, J., Sa Marques, A., 2015. Locating leaks in water distribution networks with simulated annealing and graph theory. Procedia Engineering, 119: 63-71.

[19] Zangenehmadar, Z., Moselhi, O., 2014. Study of leak detection technologies in water distribution networks. Paper presented at Congres general 2014 de la SCGC.(Canada).

[20] Liu, Z., Kleiner, Y., Rajani, B., Wang, L., & Condit, W. 2012. Condition Assessment Technologies for Water Transmission and Distribution Systems. United States Environmental Protection Agency (USEPA), Washington DC.

[21] Hao T, Rogers CDF, Metje N, et al. 2012. Condition assessment of the buried utility service infrastructure. Tunnel Underground Space Technol. 28: 331-344.

[22] Yang, Mu, Jill L. Silverman, and Jacqueline N. Crawley. 2011. "Automated Three-Chambered Social Approach Task for Mice." Current protocols in neuroscience: 8-26.

[23] Vickridge, I. G., and D. Leontidis. 1997. "Sewer surveys." Sewers ,Rehabilitation and Construction 1: 84-102.

[24] Liu Z, Kleiner Y. 2013. State of the art review of inspection technologies for condition assessment of water pipes. Measurement. 46(1):1-15.

[25] Costello SB, Chapman DN, Rogers CDF, Metje N. 2007. Underground asset location and condition assessment technologies. Tunnel Underground Space Technol. 22(5–6): 524-542.

[26] Wilson, J.W., Kaba, M., and Tian, G.Y. (2008). "New Techniques for the Quantification of Defects Through Pulsed Magnetic Flux Leakage." 17th World Conference on Nondestructive Testing, Shanghai, China.

[27] Makar, J.M., and Chagnon, N. (1999). "Inspecting Systems for Leaks, Pits, and Corrosion." Journal of AWWA, 91(7), 36-46.

[28] Sachs, J., Badstubner, A., Bonitz, F. (2008). High resolution non-destructive testing in civil engineering by ultra-wideband pseudo-noise approaches. International Conference on Ultra-Wideband, Hannover, Germany.

[29] Mergelas, B., and Henrich, G. (2005). "Leak Locating Method for Pre-Commissioned Transmission Pipelines: North American Case Studies." Leakage 2005, Halifax, Canada, 1-7.

[30] Pressure Pipe Inspection Company ,PPIC. (2006). "Transmission Main Leak Location (Sahara)."

[31] Fletcher, R. (2008). "SmartBall - A New Approach in Pipeline Leak Detection." International Pipeline Conference, Calgary, Alberta, Canada, 1-17.

[32] Sack, D.A., and Olson, L.D. (1998). "Impact Echo Testing of In-Situ Precast Concrete Cylinder Pipe." Pipelines in the Constructed Environment, J.P. Castronovo and J.A. Clark, eds., American Society of Civil Engineers, San Diego, CA, USA, 250-259.

[33] Butler, D. (2009). "Leak Detection and Management: A Comprehensive Guide to Technology and Practice in the WaterSupply Industry." Palmer Environmental, Cwmbran, UK.

[34] Rose, J.L., Mu, J., and Cho, Y. (2008). "Recent Advances on Guided Waves in Pipe Inspection." 17th World Conference on Nondestructive Testing, Shanghai, China.

[35] Bosch, J., Hugger, A., Franz, J., Falter, S., and Oberdorfer, Y. (2004). "Phase Array Technology for Automated Pipeline Inspection." Business Briefing: Exploration & Production: The Oil & Gas Review, 1-4.

[36] Beller, M., and Barbian, A. (2006). "Combined In-Line Inspection of Pipelines for Metal Loss and Cracks." European Conference on Nondestructive Testing, Berlin, Germany, 1-13.

[37] Munser, R., Robner, M., Hartrumpf, M., and Kuntze, H.B. (1999). "Microwave Back-Scattering Sensor for the Detection of Hidden Material Inhomogeneities e.g. Pipe Leakages." 9th International Trade Fair and Conference for Sensors, Transducers and Systems, Nuremberg, Germany, 1-7.

[38] Bimpas, M., Amditis, A., Uzunoglu, N. 2010. Detection of water leaks in supply pipes using continuous wave sensor operating at 2.45 GHz. Journal of Applied Geophysics : 70, 226-236.

[39] Higgins, M.S., and Paulson, P. (2006). "Fiber Optic Sensor for Acoustic Monitoring of PCCP." Pipelines 2006 - Service to the Owner, A. Atalah and A. Tremblay, eds., Chicago, Illinois, USA.

[40] FLIR Systems AB. 2004. ThermaCAM S60 operator's manual, Danderyd,Sweden, 2–40.

[41] Rao, DSP.2008. Infrared thermography and its applications in civil engineering.Indian Concr J: 41–50.

[42] Rogalski, A. 2012. History of infrared detectors. Optoelectron Rev. ;20:279–308.

[43] FLIR Systems 2005. ThermaCAM B2:Operator's Manual. Sweden.

[44] Barreira E, de Freitas VP, Delgado JMPQ, Ramos NMM. 2012. Thermography applications in the study of buildings hygrothermal behaviour. In: Prakash RV, editor. Infrared thermography. Croatia, China: InTech; p. 171–92.

[45] Mahmoud M. Engineering thermofluids. Heidelberg, New York, Dordrecht,London: Springer; 2005.

[46] Cengel YA. Introduction to thermodynamics and heat transfer. McGraw Hill series in mechanical engineering/international edition. McGraw Hill; 1997.ISBN: 0-07-011498-6.

[47] American Society of Heating, Refrigerating and Air-Conditioning Engineers _ASHRAE_ 1981; Hutcheon and Handegord 1983; Bentz 2000.

[48] Schlangen, E. _2000_. Heat of *FEMMASSE* manual, INTRON BV, The Netherlands.

[49] Mcullough, B., and Rasmussen, R. 1999. Fast track paving: Concrete temperature control and traffic opening criteria for bonded concrete overlays, Federal Highway Administration, Mclean, Va.

[50] Bentz, D. 2000. A computer model to predict the surface temperature and time-of-wetness of concrete pavements and bridge decks, Vol. 6551, National Institute of Standards and Technology NISTIR, U.S. Department of Commerce, 1–29.

[51] Walton, G. 1985. "Thermal analysis research program—Reference manual." NBSIR 83-655, Department of Commerce.

[52] B. conyers, L. 1997. Ground Penetrating Radar for Archeology.Rowman & Littlefield Publishers, Inc. ISBN:9780759123489.

[53] Gehrig, M., Morris, D., Bryant, J. 2004. Ground penetrating radar for concrete evaluation studies. Available at : http://citeseerx.ist.psu.edu/viewdoc/download?doi=10.1.1.522.4134&rep=rep1&type=pdf [Accessed June 2015].

[54] Fahmy, M., Moselhi, O. 2010. Automated Detection and Location of Leaks in Water Mains Using Infrared Photography. Journal of Performance of Constructed Facilities. Vol24:242-248

[55] Al-Barqawi, H., Zayed, T. 2006. Assessment model of Water Main Conditions. Pipelines.

[56] Reflex2DQuick manual. Available at http://www.sandmeier-geo.de/Download/reflex2dquick.pdf [accessed July 2015].

[57] Marinetti S, Cesaratto PG. Emissivity Estimation for Accurate Quantitative Thermography. NDT&E International 2012; 51: 127-134.

[58] Beier K, Gemperlein H. Simulation of infrared detection range at fog conditions for Enhanced Vision Systems in civil aviation. Aerospace Science and Technology 2004; 8: 63–71